

DISS. ETH NO. 29126

# **Mass measurements of optically trapped aerosol particles**

A thesis submitted to attain the degree of  
DOCTOR OF SCIENCES  
(Dr. sc. ETH Zurich)

presented by  
OLIVER RAFAEL REICH

MSc ETH Zurich  
born on 21.05.1992

accepted on the recommendation of  
Prof. Dr. Ruth Signorell, examiner  
Prof. Dr. Lukas Novotny, co-examiner

2023



# Contents

<b>1</b>	<b>Introduction</b>	<b>1</b>
<b>2</b>	<b>Theory of light-particle interaction</b>	<b>6</b>
2.1	Single particle elastic light scattering . . . . .	7
2.2	Mie scattering . . . . .	11
2.3	Optical force on a trapped particle . . . . .	14
2.4	Holography . . . . .	17
2.5	Raman scattering . . . . .	20
<b>3</b>	<b>Experimental methods</b>	<b>23</b>
3.1	Optical trapping . . . . .	23
3.2	Trapping cells . . . . .	24
3.3	Particle generation . . . . .	28
3.4	Particle characterization methods . . . . .	29
3.4.1	Two-dimensional angular optical scattering spectrum . . . . .	29
3.4.2	Broad-band light scattering . . . . .	29
3.4.3	Raman scattering . . . . .	32

3.4.4	Holography . . . . .	34
<b>4</b>	<b>Single particle mass measurement</b>	<b>37</b>
4.1	Optical trap for mass measurement . . . . .	38
4.2	Harmonic oscillator model . . . . .	40
4.3	Damping model corrections . . . . .	43
4.4	Experimental setup for mass measurement . . . . .	47
4.5	Example data set . . . . .	49
<b>5</b>	<b>Weighing picogram aerosol droplets with an optical balance</b>	<b>54</b>
5.1	Introduction . . . . .	56
5.2	Results . . . . .	57
5.2.1	Principle of mass measurement . . . . .	57
5.2.2	Harmonicity of the droplet oscillation . . . . .	59
5.2.3	Mass measurement and related quantities . . . . .	61
5.3	Discussion . . . . .	62
5.3.1	Range and accuracy of mass measurements . . . . .	62
5.3.2	Applications . . . . .	65
5.4	Methods . . . . .	66
5.4.1	Droplet generation and relative humidity control . . . . .	66
5.4.2	Droplet dynamics . . . . .	67
5.4.3	Phase measurement and systematic error . . . . .	67
5.4.4	Random error . . . . .	68



5.4.5	Broad-band light scattering (BLS) . . . . .	68
5.4.6	Mass growth factor $m^*$ . . . . .	70
5.5	Acknowledgements . . . . .	70
5.6	Author contributions . . . . .	70
5.7	Competing interests . . . . .	71
5.8	Supplementary information . . . . .	72
5.8.1	BLS spectra . . . . .	72
5.8.2	Droplet dynamics at Mie resonances . . . . .	72
5.8.3	Influence of the light focus on the phase measurement . . . . .	74
5.8.4	Size growth factor . . . . .	75
<b>6</b>	<b>Hygroscopic growth of single atmospheric sea salt aerosol particles from mass measurement in an optical trap</b>	<b>77</b>
6.1	Introduction . . . . .	79
6.2	Methods . . . . .	80
6.2.1	Optical trapping . . . . .	80
6.2.2	Size measurement . . . . .	81
6.2.3	Harmonic oscillator model for determination of particle mass . . . . .	82
6.2.4	Mass measurement . . . . .	85
6.2.5	Raman measurement and determination of particle dry mass . . . . .	87
6.3	Results and discussion . . . . .	89
6.3.1	Hygroscopicity of NaCl droplets . . . . .	89

6.3.2	Hygroscopicity of mixed salt droplets . . . . .	91
6.3.3	Importance of the definition of the salt dry mass for hygroscopic mass growth factors . . . . .	94
6.3.4	Significance of these hygroscopicity measurements of sea salt droplets . . . . .	95
6.4	Evolution of Raman spectra and phase transition preceding efflorescence . . . . .	96
6.5	Conclusions . . . . .	98
6.6	Acknowledgements . . . . .	100
6.7	Data availability . . . . .	100
<b>7</b>	<b>Optical trapping and mass measurement in water</b>	<b>101</b>
7.1	Introduction . . . . .	101
7.2	Methods . . . . .	102
7.3	Results and discussion . . . . .	105
7.4	Conclusions . . . . .	111
<b>8</b>	<b>Photo-induced shrinking of aqueous glycine aerosol droplets</b>	<b>113</b>
8.1	Introduction . . . . .	115
8.2	Methods . . . . .	116
8.3	Results and discussion . . . . .	118
8.4	Conclusions . . . . .	128
8.5	Acknowledgements . . . . .	129
<b>9</b>	<b>Conclusion</b>	<b>130</b>

<b>10 Appendix</b>	<b>134</b>
10.1 Optical force calculation using far field expressions . . . . .	134
10.2 Holography reconstruction . . . . .	138

## Abstract

Aerosol particles are ubiquitous in Earth's atmosphere and consist of a wide variety of species with different compositions, lifetimes and sizes. This heterogeneous ensemble of particles influences many atmospheric processes through complex interactions between individual aerosol particles, between particles and the surrounding gas phase, as well as through scattering and absorption of incident sunlight. The understanding of these processes requires accurate data on the properties of the particles that are involved. Laboratory studies of aerosol particles focus on the measurement of their properties under well controlled environmental conditions. Optical trapping is used to isolate and confine individual aerosol particles, enabling retrieval of single particle data. This information, which is not readily obtained from investigations of particle ensembles, can provide detailed insight into the underlying interaction mechanisms of the complex processes that occur in the atmosphere.

This work presents a number of measurement techniques for the characterization of single optically trapped aerosol particles. As a main result, a new method to measure the mass of single aerosol particles using optical trapping is introduced. This method is in particular applicable to liquid droplets, an important subclass of aerosol particles, for which mass measurement using optical trapping is challenging, and thus has not been demonstrated before. The accuracy and precision of our optical mass measurement method is characterized for aerosol droplets with sizes of a few micrometers down to the submicron size range. We use the new method to measure the hygroscopic mass growth factor of single sea salt droplets, which belongs to the most abundant species of aerosol particles in the atmosphere. Conflicting values for the hygroscopicity of sea salt have been published in the literature, limiting the accuracy of climate models that rely on these values as input parameters. With the new data, we are able to critically review previous values and propose a way to reconcile the apparent discrepancies in the literature. These results are expected to improve future model predictions. Performance of the optical mass measurement method is further tested for particle trapping in the liquid phase. This application holds potential for studying single cells *in vivo*. Single micrometer sized glass spheres were trapped in water in order to characterize the accuracy of the mass measurement. The current

limitations of the measurement setup are identified and discussed with regard to the accuracies required for applications in the aqueous phase.

Finally, a previously unknown photolysis reaction of glycine dissolved in aqueous droplets is demonstrated. The reaction was observed as photoinduced shrinking of an aqueous glycine droplet when a laser with wavelength 532 nm was used for trapping. The reaction is characterized with regard to shrinking rate and temporal evolution of the molecular composition of the droplet during the shrinking. A possible reaction mechanism is discussed, which indicates hitherto unknown photochemical pathways for atmospheric aerosol particles.

## Zusammenfassung

Aerosolteilchen sind in unserer Atmosphäre allgegenwärtig. Es existiert eine breite Palette von Teilchenarten, welche unterschiedliche Zusammensetzung, Lebensdauer und Grösse haben. Zusammen bilden sie ein heterogenes Gemisch, das durch komplexe Wechselwirkungen zwischen den einzelnen Teilchen oder zwischen Teilchen und der umgebenden Gasphase, sowie durch Absorption und Streuung des Sonnenlichts viele atmosphärische Prozesse beeinflusst. Um solche Prozesse zu verstehen, müssen zuverlässige Daten über die Eigenschaften der beteiligten Teilchen gesammelt werden. In Laborstudien werden die Eigenschaften von Aerosolteilchen unter kontrollierten Umgebungsbedingungen gemessen. Optische Fallen werden benutzt, um individuelle Aerosolteilchen zu isolieren und festzuhalten, damit man Daten von Einzelteilchen erheben kann. Diese Daten aus Untersuchungen an Teilchensembles zu erhalten, ist dagegen nicht praktikabel. Die Informationen, welche man über die einzelnen Aerosolteilchen gewinnt, helfen dabei, detaillierte Einsichten in die komplexen Prozesse, welche in unserer Atmosphäre stattfinden, zu erhalten, sowie die zugrundeliegenden Mechanismen besser zu verstehen.

Die Arbeit, die hier präsentiert wird, stellt eine Reihe von Messtechniken vor, welche für die Charakterisierung von einzelnen optisch gefangenen Aerosolteilchen nützlich sind. Eines der wesentlichen Resultate ist die Entwicklung einer Methode, mit der die Masse von einzelnen Aerosolteilchen in einer optischen Falle gemessen werden kann. Diese Methode kann insbesondere auch für Tröpfchen verwendet werden, für die die Bestimmung der Masse mittels optischer Fallen mit wesentlichen experimentellen Schwierigkeiten verbunden und deshalb bisher nicht gelungen ist. Es wird gezeigt, wie genau und präzise die Methode für Tröpfchen unterschiedlicher Grössen ist, welche von mehreren Mikrometern bis hin zu Submikrometer grossen Tröpfchen reichen. Mit dieser Methode bestimmen wir den hygrokopischen Massenwachstumsfaktor einzelner Meersalztröpfchen, welche zu den häufigsten Aerosolarten in der Atmosphäre gehören. Es existieren heutzutage widersprüchliche Angaben zur Hygrokopizität von Meersalz. Dadurch wird die Genauigkeit von Klimamodellen beeinträchtigt, die auf diesen Daten aufbauen. Unsere Messungen erlauben es uns, die bisherigen Angaben kritisch zu prüfen. Wir schlagen eine Lösung vor, wie die scheinbaren Widersprüche in der

Literatur behoben werden können. Diese Resultate sollten uns in Zukunft bessere Modellvorhersagen erlauben. Desweiteren wird die Anwendbarkeit der neuen Methode für Massenmessungen von optisch gefangenen Teilchen in flüssiger Phase getestet. Diese Anwendung wäre insbesondere für In-vivo-Untersuchungen von einzelnen Zellen interessant. Die Genauigkeit der Massenmessung für optisch gefangene Teilchen in Wasser wurde anhand von Mikrometergrossen Glaskügelchen getestet. Daraus lassen sich die Grenzen des aktuellen Messaufbaus für die Massenmessung ableiten, welche wir im Bezug auf die benötigte Genauigkeit für Massenmessungen in Wasser diskutieren.

Zum Schluss wird gezeigt, wie in einem wässrigen Tröpfchen gelöstes Glycin entgegen bisheriger Erwartungen photolysiert wird. Die Reaktion wird als Schrumpfen von wässrigen Glycintröpfchen beobachtet, wenn diese Tröpfchen in einer optischen Falle mit Licht der Wellenlänge 532 nm gefangen werden. Wir charakterisieren diese Reaktion mit Bezug auf die Schrumpfrate und die zeitliche Entwicklung der Molekülzusammensetzung des Tröpfchens während des Schrumpfens. Ein möglicher Reaktionsmechanismus wird diskutiert. Dieser suggeriert einen bisher unbekanntem photochemischen Reaktionspfad für atmosphärische Aerosolteilchen.

# 1 Introduction

Aerosols are dispersions of solid or liquid particles in a gas. Various fields of science are concerned with the study of aerosol particles, their properties, chemistry, industrial and health applications. In this work, aerosol particles are primarily discussed with regard to their role in Earth's atmosphere<sup>1,2</sup>. Atmospheric aerosol particles affect Earth's climate through direct interaction with the sunlight and indirectly due to their ability to facilitate cloud formation. They have been identified as one of the significant driving forces of current climate change. While generally smaller in magnitude, the effect of aerosol particles is thought to counteract the effect of greenhouse gases in the atmosphere<sup>3</sup>. However, current estimates of the aerosol driven climate change suffer from large uncertainties. The estimates of the aerosol contribution constitute the largest source of uncertainty in current prediction of Earth's radiative forcing<sup>1,3</sup>. These uncertainties in aerosol driven climate change predictions fuel ongoing research of atmospheric aerosol particles. Accurate data about the physical and chemical properties of the aerosol species present in the atmosphere is needed to better understand the processes affecting them. A large subclass of atmospheric species are liquid aerosol particles, or droplets. The work in this thesis focuses on the accurate characterization of single atmospherically relevant aerosol droplets under well defined laboratory conditions using optical trapping. A main result is the development of a method to measure the mass of single optically trapped aerosol droplets.

Optical trapping is a method to isolate and confine single particles in space by applying optical forces using laser light. Invented in 1970 by Arthur Ashkin<sup>4</sup>, optical trapping has since developed into a versatile tool that has facilitated a great number of studies in a diverse field of science. Key features of this technique are the precise control and characterization of single particles in situ in liquid, gaseous and vacuum environments. This data can provide detailed information of processes that occur inside, or in interaction with, individual particles. In contrast, this data cannot be obtained from measurements of



particle ensembles, which yields only average particle properties. In addition, optical trapping is a contact free alternative to conventional methods where particles are deposited on a substrate, which may perturb the natural state of the particle.

Though not exclusive to these areas of science, optical trapping has been frequently employed in the fields of biology, atmospheric and fundamental research. In the field of biology and biological applications, optical trapping is typically used to investigate single particles, such as biomolecules, cells and viruses, in an aqueous environment. Optical trapping has been successfully applied to observe cell division and manipulate organelles<sup>5</sup>, to deform of single cells and DNA molecules and to measure their viscoelastic properties<sup>6-8</sup>. Optical traps have also been employed to characterize the interactions of certain motorproteins with microtubules and actin filaments<sup>9-13</sup>, non-invasive measurement of the molecular composition of cells and cell parts<sup>14,15</sup>, as well as many other examples<sup>16,17</sup>. In the field of fundamental research, optical trapping is typically used to trap well calibrated particles to use them as probes in low pressure environments. Such applications of optical trapping have been demonstrated to be useful for the detection of small forces<sup>18-21</sup>. The reported sensitivities ( $\sim 10^{-21}$  N) are similar to the ones of solid-state sensors, however the latter require cryogenic cooling to achieve this performance, unlike optically trapped probe particles<sup>19</sup>. Furthermore, optically trapped probe particles allow for ultrasensitive ( $\sim 10^{-27}$  N m) detection of torques<sup>20-23</sup>. In atmospheric sciences, studies of aerosol particles include the measurement of the viscosity of organic aerosol droplets<sup>24,25</sup>, size dependent photoabsorption<sup>26,27</sup>, determination of diffusion and uptake coefficients<sup>28-30</sup> and kinetics of phase transitions<sup>31</sup>.

Optical trapping of atmospherically relevant aerosol particles is typically performed in a gaseous environment. In contrast to the examples in aqueous or low pressure environments, atmospheric particles often contain volatile components that exist only in a thermodynamic equilibrium with the surrounding gas phase. This includes hygroscopic particles, which in humid environments pick up water from their surrounding to form droplets, such as sea spray, one of the most abundant aerosol species in the atmosphere<sup>1</sup>. As a consequence, optical trapping of atmospherically relevant aerosol particles, in particular droplets, has to be performed at ambient conditions for best comparison to their natural counterparts. Many techniques have been established for the thorough characterization of optically trapped aerosol droplets, with the goal to obtain accurate data of single particles under well defined conditions. Here we restrict ourselves to highlight those relevant for the work

in this thesis. These include the measurement of radius and wavelength dependent refractive index of droplets<sup>32</sup>, their morphology<sup>33</sup> and the tracing of their molecular composition over time<sup>34,35</sup>.

Mass is a fundamental property of any object. With regard to atmospheric aerosol droplets, there are many processes that affect their mass, such as chemical reactions, as well as evaporation and condensation of water. Despite the potential to characterize a variety of processes affecting droplets as well as other atmospheric particles, their mass has rarely been measured in previous studies using optical trapping. Techniques of single particle mass measurements using optical trapping in the gas phase and other environments are relatively new, and most have emerged in the last decade only<sup>36-41</sup>. It is not surprising in this context that the potential and the range of possible applications of these optical mass measurements have not been widely explored yet. Previous examples focus around the applications in low pressure environments for ultrasensitive force and torque sensing. Accurate mass measurements are used to better characterize the solid probe particles in order to achieve better performance of the sensors<sup>36</sup>. As such, mass measurements for these applications are designed for solid particles in low pressure environments. At ambient conditions, studies involving mass measurement of optically trapped aerosol particles are very limited<sup>40,41</sup>. Previous studies focus on photophoretic trapping, which is based on the heating of the trapped particle by absorption of the incoming laser light<sup>42</sup>. Reported accuracies are approximately 10–15 % for particle sizes of a few<sup>41</sup> to a few tens<sup>40</sup> of micrometers. These photophoretic mass measurements are applicable only to particles which absorb light at the wavelength of the trapping beams and are resistant to heating to at least several tens of degrees above room temperature<sup>40,41</sup>.

Previous optical mass measurement methods are only applicable to non-volatile, solid particles. In low pressure environments, the high vapor pressure of volatile particles, such as droplets, is not in equilibrium with their environment, hence the particles evaporate. Similarly, volatile particles in photophoretic traps would rapidly evaporate due to the heating by the incident laser light. Even for semi-volatile species, laser induced heating would at least disturb the equilibrium between particle and surrounding at ambient conditions. This would make interpretation of measured thermodynamic quantities for atmospherically relevant particles, in particular droplets, very challenging. State-of-the-art methods to measure the mass of single levitated aerosol droplets, though also applicable to other particles in gas or vacuum, typically use an electrodynamic balance (EDB)<sup>43-45</sup> for trapping. EDBs

are frequently used for laboratory studies of atmospherically relevant aerosol species, though they require charging of the droplets and typically only allow access to particles with sizes larger than approximately  $5\ \mu\text{m}$ . However, atmospheric aerosol sizes follow a multimodal distribution<sup>46</sup>. The typical size range of EDB covers the coarse particle mode, but does not allow access to the submicron size range, where the majority of atmospheric aerosol particles reside.

Motivated by the limitations of existing mass measurement methods with regard to atmospheric aerosol species, a new method to measure the mass of single aerosol particles using optical trapping is demonstrated in this thesis. In Chapter 4 the principle of the new method is presented and the feasibility of the concept is demonstrated. Its performance is evaluated in Chapter 5 and it is compared to other methods using optical trapping and EDBs for mass measurement. A key feature of the new method is its applicability to volatile and semi-volatile particles, in particular droplets, which is achieved by designing the method to work for particles with negligible absorption at the wavelength of the trapping beams (in order to not perturb equilibrium) and for ambient conditions. It is later shown in Chapter 6 that the method provides reliable mass data even for the submicrometer size range, which is of particular importance for atmospheric particles. The applicability of this method to submicron particles is another important strength of the new approach.

Mass is a fundamental property of aerosol particles, hence the new method is anticipated to be interesting for application in a variety of future studies. To explore the range of possible applications, an example is demonstrated in Chapter 6. As shown in previous studies using an EDB<sup>45</sup>, mass measurements can be employed to determine the hygroscopic mass growth factor of single aerosol particles. Hygroscopic particles in the atmosphere pick up water from humid environments to form droplets. Sea spray is one of the most abundant species of atmospheric aerosols. The size distribution of these highly hygroscopic species, and therefore their interaction with the sunlight, depends critically on the relative humidity of their environment<sup>47,48</sup>. The hygroscopicity is a key parameter to predict the magnitude of the interaction of a given atmospheric aerosol species with the sunlight. Sea salt is the inorganic part and a major component of sea spray. Conflicting values for the hygroscopicity of sea salt have been reported, which limits the accuracy of model predictions that are based on this data<sup>49</sup>. Facilitated by the new optical mass measurement method, we obtain new values for the hygroscopic mass growth of single sea salt droplets in Chapter 6, and critically review literature

values. We also obtained, for the first time, values for single submicrometer sized droplets. As a second example, application of our mass measurement method to particles trapped in liquids was investigated (Chapter 7). This avenue holds potential for the investigation of single cells and other biological particles *in vivo*. We obtain preliminary data for microspheres submerged in water and discuss the current limitations with regard to the accuracy of the method. In Chapter 8 we extend our investigations to aerosol droplets containing organic components. Aqueous glycine droplets were studied as an example of atmospherically relevant organic droplets. They can also be considered as a proxy for other, more complex amino acids. We found a previously unexpected photolysis reaction of glycine in the aqueous droplets when a trapping laser in the visible range (532 nm) was used. The reaction was observed as continuous shrinking of the micrometer sized droplets over the course of a few hours to several days. A possible mechanism for this photolysis reaction is discussed in preparation of future studies involving mass measurements of glycine droplets.

## 2 Theory of light-particle interaction

Many of the relevant aspects of the light-particle interaction in this thesis are captured by classical electrodynamics. Therefore, a brief recapitulation is presented here, with a focus on light scattering by single particles. For the phenomena discussed here, it is sufficient to consider stationary electric and magnetic fields,  $\mathbf{E}^{(t)}(t) = \text{Re}(\mathbf{E} e^{-i\omega t})$ ,  $\mathbf{B}^{(t)}(t) = \text{Re}(\mathbf{B} e^{-i\omega t})$ , respectively, where  $\mathbf{E}^{(t)}$  and  $\mathbf{B}^{(t)}$  are the electric and magnetic field,  $\mathbf{E}$  and  $\mathbf{B}$  their respective spatial part and  $\omega$  the frequency of the field oscillation. Furthermore, free charges and currents are absent or irrelevant for the experiments in question. In this case, it follows from Maxwell's equations that  $\mathbf{E}$  and  $\mathbf{B}$  fulfill the equations ( $\mathbf{F} = \mathbf{E}, \mathbf{B}$ )

$$\Delta \mathbf{F} = -(|\mathbf{k}| \cdot n)^2 \mathbf{F} \quad (2.1)$$

$$\nabla \cdot \mathbf{F} = 0 \quad (2.2)$$

where  $\mathbf{k}$  is the corresponding wavevector in vacuum, with  $k = |\mathbf{k}| = \frac{\omega}{c}$ , where  $c$  is the speed of light in vacuum, and  $n$  is the refractive index of the medium. Here it is implicitly assumed that the medium is optically linear and isotropic, and that only elastic scattering occurs, such that  $n$  describes all aspects of the optical response of the medium. For the experiments in this thesis, the assumptions of optical linearity and isotropy are valid to very good approximation. An important exception to the last assumption is inelastic Raman scattering, which is discussed later in Section 2.5.

Eq.(2.1) represents the wave equation, while Eq.(2.2) specifies that the waves be solenoid. The scattering phenomenon emerges as a consequence of non-continuous changes of  $n$  at interfaces, such as the surface of a particle. Using Eq.(2.1), Eq.(2.2) and suitable boundary conditions, the solutions for  $\mathbf{E}$  and  $\mathbf{B}$  can be found independently of each other. Furthermore, if a solution for either  $\mathbf{E}$  or  $\mathbf{B}$  has been found, one may find the respective other field using

the Maxwell's equations

$$\begin{aligned} ikc \cdot \mathbf{B} &= \nabla \times \mathbf{E} \\ -i\frac{k}{c}n^2 \cdot \mathbf{E} &= \nabla \times \mathbf{B} \end{aligned} \quad (2.3)$$

With this, we focus on  $\mathbf{E}$  in the following to describe light scattering by single particles.

## 2.1 Single particle elastic light scattering

The theory presented here is taken in essence from a standard textbook<sup>50</sup> and a tutorial article<sup>51</sup>. The following system serves as a starting point for our discussion: A homogeneous particle with refractive index  $n_i$  is illuminated by a plane electromagnetic wave propagating through a medium with refractive index  $n_0 \neq n_i$ . Fig.(2.1) shows a schematic of light scattering by a single particle. The electric field inside the particle is denoted  $\mathbf{E}_i$  and the field outside the particle is the sum of incident and scattered waves,  $\mathbf{E}_0 + \mathbf{E}_s$ . All fields ( $\mathbf{E}_i$ ,  $\mathbf{E}_0$  and  $\mathbf{E}_s$ ) must fulfill Eq.(2.1) and Eq.(2.2). To solve for the individual electric fields, we would like to find a basis of general solutions to Eq.(2.1) and Eq.(2.2). To this end, consider a scalar function  $\psi \neq 0$  with

$$\Delta\psi = -(kn)^2\psi \quad (2.4)$$

where  $n = n_0$  outside and  $n = n_i$  inside the particle. The following fields then automatically fulfill Eq.(2.1):

$$\begin{aligned} \mathbf{L} &= \nabla\psi \\ \mathbf{M} &= \nabla \times (\mathbf{r}\psi) \\ \mathbf{N} &= \frac{1}{kn} \nabla \times \mathbf{M} \end{aligned} \quad (2.5)$$

$\mathbf{L}$ ,  $\mathbf{M}$  and  $\mathbf{N}$  are the vector harmonics for which a few important relations

hold:

$$\begin{aligned}
 \nabla \cdot \mathbf{L} &= -(kn)^2 \psi \neq 0 \\
 \nabla \times \mathbf{L} &= 0 \\
 \nabla \cdot \mathbf{M} &= 0 \\
 \nabla \cdot \mathbf{N} &= 0 \\
 \nabla \times \mathbf{N} &= kn \mathbf{M}
 \end{aligned} \tag{2.6}$$

It follows thus that  $\mathbf{M}$  and  $\mathbf{N}$  fulfill Eq.(2.2) as well. A complete set of solutions for Eq.(2.4) is given in spherical coordinates by

$$\begin{aligned}
 \psi_{lme}(r, \theta, \varphi) &= z_l(knr) \cdot P_l^m(\cos(\theta)) \cdot \cos(m\varphi) \\
 \psi_{lmo}(r, \theta, \varphi) &= z_l(knr) \cdot P_l^m(\cos(\theta)) \cdot \sin(m\varphi)
 \end{aligned} \tag{2.7}$$

where  $z_l$  with  $l = 0, 1, 2, \dots$  are the Bessel functions of the first or second kind,  $z_l = j_l, y_l$ , respectively, or superpositions thereof, and  $P_l^m$  with  $l = 0, 1, 2, \dots$ ,  $m \leq 0, 1, \dots, l$  are the associated Legendre polynomials. The indices  $e$  and  $o$  indicate even and odd parity, respectively, with regard to the transformation  $m \rightarrow -m$ .

Using this set of  $\psi$ , we find with Eq.(2.5):

$$\begin{aligned}
 \mathbf{M}_{lme} &= -z_l \cdot \frac{m}{\sin(\theta)} P_l^m \cdot \sin(m\varphi) \hat{\boldsymbol{\theta}} - z_l \cdot \frac{\partial P_l^m}{\partial \theta} \cdot \cos(m\varphi) \hat{\boldsymbol{\varphi}} \\
 \mathbf{M}_{lmo} &= +z_l \cdot \frac{m}{\sin(\theta)} P_l^m \cdot \cos(m\varphi) \hat{\boldsymbol{\theta}} - z_l \cdot \frac{\partial P_l^m}{\partial \theta} \cdot \sin(m\varphi) \hat{\boldsymbol{\varphi}} \\
 \mathbf{N}_{lme} &= \frac{1}{knr} z_l \cdot l(l+1) P_l^m \cdot \cos(m\varphi) \hat{\mathbf{r}} \\
 &\quad + \frac{1}{knr} \frac{\partial(rz_l)}{\partial r} \cdot \frac{\partial P_l^m}{\partial \theta} \cdot \cos(m\varphi) \hat{\boldsymbol{\theta}} - \frac{1}{knr} \frac{\partial(rz_l)}{\partial r} \cdot \frac{m}{\sin(\theta)} P_l^m \cdot \sin(m\varphi) \hat{\boldsymbol{\varphi}} \\
 \mathbf{N}_{lmo} &= \frac{1}{knr} z_l \cdot l(l+1) P_l^m \cdot \sin(m\varphi) \hat{\mathbf{r}} \\
 &\quad + \frac{1}{knr} \frac{\partial(rz_l)}{\partial r} \cdot \frac{\partial P_l^m}{\partial \theta} \cdot \sin(m\varphi) \hat{\boldsymbol{\theta}} + \frac{1}{knr} \frac{\partial(rz_l)}{\partial r} \cdot \frac{m}{\sin(\theta)} P_l^m \cdot \cos(m\varphi) \hat{\boldsymbol{\varphi}}
 \end{aligned} \tag{2.8}$$

where  $\hat{\mathbf{r}}$ ,  $\hat{\boldsymbol{\theta}}$ ,  $\hat{\boldsymbol{\varphi}}$  are the spherical unit vectors and the arguments of  $z_l(knr)$

and  $P_l^m(\cos(\theta))$  have been omitted. We introduce the angular functions

$$\begin{aligned}
 \mathbf{p}_{lme} &= l(l+1)P_l^m \cdot \cos(m\varphi) \hat{\mathbf{r}} \\
 \mathbf{p}_{lmo} &= l(l+1)P_l^m \cdot \sin(m\varphi) \hat{\mathbf{r}} \\
 \mathbf{m}_{lme} &= -\frac{m}{\sin(\theta)} P_l^m \cdot \sin(m\varphi) \hat{\boldsymbol{\theta}} - \frac{\partial P_l^m}{\partial \theta} \cdot \cos(m\varphi) \hat{\boldsymbol{\varphi}} \\
 \mathbf{m}_{lmo} &= \frac{m}{\sin(\theta)} P_l^m \cdot \cos(m\varphi) \hat{\boldsymbol{\theta}} - \frac{\partial P_l^m}{\partial \theta} \cdot \sin(m\varphi) \hat{\boldsymbol{\varphi}} \\
 \mathbf{n}_{lme} &= \frac{\partial P_l^m}{\partial \theta} \cdot \cos(m\varphi) \hat{\boldsymbol{\theta}} - \frac{m}{\sin(\theta)} P_l^m \cdot \sin(m\varphi) \hat{\boldsymbol{\varphi}} \\
 \mathbf{n}_{lmo} &= \frac{\partial P_l^m}{\partial \theta} \cdot \sin(m\varphi) \hat{\boldsymbol{\theta}} + \frac{m}{\sin(\theta)} P_l^m \cdot \cos(m\varphi) \hat{\boldsymbol{\varphi}}
 \end{aligned} \tag{2.9}$$

which fulfill the following orthogonality relations:

$$\begin{aligned}
 \hat{\mathbf{r}} \times \mathbf{p}_{lmp} &= 0 \\
 \hat{\mathbf{r}} \times \mathbf{m}_{lmp} &= \mathbf{n}_{lmp} \\
 \hat{\mathbf{r}} \times \mathbf{n}_{lmp} &= -\mathbf{m}_{lmp}
 \end{aligned} \tag{2.10}$$

where the index  $p = e, o$  indicates the respective parity. With this, the vector harmonics can be written in more compact form as

$$\begin{aligned}
 \mathbf{M}_{lmp} &= z_l \cdot \mathbf{m}_{lmp} \\
 \mathbf{N}_{lmp} &= \frac{1}{knr} z_l \cdot \mathbf{p}_{lmp} + \frac{1}{knr} \frac{\partial(rz_l)}{\partial r} \cdot \mathbf{n}_{lmp}
 \end{aligned} \tag{2.11}$$

With this basis of general solutions to of Eq.(2.1) and Eq.(2.2), the electric fields can be written as:

$$\mathbf{E}_{i,0,s} = A \sum_{l=0}^{\infty} \sum_{m=0}^l \sum_{p=e,o} i^l \frac{2l+1}{l(l+1)} \left( a_{lmp}^{i,0,s} \mathbf{M}_{lmp} - i b_{lmp}^{i,0,s} \mathbf{N}_{lmp} \right) \tag{2.12}$$

where  $A$  is a constant scalar and  $a_{lmp}^{i,0,s}$  and  $b_{lmp}^{i,0,s}$  are the scattering coefficients for  $\mathbf{E}_{i,0,s}$ , respectively. The prefactor  $i^l \frac{2l+1}{l(l+1)}$  and the phase  $-i$  between  $a_{lmp}^{i,0,s}$  and  $b_{lmp}^{i,0,s}$  are convention and simplify later calculations. The constant  $A$  is a scaling factor that is only required for quantitative computations and is neglected in the following ( $A = 1$ ). Eq.(2.12) represents the general form for the electric fields that describe single particle light scattering. For a particular scattering configuration, the resulting electric fields are found by



determining the scattering coefficients from suitable boundary conditions.

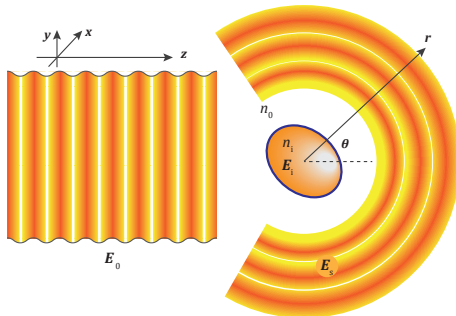


Figure 2.1: Single particle light scattering. The incident plane wave is denoted  $\mathbf{E}_0$ , the field inside the particle  $\mathbf{E}_i$  and the scattered field  $\mathbf{E}_s$ . Light scattering occurs as a consequence of the change in refractive index between  $n_0$  and  $n_i$  at the surface of the particle. The scattered wave propagates away from the particle in radial direction.

Often in light scattering experiments, the far field of the scattered light,  $\mathbf{E}_s(r \rightarrow \infty, \theta, \varphi)$ , is of particular interest. This limit describes the properties of the light that can be measured by detectors, which are typically placed far away from the particle compared to the wavelength of the light  $\lambda = \frac{2\pi}{k}$ . In the limit  $r \rightarrow \infty$ , only terms in highest order of  $r$  in Eq.(2.11) need to be considered:

$$\begin{aligned}
 \frac{1}{knr} \frac{\partial(rz_l)}{\partial r} &\rightarrow \frac{1}{kn} \frac{\partial z_l}{\partial r} \\
 \mathbf{M}_{lmp} &\rightarrow z_l \cdot \mathbf{m}_{lmp} \quad (\text{unchanged}) \\
 \mathbf{N}_{lmp} &\rightarrow \frac{1}{kn} \frac{\partial z_l}{\partial r} \cdot \mathbf{n}_{lmp}
 \end{aligned} \tag{2.13}$$

Using the asymptotic behavior of the radial functions  $z_l$ , we determine an additional constraint on the scattered far field. In the limit of  $r \rightarrow \infty$ , the

following relations hold:

$$\begin{aligned}
 j_l(knr) &\rightarrow \frac{1}{knr} \cos\left(knr - (l+1)\frac{\pi}{2}\right) \\
 y_l(knr) &\rightarrow \frac{1}{knr} \sin\left(knr - (l+1)\frac{\pi}{2}\right) \\
 h_l^{(1)}(knr) &:= j_l(knr) + iy_l(knr) \rightarrow \frac{(-i)^{l+1}}{knr} e^{iknr} \\
 h_l^{(2)}(knr) &:= j_l(knr) - iy_l(knr) \rightarrow \frac{(+i)^{l+1}}{knr} e^{-iknr}
 \end{aligned} \tag{2.14}$$

Here  $h_l^{(1)}$  and  $h_l^{(2)}$  are the spherical Hankel functions of the first and second kind, respectively, which in the far field represent outgoing and incoming spherical waves. By identifying  $h_l^{(1)}$  as the only function that describes the far field of a scatterer (the scattered light must have a propagation direction that points away from the particle), the following relations are obtained in the limit  $r \rightarrow \infty$ :

$$\begin{aligned}
 \mathbf{M}_{lmp} &\rightarrow h_l^{(1)} \cdot \mathbf{m}_{lmp} \\
 \mathbf{N}_{lmp} &\rightarrow \frac{1}{kn} \frac{\partial h_l^{(1)}}{\partial r} \cdot \mathbf{n}_{lmp} = ih_l^{(1)} \cdot \mathbf{n}_{lmp}
 \end{aligned} \tag{2.15}$$

This allows us to write the scattering far field in its final form ( $r \rightarrow \infty$ ):

$$\mathbf{E}_s(r, \theta, \varphi) \rightarrow \sum_{l=0}^{\infty} \sum_{m=0}^l \sum_{p=e,o} i^l \frac{2l+1}{l(l+1)} h_l^{(1)} (a_{lmp}^s \cdot \mathbf{m}_{lmp} + b_{lmp}^s \cdot \mathbf{n}_{lmp}) \tag{2.16}$$

where again the value of  $a_{lmp}^s$  and  $b_{lmp}^s$  depends on the scattering configuration. Since the present work investigates small droplets, an important case to discuss is scattering by a homogeneous sphere. The solution to this problem is known as Mie scattering.

## 2.2 Mie scattering

Consider a spherical, homogeneous particle illuminated by an incident plane wave  $\mathbf{E}_0$ . The resulting internal and scattered electric fields,  $\mathbf{E}_i$  and  $\mathbf{E}_s$ , can be determined using Mie theory<sup>50</sup>, which is recapitulated here. We choose Cartesian coordinates such that the origin lies at the center of the spherical

particle and  $z$  is the propagation axis of the incident plane wave which is linearly polarized along  $x$ . The incident field can then be written as sum of vector harmonics:

$$\begin{aligned} \mathbf{E}_0 &= e^{ikx} \hat{\mathbf{x}} = \sum_{l=0}^{\infty} i^l \frac{2l+1}{l(l+1)} \left( \mathbf{M}_{l1o}^{(1)} - i \mathbf{N}_{l1e}^{(1)} \right) \\ &= \sum_{l=0}^{\infty} i^l \frac{2l+1}{l(l+1)} \left( j_l \mathbf{m}_{l1o} - \frac{i}{kn_{0r}} j_l \mathbf{p}_{l1e} - \frac{i}{kn_{0r}} \frac{\partial(rj_l)}{\partial r} \mathbf{n}_{l1e} \right) \end{aligned} \quad (2.17)$$

where the superscript (1) indicates that the radial part of the vector harmonics is the Bessel function of the first kind,  $z_l = j_l$ . Eq.(2.17) is equivalent to stating that in Eq.(2.12), the scattering coefficients for the incident wave are

$$\begin{aligned} a_{lmp}^0 &= 1, \quad m = 1, p = o \\ b_{lmp}^0 &= 1, \quad m = 1, p = e \\ a_{lmp} &= b_{lmp} = 0 \quad \text{otherwise} \end{aligned} \quad (2.18)$$

Similarly, the scattered and internal fields can be written as

$$\begin{aligned} \mathbf{E}_s &= \sum_{l=0}^{\infty} i^l \frac{2l+1}{l(l+1)} \left( a_{l1o}^s \mathbf{M}_{l1o}^{(3)} - ib_{l1e}^s \mathbf{N}_{l1e}^{(3)} \right) \\ &= \sum_{l=0}^{\infty} i^l \frac{2l+1}{l(l+1)} \left( a_{l1o}^s h_l^{(1)} \mathbf{m}_{l1o} - b_{l1e}^s \frac{i}{kn_{0r}} h_l^{(1)} \mathbf{p}_{l1e} - b_{l1e}^s \frac{i}{kn_{0r}} \frac{\partial(rh_l^{(1)})}{\partial r} \mathbf{n}_{l1e} \right) \\ \mathbf{E}_i &= \sum_{l=0}^{\infty} i^l \frac{2l+1}{l(l+1)} \left( a_{l1o}^i \mathbf{M}_{l1o}^{(1)} - ib_{l1e}^i \mathbf{N}_{l1e}^{(1)} \right) \\ &= \sum_{l=0}^{\infty} i^l \frac{2l+1}{l(l+1)} \left( a_{l1o}^i \cdot j_l \mathbf{m}_{l1o} - b_{l1e}^i \cdot \frac{i}{kn_{1r}} j_l \mathbf{p}_{l1e} - b_{l1e}^i \frac{i}{kn_{1r}} \frac{\partial(rj_l)}{\partial r} \mathbf{n}_{l1e} \right) \end{aligned} \quad (2.19)$$

Here the superscript (3) indicates the Hankel function of the first kind (also called the Bessel function of the third kind). It was shown in the last section that only  $h_l^{(1)}$  describes the correct asymptotic behavior for the scattered field, hence the radial part of  $\mathbf{E}_s$  must be described by  $h_l^{(1)}$ . For the internal field, as  $r \rightarrow 0$ , all Bessel functions except the first kind possess a singularity,  $z_l \neq j_l : z_l \rightarrow \infty$ , hence the radial part of  $\mathbf{E}_i$  must be described by  $j_l$ .

The tangential component of the total electric field  $\mathbf{E}$  must be continuous on the particle's surface as dictated by energy conservation. If the particle and surrounding are nonmagnetic (and in the absence of free currents as per our general presumption), the same holds true for the magnetic field  $\mathbf{B}$  given by Eq.(2.3),  $\mathbf{B} = -i\frac{1}{kc}\nabla \times \mathbf{E}$ . Since the total electric fields outside and inside of the particle are given by  $\mathbf{E}_0 + \mathbf{E}_s$  and  $\mathbf{E}_i$ , respectively, it follows that

$$\begin{aligned} \mathbf{r} \times (\mathbf{E}_0 + \mathbf{E}_s)|_{|r|=R} &= \mathbf{r} \times \mathbf{E}_i|_{|r|=R} \\ \mathbf{r} \times (\nabla \times (\mathbf{E}_0 + \mathbf{E}_s))|_{|r|=R} &= \mathbf{r} \times (\nabla \times \mathbf{E}_i)|_{|r|=R} \end{aligned} \quad (2.20)$$

where it was used that  $\mathbf{r}$  is normal to the surface of the particle with radius  $R$ . Inserting Eq.(2.17) and Eq.(2.19) into Eq.(2.20) and equating coefficients for the basis vectors  $\mathbf{m}_{l1o}$  and  $\mathbf{n}_{l1e}$  using the properties listed in Eq.(2.5), Eq.(2.6) and Eq.(2.10), one obtains for each  $l$

$$\begin{aligned} a_{l1o}^s &= -\frac{j_l(Nx)\frac{\partial}{\partial \rho}(\rho \cdot j_l(\rho))|_{\rho=x} - j_l(x)\frac{\partial}{\partial \rho}(\rho \cdot j_l(\rho))|_{\rho=Nx}}{j_l(Nx)\frac{\partial}{\partial \rho}(\rho \cdot h_l^{(1)}(\rho))\Big|_{\rho=x} - h_l^{(1)}(x)\frac{\partial}{\partial \rho}(\rho \cdot j_l(\rho))|_{\rho=Nx}} \\ b_{l1e}^s &= -\frac{N^2 j_l(Nx)\frac{\partial}{\partial \rho}(\rho \cdot j_l(\rho))|_{\rho=x} - j_l(x)\frac{\partial}{\partial \rho}(\rho \cdot j_l(\rho))|_{\rho=Nx}}{N^2 j_l(Nx)\frac{\partial}{\partial \rho}(\rho \cdot h_l^{(1)}(\rho))\Big|_{\rho=x} - h_l^{(1)}(x)\frac{\partial}{\partial \rho}(\rho \cdot j_l(\rho))|_{\rho=Nx}} \\ a_{l1o}^i &= \frac{j_l(x)\frac{\partial}{\partial \rho}(\rho \cdot h_l^{(1)}(\rho))\Big|_{\rho=x} - h_l^{(1)}(x)\frac{\partial}{\partial \rho}(\rho \cdot j_l(\rho))|_{\rho=x}}{j_l(Nx)\frac{\partial}{\partial \rho}(\rho \cdot h_l^{(1)}(\rho))\Big|_{\rho=x} - h_l^{(1)}(x)\frac{\partial}{\partial \rho}(\rho \cdot j_l(\rho))|_{\rho=Nx}} \\ b_{l1e}^i &= \frac{N j_l(x)\frac{\partial}{\partial \rho}(\rho \cdot h_l^{(1)}(\rho))\Big|_{\rho=x} - N h_l^{(1)}(x)\frac{\partial}{\partial \rho}(\rho \cdot j_l(\rho))|_{\rho=x}}{N^2 j_l(Nx)\frac{\partial}{\partial \rho}(\rho \cdot h_l^{(1)}(\rho))\Big|_{\rho=x} - h_l^{(1)}(x)\frac{\partial}{\partial \rho}(\rho \cdot j_l(\rho))|_{\rho=Nx}} \end{aligned} \quad (2.21)$$

where  $x = kn_0R$  is the size parameter of the particle and  $N = \frac{n_i}{n_0}$  the dielectric contrast between particle and surrounding.

Eq.(2.21) holds true if both the particle and surrounding are nonmagnetic, i.e. their magnetic permeability  $\mu$  is equal to the vacuum permeability  $\mu_0$ . For magnetic particles or surroundings ( $\mu \neq \mu_0$ ), the interface condition for the magnetic field in Eq.(2.20) is slightly modified:

$$\mathbf{r} \times (\mathbf{H}_0 + \mathbf{H}_s)|_{|r|=R} = \mathbf{r} \times \mathbf{H}_i|_{|r|=R} \quad (2.22)$$

where  $\mathbf{H} = \frac{\mathbf{E}}{\mu}$  is the auxiliary magnetic field, or magnetic field strength vector, with the indices indicating internal, incident and scattered field as before. With this a more general expression for the scattering coefficients including the case of magnetic materials may be derived, using the same steps than discussed previously. However, this case is not relevant for the work in this thesis and is therefore not discussed further.

## 2.3 Optical force on a trapped particle

The optical trapping principle is based on the force that is exerted on a particle which is irradiated by a laser beam. The far field of the light scattering was previously discussed as it describes properties of the light which are relatively easy to access experimentally. Here we use the far field expressions to simplify the calculation of the optical force on a single particle for different beam configurations. In general, the optical force on a particle is given by

$$\mathbf{F} = \int_S d^3r \nabla \cdot \boldsymbol{\sigma} \quad (2.23)$$

where  $S$  is the volume of a sphere that completely encompasses the particle and  $\boldsymbol{\sigma}$  is the 3x3 Maxwell stress tensor with elements

$$\sigma_{ij} = \frac{1}{2} \cdot \frac{1}{\mu_0} \left( \frac{1}{c^2} \bar{E}_i E_j + \bar{B}_i B_j - \frac{1}{2} \left( \frac{1}{c^2} |\mathbf{E}|^2 + |\mathbf{B}|^2 \right) \delta_{ij} \right) \quad (2.24)$$

where  $\mathbf{E}$  and  $\mathbf{B}$  are the total electric and magnetic field, respectively, and the indices  $i, j = x, y, z$  indicate the respective field components. Eq.(2.23) and Eq.(2.24) are the average  $\mathbf{F}$  and  $\sigma_{ij}$ , respectively, on time scales  $T \gg \frac{1}{\omega}$ , which represent experimental conditions very well. Experimental time scales are usually much longer than typical periods of the light ( $\frac{1}{\omega} = 1.8$  fs for  $\lambda = 532$  nm).

We first consider as incident wave a laser beam with given width  $w$  which propagates along the  $z$  direction. Strictly speaking, an incident wave that is spatially confined along the lateral directions  $x$  and  $y$  and possesses a sharply defined momentum along the  $z$  axis violates the uncertainty principle between position and momentum of particles including light. One may however, to a good approximation, consider the incident beam to be a loosely focused

Gaussian beam

$$\mathbf{E}_0(x, y, z) = A \frac{w_0}{w(z)} \cdot e^{-\frac{r_\perp^2}{w(z)^2}} \cdot e^{i\left(kz + k\frac{r_\perp^2}{2R(z)} - \xi(z)\right)} \hat{\mathbf{x}} \quad (2.25)$$

where  $\hat{\mathbf{x}}$  indicates the polarization direction along  $x$ ,  $r_\perp = \sqrt{x^2 + y^2}$  is the distance from the beam axis  $z$ ,  $w(z) = w_0 \sqrt{1 + \left(\frac{z}{z_R}\right)^2}$  is the beam width as function of  $z$  with  $w_0$  the beam waist radius and  $z_R = \frac{1}{2}knw_0^2$  the Rayleigh range,  $R(z) = z \left(1 + \left(\frac{z}{z_R}\right)^2\right)$  the radius of beam curvature and  $\xi(z) = \arctan\left(\frac{z}{z_R}\right)$  the Gouy phase. The prefactor  $A$  is only necessary for quantitative computations and is subsequently neglected as was done before ( $A = 1$ ). For a given range of  $z$  we choose  $w_0$  sufficiently large such that  $z_R \gg z$  in this range. It follows that the Gaussian beam has an approximately constant width of  $w = w_0$  and a well defined momentum along  $z$  within the specified range. Eq.(2.25) can alternatively be expressed as Fourier series

$$\mathbf{E}_0(x, y, z) = \iint dk_x dk_y e^{ik_z z} \mathbf{g}_0(k_x, k_y) \cdot e^{ik_x x} e^{ik_y y} \hat{\mathbf{x}} \quad (2.26)$$

where  $k_z = \sqrt{k^2 - k_x^2 - k_y^2}$  with  $k = |\mathbf{k}| = \frac{\omega}{c}$ . The Fourier components of the incident wave are given by

$$g_0(k_x, k_y) = -\frac{z_R}{(2\pi)^{\frac{1}{2}} k} \cdot e^{-\frac{z_R}{2k}(k_x^2 + k_y^2)} \quad (2.27)$$

Let now the sphere  $S$  be sufficiently large such that its radius  $R_S$  fulfills  $R_S \gg w_0$  and  $kR_S \gg 1$ , that is, at distance  $R_S$  to the particle the far field expressions for  $\mathbf{E}_s$  and  $\mathbf{B}_s$  are valid. In this limit Eq.(2.23) is equivalent to

$$\mathbf{F} = \frac{1}{c} (W_{\text{abs}} + W_{\text{scat}}) \cdot \hat{\mathbf{z}} - \int_{\partial S} d^2r \frac{\epsilon_0}{2} |\mathbf{E}_s|^2 \hat{\mathbf{r}} \quad (2.28)$$

where  $\partial S$  is the surface of the sphere  $S$ ,  $\hat{\mathbf{r}}$  is the radial unit vector which coincides with the surface normal of  $\partial S$  and  $\hat{\mathbf{z}}$  is the unit vector along  $z$ , which coincides with the propagation direction of the incident wave. The

absorption and scattering rates are given by

$$\begin{aligned}
 W_{\text{abs}} &= c \int_{\partial S} d^2r \frac{\epsilon_0}{2} |\mathbf{E}_0 + \mathbf{E}_s|^2 \\
 W_{\text{scat}} &= c \int_{\partial S} d^2r \frac{\epsilon_0}{2} |\mathbf{E}_s|^2
 \end{aligned}
 \tag{2.29}$$

The derivation of this equation is presented in the appendix in Section 10.1. Eq.(2.28) allows one to calculate the optical force exerted by an incident beam described by  $\mathbf{E}_0$  on a particle if the electric far field  $\mathbf{E}_s$  is known. In the case of a spherical particle, expressions for the electric far field have already been derived in Eq.(2.16) and Eq.(2.21). These expressions strictly apply only to incident plane waves, however, may be used as an approximation for spatially confined beams in some applications presented in later chapters.

We can extend Eq.(2.28) to several incoherent incident beams by taking the sum over the individual contributions. For example, counter-propagating optical tweezers (CPT) used for particle trapping, as presented in later chapters, consist of two counter-propagating beams, where beam 1 propagates along  $\mathbf{k}_1 = k\hat{z}$  and beam 2 along  $\mathbf{k}_2 = -k\hat{z}$ . For a general configuration of laser beams, each beam propagating along a direction  $\mathbf{k}_i$ , the resulting optical force on a spherical particle can be calculated according to

$$\mathbf{F}_{\text{tot}} = \sum_i \mathbf{F} \left[ \mathbf{E}_s^{(\mathbf{k}_i)} \right]
 \tag{2.30}$$

where  $\mathbf{F} \left[ \mathbf{E}_s^{(k\hat{z})} \right]$  is the force given by Eq.(2.28) and  $\mathbf{F} \left[ \mathbf{E}_s^{(\mathbf{k}_i)} \right]$  is obtained from Eq.(2.28) by replacing the propagation direction  $\hat{z}$  with  $\hat{\mathbf{k}}_i$ . The scattered field  $\mathbf{E}_s^{(\mathbf{k}_i)}$  is obtained by rotating  $\mathbf{E}_s^{(k\hat{z})}$ , given by Eq.(2.16) and Eq.(2.21), such that  $\mathbf{k}_i$  is mapped onto  $\hat{z}$ . For spherical particles, the optical force of an incoherent superposition of incident plane waves is independent of the polarization of the partial beams.

It is worth noting that for a coherent superposition of incident beams, Eq.(2.28) is generally not applicable for calculating the optical force, and Eq.(2.23) has to be used instead. However, if we remain in the limit where all coherent partial beams have approximately the same propagation direction, a modified version of Eq.(2.28) can be used. Let  $\mathbf{E}_s^{(\mathbf{k}_i)}$  be the scattered field of the partial beam propagating along  $\mathbf{k}_i \approx k\hat{z}$ . The scattered field  $\mathbf{E}_s^{(\mathbf{k}_i)}$  is

obtained by rotating  $\mathbf{E}_s^{(k\hat{z})}$ , given by Eq.(2.16) and Eq.(2.21), such that  $\mathbf{k}_i$  is mapped onto  $\hat{\mathbf{z}}$ . The optical force is found by first taking the coherent sum of partial scattering fields

$$\mathbf{E}_{s,\text{tot}} = \sum_i \mathbf{E}_s^{(k_i)} \quad (2.31)$$

and then using Eq.(2.28), with  $\mathbf{E}_s = \mathbf{E}_{s,\text{tot}}$ . This result can be used to derive a more accurate expression of the optical force on a particle in the focus of a Gaussian beam, when the plane wave approximation is not sufficiently accurate. Using Eq.(2.26) and identifying  $\mathbf{k}_i = (k_x/k_y/k_z)$  as the propagation direction of each individual plane wave component, the total electric scattering field to be used in Eq.(2.28) is

$$\mathbf{E}_{s,\text{Gauss}} = \iint dk_x dk_y \mathbf{g}_0(k_x, k_y) \cdot \mathbf{E}_s^{(k_i)} \quad (2.32)$$

where  $\mathbf{g}_0(k_x, k_y)$  is given by Eq.(2.27) and the discrete sum in Eq.(2.31) was replaced by the integral over  $dk_x dk_y$ .

Finally, the results of Eq.(2.30) and Eq.(2.32) can be combined to describe the optical force exerted by several incoherent Gaussian beams irradiating the particle:

$$\mathbf{F}_{\text{tot}} = \sum_i \mathbf{F} \left[ \mathbf{E}_{s,\text{Gauss}}^{(k_i)} \right] \quad (2.33)$$

where  $\mathbf{k}_i$  is the central axis of the partial Gaussian beam and  $\mathbf{F} \left[ \mathbf{E}_{s,\text{Gauss}}^{(k_i)} \right]$  is obtained by replacing  $\hat{\mathbf{z}}$  with  $\hat{\mathbf{k}}_i$  and  $\mathbf{E}_s = \mathbf{E}_{s,\text{Gauss}}^{(k_i)}$  in Eq.(2.28).

## 2.4 Holography

Holography derives its name from the fact that it allows the full 3 dimensional (3d) image of an object ("holos" = whole) to be captured in a 2d picture ("graphy"=graph). Interesting as a concept, holography has an additional advantage over other imaging techniques in that it requires no optics to focus the image, and was originally developed to overcome the resolution limit of electron lenses in electron microscopy<sup>52</sup>. From a physical point of view, the 3 dimensional image of an object is determined by its local electromagnetic



scattered field, represented by  $\mathbf{E}_s$ , where local means in proximity to the surface of the object. Imaging techniques like photography fail to capture the full information on  $\mathbf{E}_s$  as they only record the scattered intensity,  $I_s \sim |\mathbf{E}_s|^2$  on a 2d screen. From the recorded picture one may determine the amplitude  $|\mathbf{E}_s|$  of the scattered light, however, the information on the phase of  $\mathbf{E}_s$  is lost. The recorded photograph is therefore perceived as a 2 dimensional projection of the original object. In holographic imaging, both amplitude and phase are recorded in a 2 dimensional picture. From this picture the local scattering field, that is the 3d image, of the object, can be obtained. The principle of holographic imaging and reconstruction is discussed here. A practical algorithm for holography reconstruction is presented in the appendix in Section 10.2.

Let again be  $\mathbf{E}_0$  the incident light illuminating the particle and  $\mathbf{E}_s$  be the scattered field of the particle that is to be imaged, as shown in Fig.(2.2). As before, we define  $x$  to be the polarization axis of  $\mathbf{E}_0$ . The intensity of the electric field outside of the particle is then proportional to

$$\begin{aligned} |\mathbf{E}_0 + \mathbf{E}_s|^2 &= |\mathbf{E}_0|^2 + |\mathbf{E}_s|^2 + \mathbf{E}_0 \cdot \bar{\mathbf{E}}_s + \bar{\mathbf{E}}_0 \cdot \mathbf{E}_s \\ &= |E_0|^2 + |E_s|^2 + E_0 \bar{E}_s + \bar{E}_0 E_s \end{aligned} \quad (2.34)$$

where  $E_0$  and  $E_s$  are the  $x$  components of  $\mathbf{E}_0$  and  $\mathbf{E}_s$ , respectively. Subtracting  $|E_0|^2$  from Eq.(2.34) and then dividing by  $|E_0|^2$  yields a scalar field

$$h := \frac{1}{|E_0|^2} (|\mathbf{E}_0 + \mathbf{E}_s|^2 - |E_0|^2) = \frac{|\mathbf{E}_s|^2}{|E_0|^2} + \frac{E_0}{|E_0|^2} \bar{E}_s + \frac{\bar{E}_0}{|E_0|^2} E_s \quad (2.35)$$

which, when multiplied with  $E_0$ , results in

$$E_h := E_0 \cdot h = \frac{|\mathbf{E}_s|^2}{|E_0|^2} E_0 + \frac{E_0^2}{|E_0|^2} \bar{E}_s + E_s \quad (2.36)$$

These mathematical operations are in part redundant, however, they reflect the steps in the process to create a physical hologram: The scattered light of the particle is superimposed with the incident light, and the intensity of the total electric field,  $|\mathbf{E}_0 + \mathbf{E}_s|^2$ , is recorded on a screen. The background hologram  $|E_0|^2$  is obtained by recording the light intensity without the particle present and is used to subtract the background and normalize the image. This background subtracted and normalized intensity pattern is the hologram  $h$ . One may then imagine  $h$  being printed as a black and white pattern on an transparent that has the same area than the screen that recorded the

hologram. Let  $A$  denote this area. The pattern leads to an effective modulation of the transparency of  $A$  according to  $h$ . If the same incident wave  $\mathbf{E}_0$  is used to illuminate  $A$ , the pattern generates an electric field  $E_h$  similar to  $E_s$ , albeit with two additional contributions according to Eq.(2.36). It is shown at the end of this section that the additional contributions in Eq.(2.36) are negligible and that  $E_h$  is equivalent to  $E_s$  for all practical purposes. Two important observations are discussed before: First, the use of a incident wave that is polarized along  $x$  allows for the measurement of the  $x$  component of the scattered field only. The  $y$  component of the scattered field could be obtained by repeating the measurement with a incident wave polarized along  $y$ . This is superfluous though for the purpose of creating an image of the particle, which is typically well represented by a single polarization component of the scattered field. Second, since experimentally we only measure  $h$  within the area  $A$ , it follows that Eq.(2.36) determines  $E_h$  only inside  $A$ . However, this information uniquely defines the whole field  $E_h$ , and therefore also  $E_s$ , as is shown here. Using the Kirchhoff-Helmholtz integral theorem<sup>53</sup>, the following identity is obtained for  $E_h$ :

$$E_h(\mathbf{r}) = -\frac{1}{4\pi} \int_A d^2s E_h(\mathbf{s}) \frac{\partial}{\partial \mathbf{n}} \left( \frac{e^{-ik|\mathbf{s}-\mathbf{r}|}}{|\mathbf{s}-\mathbf{r}|} \right) - \frac{e^{-ik|\mathbf{s}-\mathbf{r}|}}{|\mathbf{s}-\mathbf{r}|} \frac{\partial E_h}{\partial \mathbf{n}} \quad (2.37)$$

where  $\mathbf{s}$  denotes the position on the screen  $A$  with  $\frac{\partial}{\partial \mathbf{n}}$  the derivative along the normal of  $A$ , and  $k = \frac{\omega}{c}$  as before. This identity holds strictly true only if  $A$  describes a closed surface around the particle and  $\mathbf{r}$  is a point inside the volume enclosed by  $A$ . For practical purposes however, we consider Eq.(2.37) valid if  $A$  is sufficiently large to capture the essential part of the hologram, and  $\mathbf{r}$  is a point that is close to the particle in the configuration shown in Fig.(2.2). Using Eq.(2.37) the scattered electric field can be determined in the local volume where the particle resides, as further discussed in Section 10.2. The field outside of this local volume is not of interest for the purpose of imaging the particle, however, it can be nevertheless determined by propagating the local scattered field using the wave equation Eq.(2.1). Therefore from the knowledge of  $E_h$  inside the area  $A$ , the full information on  $E_s$  can be deduced.

Let us now revisit the additional contributions in Eq.(2.36). Microscopic particles typically have small scattering intensities,  $|E_s| \ll |E_0|$ , and the first term on the right-hand side is negligible. The second term is essentially equal to  $\bar{E}_s$ , which creates the image of a particle that is mirrored in space. In our setup, the incident wave is spherical to a good approximation,  $E_i(\mathbf{r}) \sim \frac{1}{|\mathbf{r}|} e^{ik|\mathbf{r}|}$ . For a spherical incident wave, the mirrored image, or twin image, is

located centro-symmetrically to the original object relative to the center of the spherical incident wave<sup>54,55</sup>, see Fig.(2.2). Due to the spatial separation between particle and twin, the intensity of the original scattered wave at the position of the particle is generally larger than the scattered field of the twin. In our holography setup, the spatial separation between the particle and its twin is made large enough so that the scattered field of the twin image is not significant inside the local volume where the particle resides. When reconstructing the image of the original particle using Eq.(2.37), the contribution of the twin image can therefore be neglected.

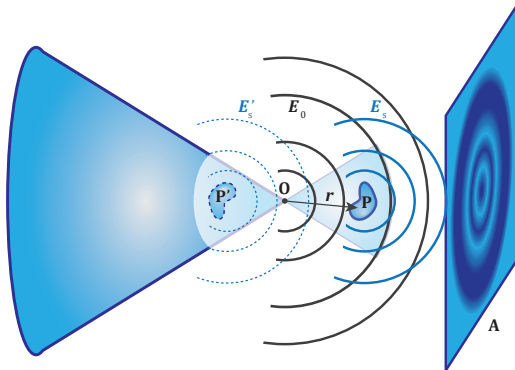


Figure 2.2: Principle of holographic imaging. The incident wave  $\mathbf{E}_0$  is generated by a focused laser beam and is superimposed on the scattered wave  $\mathbf{E}_s$  of the particle  $\mathbf{P}$ . The superposition is then recorded on the screen  $A$ . The wavefront of the incident beam propagating towards  $A$  and the scattered wave in the far field limit are spherical to a good approximation. From the hologram, the scattered wave in the local volume of the particle can be reconstructed. The arrow  $\mathbf{r}$  indicates a point inside this volume. The distances between  $\mathbf{P}$  and  $\mathbf{O}$  and between  $\mathbf{P}$  and  $A$  are not to scale. The distance between  $\mathbf{P}$  and  $\mathbf{O}$  is typically only approximately  $100\ \mu\text{m}$ . The twin image, an artifact in the reconstruction of the hologram, is indicated by  $\mathbf{P}'$ , and the corresponding scattered wave by  $\mathbf{E}'_s$ .

## 2.5 Raman scattering

Raman scattering is a type of inelastic light scattering that arises due to the specific interaction between a incident photon and a molecule of the

particle. As shown in Fig.(2.3), photon energies that do not correspond to an electronic transition may instead excite the molecule to a virtual state. The molecule then relaxes back to the electronic ground state by emitting a photon. Raman scattering occurs when the initial and final state have a different vibrational level, and thus the emitted photon has a different wavelength than the incident one. Stokes-Raman scattering occurs when the final state is higher in energy than the initial one, and therefore the emitted photon is lower in energy than the incident one. The opposite case is termed Anti-Stokes-scattering. Since at any finite temperature, the lower energy states are more populated than the higher energy states, the Stokes-Raman scattering is generally more intense than the Anti-Stokes scattering<sup>56</sup>.

Emission from Raman scattering may be stimulated by a second incoming photon if the second photon energy matches the transition energy to one of the electronic ground states. This process is called stimulated Raman scattering<sup>57</sup> to differentiate it from the spontaneous Raman scattering explained above. In aerosol particles, stimulated Raman scattering is relevant when the light intensity from the spontaneous Raman scattering is sufficiently large inside the particle. Typically, this condition is met when photons emitted by spontaneous Raman scattering have wavelengths that resonate inside the particle. For spherical particles, these resonance wavelengths are given by the wavelengths where one or several scattering coefficients in Eq.(2.21) become large. At resonance, these emitted photons form standing waves, or whispering gallery modes<sup>58</sup>, on the surface of the particle. This greatly enhances the local photon density and consequently the scattering rate.

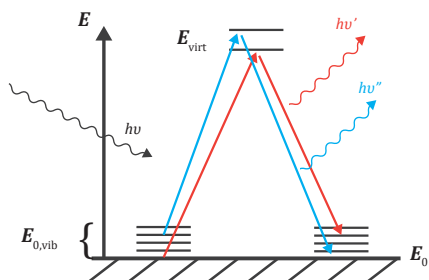


Figure 2.3: Principle of Raman scattering. The incoming photon excites a molecule in the particle from the electronic ground state  $E_0$  to a virtual state  $E_{virt}$ . The molecule relaxes back to the electronic ground state by emitting a photon. Raman scattering occurs when initial and final state have a different vibrational level. The red arrows indicate Stokes-Raman scattering which releases a photon that is lower in energy,  $h\nu' < h\nu$ . The blue arrows indicate Anti-Stokes-Raman scattering which releases a photon that is higher in energy,  $h\nu'' > h\nu$ .

## 3 Experimental methods

This chapter describes the setup for optical trapping of single particles and their characterization. The characterization methods explained here are the determination of size and refractive index of homogeneous and spherical particles, the determination of size and shape of non-spherical particles and the investigation of their molecular composition. The principle of mass measurement and the procedure to measure single particle mass are explained in Chapter 4.

### 3.1 Optical trapping

Single particles are isolated and immobilized in a dual beam trap<sup>17,33,42</sup>, consisting of two focused counter-propagating Gaussian beams. For the experiments in this thesis, two similar designs for these counter-propagating optical tweezers (CPT) have been implemented, which are described in detail in Chapters 5, 6 and 8. Both designs share in essence the layout that is shown in Fig.(3.1). A continuous 532 nm laser beam is expanded by an approximate factor of 4 and then split by a polarizing beam splitter into the two trapping beams. The trapping beams are aligned on a single axis and focused into the trapping cell on two points on the axis that are separated by 10–500  $\mu\text{m}$ . Between the two focii, a point of stable equilibrium is formed at which particles are trapped due to the optical forces exerted by the laser beams. This is illustrated in Fig.(3.2), where a simulation of the optical forces acting on a spherical, non-absorbing particle in proximity of the beam focii is shown for typical experimental parameters. Experimentally, it is found that spherical and elliptical particles with relatively low eccentricities can be trapped for extended periods of time (weeks if needed). For this, the particles need to have an approximate size of 0.5–10  $\mu\text{m}$  and should have no strong absorption

at the wavelength of the trapping laser.

The path difference between the two trapping beams of the CPT is much longer than the coherence length of the laser (7 mm), therefore coherence effects between the two beams are negligible. For stable trapping a nominal laser power between 100–3000 mW is used. The effective power of the laser light incident onto the particle is lower due to losses along the laser beam path and depends on the respective setup.

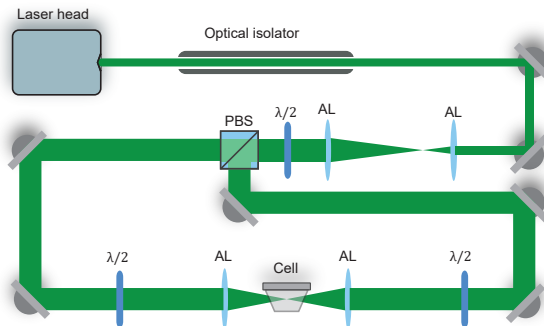


Figure 3.1: Counter-propagating tweezers setup. A continuous 532 nm laser beam is expanded using two aspherical lenses (AL) before it is split by a polarizing beam splitter (PBS). Before the PBS a halfwave plate ( $\lambda/2$ ) is used to adjust the power ratio of the two beams to 50%/50%. The two beams are aligned on a single axis and focused down into the trapping cell. The polarization direction of the trapping beams is adjusted with a ( $\lambda/2$ ) plate each. The optical isolator prevents optical feedback from the trapping beam back into the laser. Figure adapted from Reich et al.<sup>59</sup> under Copyright 2021 Society of Photo-Optical Instrumentation Engineers (SPIE).

## 3.2 Trapping cells

The particles investigated in this thesis were optically trapped inside a trapping cell in either a gaseous or liquid medium. The trapping cell enables the precise control of the ambient conditions in which the particles are trapped, in particular the temperature and chemical composition, and for gases, the relative humidity (RH) of the surrounding.

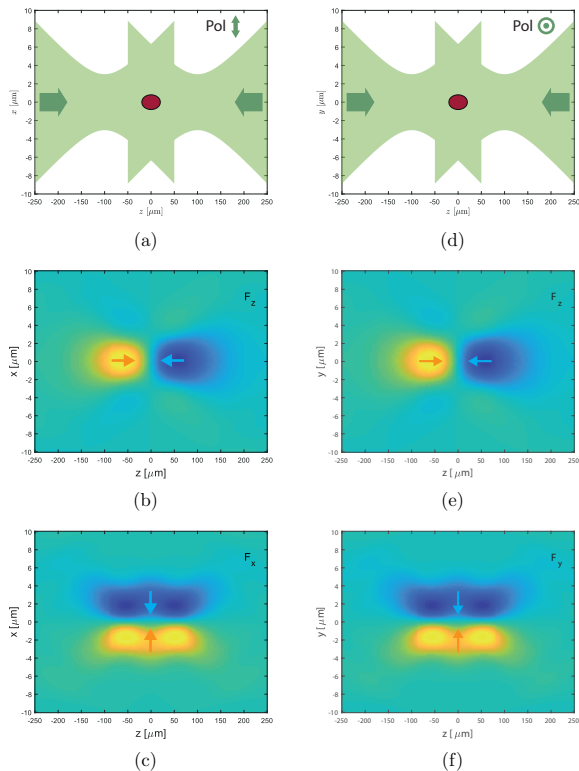


Figure 3.2: Principle of particle trapping with focused dual Gaussian beams. (a) Shape of the beams in proximity of the focus spots. The contour indicates the  $1/e$  width of the Gaussian profile. The  $z$  axis is defined as the beam propagation axis and the  $x$  axis is the polarization axis of the beams. (b) Simulated optical force along  $z$ . (c) Simulated optical force along  $x$ . The arrows indicate the direction of the optical force in regions where its magnitude is large. The third force component,  $F_y$ , vanishes in the  $x-z$  plane for symmetry reasons. (d)-(f) show the corresponding data in the  $y-z$  plane. The simulation was done as explained in Section 2.3. The relevant parameters for the Gaussian trapping beams are: wavelength  $\lambda = 532$  nm, trapping beam waist  $w_0 = 3.05$   $\mu\text{m}$ , separation between foci of beam 1 and beam 2  $z_{\text{sep}} = 100$   $\mu\text{m}$ . For the particle, the radius was  $R = 1.5$   $\mu\text{m}$ , and the refractive index  $n_i = 1.420$ .



For trapping in the gas phase, two similar cell designs were used, which are shown in Fig.(3.3). Each cell has an inlet for the gas used as surrounding medium for particle trapping, which was nitrogen for all measurements reported here. The inlet is sufficiently far away from the designated trapping position so that the constant flow of nitrogen does not affect the trapping stability during measurements. The relative humidity of the inflowing nitrogen gas is controlled by mixing a line of wet and a line of dry nitrogen in specified ratios. The ratio is adjusted using a gas mass flow controller (Bronkhorst F-211 CV) (MFC) in each of the lines, and the wet nitrogen line is humidified by leading the gas through a cylinder with water after the MFC. The RH in the cell adjusts to the RH of the inflowing nitrogen in a matter of seconds to minutes depending on the difference between cell and inflow. The inlet for the particle stream is directed towards the designated trapping position. Once a suitable particle has been trapped, the remainder of the particles in the cell is flushed through the outlet of the cell by redirecting the nitrogen line through the particle inlet. The temperature and RH of the cell, nitrogen line and the outlet are monitored with a temperature/RH sensor (Sensirion SHT35) each.

The nitrogen lines are built from copper and stainless steel tubings, connected with stainless steel fittings (Swagelok) and turned on and off using ball valves (Swagelok). The particle inlet line is built from the same pieces. For the cell design in Fig.(3.3a) the last segment of the particle inlet before the cell is a teflon tube for greater flexibility. All parts of the gas flow system except the cell and the teflon tube are vacuum tight to minimize contamination of the gas flow. The cell and teflon tube are airtight. The system is tested for leaks prior to the measurements and a stable nitrogen flow during the trapping of a particle ensures that the gas at undetected leaks is flowing outwards to further minimize the risk of contamination of the gas lines.

The cell design for trapping in the liquid phase is shown in Fig.(3.4). The cell is filled by pumping purified water through an inlet in the cell wall using a high performance liquid chromatography pump (Hitachi L-6200A). Once the cell is full, solid particles are introduced via the opening at the top of the cell, which is sealed watertight afterwards. Once a suitable particle is trapped, water is pumped through the inlet to flush the remainder of the particles through the outlet near the bottom of the cell. Light scattering is collected through the front and back windows of the cell.

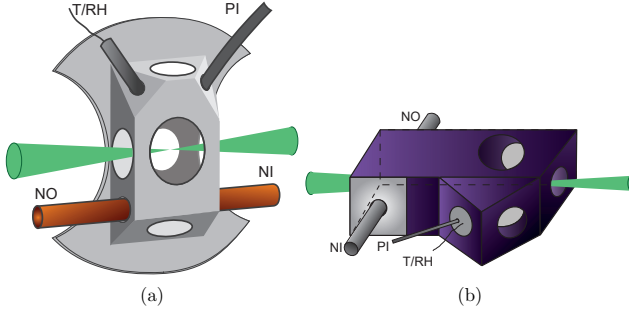


Figure 3.3: Cell designs for optical trapping in nitrogen gas. (a) Cell design 1 (adapted from Reich et al.<sup>60</sup> under copyright CC-BY4.0) and (b) Cell design 2. A steady gas flow enters and exits the cell via the nitrogen inlet (NI) and outlet (NO), respectively, to provide stable ambient conditions for particle trapping. The particles are introduced into the cell via the particle inlet (PI). Temperature and RH inside the cell are measured with a sensor (T/RH). The green cones indicate the two trapping beams, which enter the cell through the side windows.

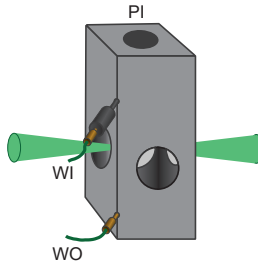


Figure 3.4: Cell design for optical trapping in water. The cell is filled with purified water through the water inlet (WI) prior to introducing solid particles for trapping via the particle inlet (PI), which is shut watertight thereafter. Once a suitable particle is trapped, the remainder of the particles is flushed through the water outlet (WO) by pumping water through the WI. The green cones indicate the two trapping beams, which enter the cell through the side windows.

### 3.3 Particle generation

Liquid droplets for trapping in the gas phase were generated from solution using a commercial atomizer (TSI 3076) attached to a nitrogen gas line at approximately 1.5 bar overpressure. The atomizer generates a constant flow of polydisperse aerosol droplets which is delivered to the trapping cell by a system of copper tubings. For aqueous liquid droplets the nitrogen line is humidified by letting it flow through a water filled cylinder prior to the atomizer to ensure particles reach the cell in a liquid state. In the trapping cell the droplets coagulate at the trapping position until the desired size is reached, upon which the remainder of the particles is flushed out as previously explained. Table (3.1) lists typical examples for the type of droplets that are used for the experiments, as well as the stock solutions from which they were generated. The concentration of the aqueous stock solution does not influence the eventual concentration of the generated particles, as they quickly equilibrate according to the relative humidity inside the cell.

Stock solution	Molar.	Company/Catalogue no.
NaCl + H <sub>2</sub> O	0.5 M	Merck/1.06404.1000
NaCl + H <sub>2</sub> O	1.0 M	Merck/1.06404.1000
MgCl <sub>2</sub> hexahyd. + H <sub>2</sub> O	1.0 M	Sigma-Aldrich/63068-250G
MgSO <sub>4</sub> + H <sub>2</sub> O	1.0 M	Sigma-Aldrich/M7506-500G
Glycine + H <sub>2</sub> O	1.0 M	Sigma-Aldrich/G7126-100G
Glycine + H <sub>2</sub> O	2.0 M	Sigma-Aldrich/G7126-100G
Squalane	pure	Acros Organics/111-01-3

Table 3.1: Stock solutions for generation of liquid droplets.

For trapping in the liquid phase, commercially available monospheres were used as solid particles. Two different types were used for the experiments: SiO<sub>2</sub> with radius 2.5  $\mu\text{m}$  (Bangs Laboratories SS05003) and BoroSiO<sub>2</sub> with radius 4.0  $\mu\text{m}$  (Thermo Fisher 9008). The particles were suspended in purified water and introduced into the cell as previously explained.

## 3.4 Particle characterization methods

The size, shape, optical properties and chemical composition of the trapped particles are determined in-situ and non-destructively using the methods described in this section.

### 3.4.1 Two-dimensional angular optical scattering spectrum

The light of the trapping laser beams that is elastically scattered by the trapped particle carries information about the particle's size, shape and refractive index. To determine whether a particle is spherical, the scattered intensity is measured as a function of scattering and azimuthal angle and the resulting two-angular optical scattering spectrum (TAOS spectrum) is fitted with simulations using Mie theory (Eq.(2.16) and Eq.(2.21)). To measure the TAOS spectrum, the elastically scattered laser light is collected under a scattering angle of  $90 \pm 24^\circ$  using an objective (Mitutoyo 20x NA 0.42) and loosely focused on a CMOS camera (Thorlabs DCC1545M) as depicted in Fig.(3.5). Alternatively, by introducing a polarizing beam splitter before the focusing lens, the scattered light is split into two orthogonal polarization components which are recorded individually. Fig.(3.6) shows the measured and simulated TAOS spectrum of a spherical NaCl droplet for both polarization directions. By matching the characteristic vertical stripes between simulation and experiment, the size of the particle can be determined. This technique however requires that the refractive index of the particle is known approximately, and the uncertainty from matching the measured image to the simulated one is typically large for the purpose of the experiments reported here. For the determination of the size and the refractive index of a spherical particle, broad-band light scattering is a more accurate method, as explained in the next section.

### 3.4.2 Broad-band light scattering

Spherical particles act as cavities for the incoming light, amplifying the scattered intensity if the wavelength matches the resonance condition in Eq.(2.21) (see also discussion of stimulated Raman scattering in Section 2.5), while the

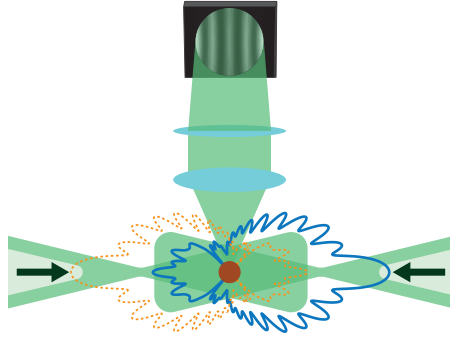


Figure 3.5: Schematic of the two-dimensional angular optical scattering (TAOS) measurement configuration. The solid blue and dashed red curves show the relative scattered intensity of the left and right beam, respectively, as a function of scattering angle (log scale). The light is collected under a scattering angle of  $90 \pm 24^\circ$  and recorded by camera.

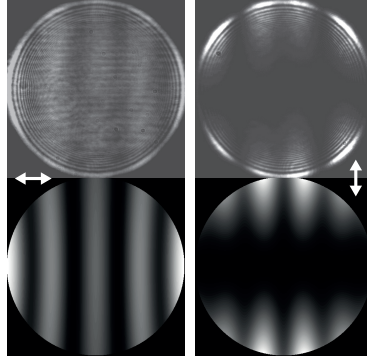


Figure 3.6: Measured and simulated two-dimensional angular optical scattering (TAOS) spectra of a spherical NaCl droplet. The white arrows indicate the respective polarization direction of the recorded light. The scattering geometry is as described in the text and both trapping beams are polarized parallel to the scattering plane. For the simulated images in the lower panels the parameters are as follows: Radius  $R = 1.540 \mu\text{m}$ , wavelength  $\lambda = 532 \text{ nm}$ , refractive index  $n = 1.400$ , mean scattering angle  $\theta = 90^\circ$ , numerical aperture  $\text{NA} = 0.42$ .

spectral intensity for other wavelengths is significantly lower. The wavelengths at which the light is at resonance depends critically on the size of the spherical particle and the refractive index. The broad-band light scattering (BLS) technique<sup>32</sup> makes use of this fact by illuminating a trapped spherical particle using a light source with a broad spectral range and recording the spectrum of the scattered light, as shown in Fig.(3.7). The spectrum of the scattered light is analyzed using Mie theory (Eq.(2.16) and Eq.(2.21)) and fitted by optimizing radius and refractive index of the spherical particle to obtain the size of the particle.

As light source a fiber coupled broad-band lamp (EnergetiQ LDLS EQ-99X) with a spectral range of 190–2500 nm was used. The light is focused on the trapped particle using a reflective objective (Edmund Optics ReflX 89722) and the scattered light is collected under a scattering angle of  $\theta$  using a second objective of the same type, before it is fiber coupled into a spectrometer. The scattering angle  $\theta$  varies for different experiments and is specified in the respective chapter. Typical values are  $\theta = 45^\circ$ ,  $90^\circ$  and  $112.5^\circ$ . The BLS spectrum is analyzed in the range 300–500 nm, which represents a compromise between the characteristic features of the BLS spectrum which are more abundant at small wavelengths and the spectral intensity of the light source which is higher for larger wavelengths. To avoid any contribution from the elastically scattered trapping laser light at 532 nm, the collected scattered light from the particle is filtered using two short pass filters (Edmund Optics 500 nm #49825) before the recording spectrograph.

For fitting of the experimental BLS spectra with Mie theory, the radius  $R$  and refractive index  $n$  of the particle are used as fit parameters. To represent the wavelength dependence of the refractive index in the model, the Cauchy expansion for  $n(\lambda)$  is used up to second order,

$$n(\lambda) = n_0 + n_1 \cdot \left( \left( \frac{\lambda_0}{\lambda} \right)^2 - 1 \right) \quad (3.1)$$

where  $n_0$  and  $n_1$  are the first two coefficients of the Cauchy expansion and  $\lambda_0 = 475$  nm is the reference wavelength at which  $n(\lambda_0) = n_0$ . The choice of  $\lambda_0$  is somewhat arbitrary. Here it is chosen to be at the approximate maximum of the light source emission in the range 300–500 nm. The simulated spectra are compared to the measurements and from visual inspection, the best set  $R$ ,  $n_0$  and  $n_1$  are determined. Fig.(3.8) shows an example of a fitted BLS spectrum of a spherical Squalane droplet measured with a high sensitiv-

---

ity, low noise spectrograph (Andor SR-303i-A). The range of fit parameters for which good agreement between simulation and experiment is observed defines the fit uncertainty. For the experiments reported here the accuracy of the radius determination is typically better than 1%.

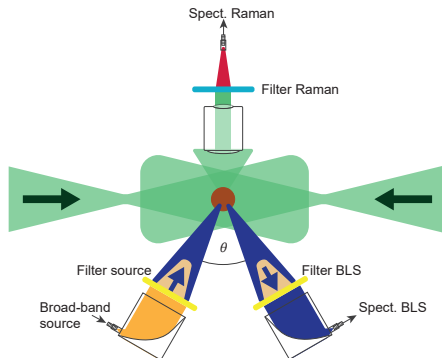


Figure 3.7: Setup for broad-band light scattering (BLS) and Raman spectroscopy. For BLS spectroscopy, a light source with a broad emission spectrum is focused on the trapped particle (brown circle) and the elastically scattered light is collected under a scattering angle of  $\theta$  and coupled into the BLS spectrograph (Spect. BLS). The elastically scattered light from the trapping beams, which are incident on the particle from the directions indicated by the green arrows, is filtered out before the BLS spectrograph (Filter BLS). For Raman spectroscopy, the scattered light from the trapping beams is collected under an angle of  $90^\circ$  and coupled into the spectrograph (Spect. Raman). The emission of the broad-band light source in the spectral range of the analyzed Raman shifts is suppressed (Filter source). Additionally, the elastically scattered components of the trapping beams and the broad-band light source outside the spectral range of the analyzed Raman shifts are filtered out (Filter Raman) before the Raman spectrometer to avoid oversaturation of the spectrometer sensor.

### 3.4.3 Raman scattering

A small portion of the scattered trapping laser light consists of emission from Stokes or Anti-Stokes scattering processes in the trapped particle<sup>61,62</sup>, which can be used as fingerprints for detection of molecular species in the particle. Although the cross-sections for these processes are much smaller than for the

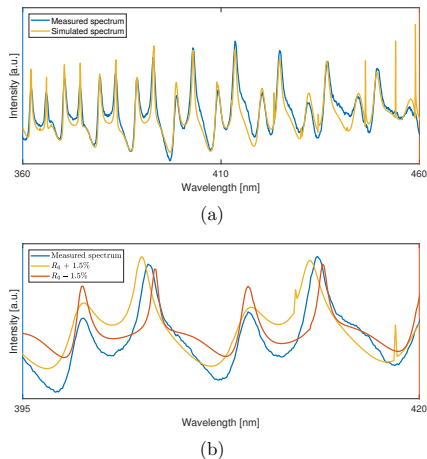


Figure 3.8: Fitted broad-band light scattering (BLS) spectrum of a Squalane droplet (a) Measured spectrum with best fit for  $R_0 = 1.838 \mu\text{m}$ ,  $n_0 = 1.460$  and  $n_1 = 0.020$  (b) Measured spectrum with fits that do not match the measured spectrum precisely. Here the simulated spectra are obtained by fixing the radius parameter to a value that is 1.5% larger or lower than  $R_0$ , respectively, and  $n_0$  and  $n_1$  are optimized for best agreement under this constraint. The discrepancy between measurement and fits is best observed at the separation of two neighboring peaks, which are smaller or larger than in the experimental spectrum, respectively. The radius determination is typically better than 1%.

elastic scattering, this signal can be measured using a high sensitivity, low noise spectrograph (Andor KY-328i-A) due to the high intensity of the laser beam (100–3000 mW). The scattered trapping laser light is collected under a mean scattering angle of  $90^\circ$  using a relatively high aperture objective (Mitutoyo 20x NA 0.42) before being fiber coupled into the spectrograph using a focusing lens, as illustrated in Fig.(3.7). The elastically scattered light is filtered out using two notch filters (Edmund Optics 532 nm, OD 6 #86120) in succession before the focusing lens. In an alternative setup, the Raman scattered light is collected by the same objective than the TAOS spectrum and separated from the elastically scattered light by a dichroic beam splitter (AHF 532 nm LPD02-532RU-25).

For analysis of the Stokes shifts in the Raman spectra the range 500–



$3800\text{ cm}^{-1}$  is used, corresponding approximately to a wavelength range of 550–670 nm. This range allows in particular to probe the water content of the trapped particles (water O–H stretch mode  $3000\text{--}3600\text{ cm}^{-1}$ ).

If Raman spectrometry is performed simultaneously with BLS measurements, the BLS light has to be filtered out as it would perturb the Raman signal. To this end, two additional filters, a short pass filter (Thorlabs 750 nm FES0750) and a long pass filter (Edmund Optics 525 nm #84738) are introduced with the notch filters before the Raman spectrograph and a short pass filter (Edmund Optics 500 nm #84693) is used at the exit of the broad-band light source to suppress the emission in the Raman range.

### 3.4.4 Holography

Conventional holography setups require two identical light beams. The first is used to illuminate the object in order to generate the scattering field,  $\mathbf{E}_s$ . The second is superimposed on the scattering field to create the interference pattern that is then recorded as hologram. However, microscopic particles typically only scatter a small fraction of the incident light. As a consequence, the incident light beam is only marginally perturbed by the scattering field of the particle. In-line holography<sup>33,63,64</sup> makes use of this fact by using a single beam to both illuminate the object and serve as a reference beam for creating the hologram of the object. We have recently setup the first digital in-line holography imaging system for trapped aerosol particles<sup>33</sup>. A schematic of experimental setup is shown in Fig.(3.9). To create the light beam, the output of a fiber coupled diode laser (Toptica Photonics DL Pro) with wavelength  $\lambda = 379\text{ nm}$  is collimated perpendicularly to the trapping laser beams, before being focused using an objective (Mitutoyo 20x NA 0.42) approximately 100–200  $\mu\text{m}$  before the trapped particle. The diverging laser beam and the superimposed scattered field of the particle that together form the hologram are then recorded using a high-speed camera (IDT OS7-V3-S3). This setup allows us to follow the shape changes upon phase transition of the trapped particle with time resolution up to 240  $\mu\text{s}$ <sup>33</sup>.

The performance of the digital in-line holography setup is analyzed in a series of test images. For this series, instead of a particle in the trap, a composition of standardized particles with known size and shape deposited on a microscope glass slide are holographically imaged. This allows us to compare the reconstructions to the images obtained from conventional microscopy.

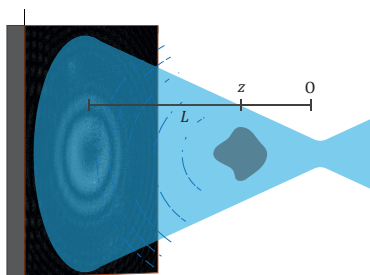


Figure 3.9: Digital in-line holography setup. The microscopic object is illuminated by a diverging laser beam which is recorded together with the scattered field of the object on camera. The camera screen is positioned at a distance  $L \approx 21.5$  mm from the focus (O) of the diverging beam. The object is located on the axis of the laser beam at a typical distance of  $z = 100 \mu\text{m}$  from O.

Fig.(3.10) shows a comprehensive example. The holograms and the digital reconstruction of a triangle of three polystyrene latex (PSL) spheres (Magsphere PS004UM) are shown as well as the conventional microscopy image. The raw hologram is subtracted by a background image which is obtained by moving the glass slide such that no particle are in the hologram field of view. The background subtracted hologram is then used for reconstruction using the algorithm explained in Section 10.2. The reconstruction renders the correct relative positions of the three spheres with respect to the direct image. The reconstructed distances between the centers of the three monospheres are  $4.17 \mu\text{m}$ ,  $4.25 \mu\text{m}$  and  $4.29 \mu\text{m}$ , which agrees with the diameter range of the PSL monospheres of  $4.05 \pm 0.40 \mu\text{m}$ . From the test series it is concluded that the digital in-line holography setup is suitable to image microscopic objects with a faithful representation of the object's shape and a size accuracy of at least 10%.

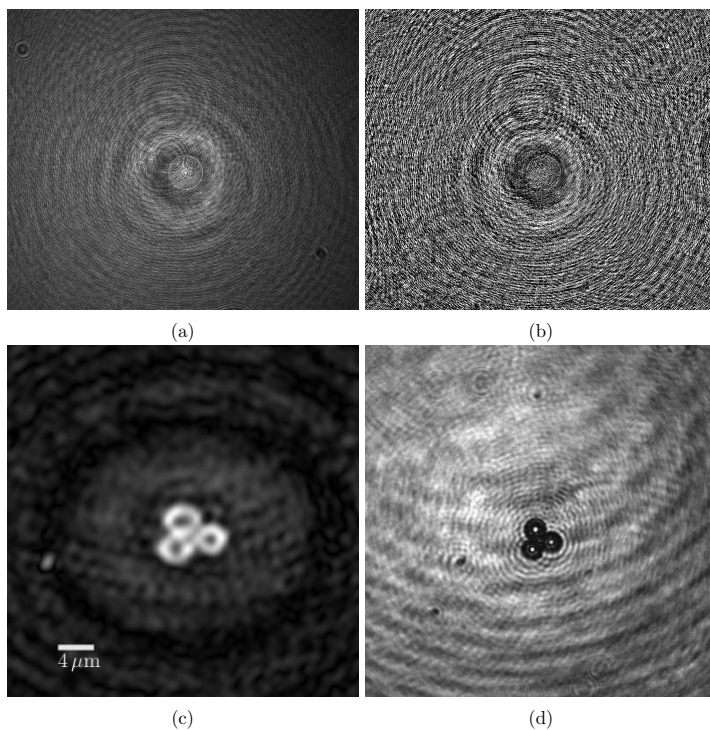


Figure 3.10: Microscopy image and holographic reconstruction of three polystyrene spheres ( $R = 2.0 \pm 0.2 \mu\text{m}$ ) stuck together on a microscope slide. (a) raw hologram, (b) background subtracted hologram, (c) digital reconstruction of the background subtracted hologram, (d) object under the conventional microscope. The scale in (c) is indicated by the white bar.

## 4 Single particle mass measurement

Single particle mass measurement methods are typically based on one of two principles: Either the mass is determined by measuring the force necessary to sustain the particle against gravity (determination of the gravitational mass) or by measuring the particle's response to some known applied force (determination of the inertial mass). The former principle is used by electrodynamic balances (EDB)<sup>44,65,66</sup>, where the charged particle is suspended using calibrated electric fields. Determination of the inertial mass on the other hand has been realized using a variety of techniques: Measurement of the power spectral density of the Brownian motion of a particle<sup>36,38,40</sup>, measurement of the induced oscillation amplitude of a particle in a modulated trapping potential<sup>36,41</sup> and measurement of the eigenfrequency of charged particle oscillation in calibrated electromagnetic fields<sup>67-70</sup> are commonly used methods. Each of these techniques has their specific range of applications, however, only a few are suited for volatile particle species like liquid droplets. As explained in Chapter 1, mass measurements of droplets can be used for determination of the hygroscopicity of a given particle species. Traditionally, the EDB has represented the state-of-the art mass measurement device for single liquid droplets for the last few decades<sup>45,65,71</sup>, with alternative setups with comparable performance only emerging recently<sup>38,39</sup>. However, the current single droplet methods are limited to particle sizes well above the atmospherically important submicrometer size range.

The technique that we present here overcomes this size limitation and facilitates mass measurements down to submicrometer particles with accuracies of a few percent in mass<sup>60</sup>. This method is based on the excitation of harmonic oscillation of an optically trapped particle and the precise measurement of the induced dynamics. From these measurements, the particle's inertial mass can be determined using a harmonic oscillator model. As an additional feature, the implementation into previous optical trapping setups is straightforward. This allows us to combine the mass measurement with other characterization

methods (see Chapter 3).

## 4.1 Optical trap for mass measurement

The optical trapping setup for single particle mass measurement is very similar to the basic CPT presented in Chapter 3, Fig.(3.1). The only modification concerns the halfwave plate before the PBS. The halfwave plate rotates the linear polarization of the laser beam to a fixed angle of  $45^\circ$  to the PBS, in order to split the beam at a power ratio of 50%/50%. It is replaced with an electro-optic modulator (ConOptics 350-50-01 RP), which enables us to electronically control the ratio of the power splitting. This principle is illustrated in Fig.(4.1). The EOM acts as a Pockels cell for the incoming laser beam, which is polarized at  $45^\circ$  to the crystalline axes of the EOM. Upon exiting, the slow beam component has accumulated a phase delay  $\alpha$  with respect to the fast component, which depends linearly on the voltage applied to the EOM. If  $V_0$ ,  $V_{\text{eq}}$  are the voltages required for  $\alpha = 0$ ,  $\alpha = \frac{\pi}{2}$ , respectively, the power splitting between the horizontal and vertical beam component after the EOM can be written as

$$\begin{aligned} P_1(V_{\text{EOM}}) &= P_0 \cdot \cos^2\left(\frac{1}{2}\alpha(V_{\text{EOM}})\right) = P_0 \cdot \cos^2\left(\frac{\pi}{4} \cdot \frac{V_{\text{EOM}} - V_0}{V_{\text{eq}} - V_0}\right) \\ P_2(V_{\text{EOM}}) &= P_0 \cdot \sin^2\left(\frac{1}{2}\alpha(V_{\text{EOM}})\right) = P_0 \cdot \sin^2\left(\frac{\pi}{4} \cdot \frac{V_{\text{EOM}} - V_0}{V_{\text{eq}} - V_0}\right) \end{aligned} \quad (4.1)$$

where  $V_{\text{EOM}}$  is the voltage applied to the EOM and  $P_0$  is the total power of the laser beam. From Eq.(4.1) it is evident that  $V_{\text{eq}}$  is the voltage required for even power splitting, i.e.  $P_1(V_{\text{eq}}) = P_2(V_{\text{eq}}) = \frac{1}{2}P_0$ .

The ratio between  $P_1$  and  $P_2$  determines the trapping position between the foci of the two trapping beams of the CPT. In accordance with Chapter 3, and Fig.(3.2) in particular, we denote the axis of the trapping beams as  $z$  axis and choose the origin of the coordinate system  $(x/y/z) = (0/0/0)$  as the trapping position when  $P_1 = P_2 = P_{\text{eq}}$ . Harmonic oscillation of the trapped particle along the  $z$  axis is then induced by modulating  $V_{\text{EOM}}$  in a small range around  $V_{\text{eq}}$ :

$$V_{\text{EOM}}(t) = V_{\text{eq}} + S_0 \sin(2\pi ft) \quad (4.2)$$

where  $S_0$  is the modulation signal amplitude (with  $S_0 \ll V_{\text{eq}} - V_0$ , see also

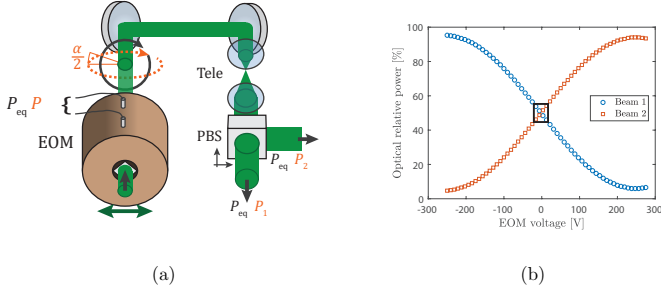


Figure 4.1: Trapping beams modulation. (a) Section of the trapping beam path. The electro-optical modulator (EOM) acts as a variable wave plate for the incoming, linearly polarized light. Upon exiting the EOM, the polarization is elliptical with ratio  $\tan(\frac{1}{2}\alpha)$  between the two axes of the ellipse. This ratio determines the power splitting of the beam at the polarizing beam splitter (PBS) after the telescope (Tele). In (a), the situation is shown for two different voltages applied to the EOM: in black for  $V_{\text{Eq}}$ , which leads to circular polarization and even power splitting,  $P_1 = P_2 = P_{\text{eq}}$ , and in red for a voltage  $V$  slightly smaller than  $V_{\text{eq}}$  for which  $0 < \alpha < \frac{\pi}{2}$  and therefore  $P_1 > P_2$ . (b) Measured relative beam powers of the two trapping beams as function of voltage applied to the EOM. The rectangle indicates the typical modulation range during experiments.

Fig.(4.1b)) and  $f$  the modulation frequency. The time dependent trapping position along the  $z$  axis,  $z_0$ , is then well approximated by a first order Taylor series:

$$\begin{aligned}
 z_0(V_{\text{EOM}}(t)) &= \underbrace{z_0(V_{\text{eq}})}_0 + \left. \frac{dz_0}{dV_{\text{EOM}}} \right|_{V_{\text{EOM}}=V_{\text{eq}}} \cdot (V_{\text{EOM}}(t) - V_{\text{eq}}) \\
 &= Z_0 \sin(2\pi ft)
 \end{aligned} \tag{4.3}$$

where  $Z_0 = S_0 \cdot \frac{dz_0}{dV_{\text{EOM}}}$  at  $V_{\text{EOM}} = V_{\text{eq}}$  is the modulation amplitude. For symmetry reasons, the trapping position along the lateral dimensions  $x$  and  $y$  remains unaffected by the modulation. The particle dynamics that result from the modulation of  $z_0$  follow a driven damped harmonic oscillator model.

## 4.2 Harmonic oscillator model

The dynamics of a particle in an optical trap are governed by Newton's equation of motion. The particle experiences an optical force due to the interaction with the trapping beams. In the vicinity of the trapping position  $\mathbf{r}_0 = (0/0/z_0)$ , the trapping potential is well approximated by a harmonic potential. The resulting optical force is therefore

$$\begin{aligned}\mathbf{F}_{\text{opt}}(\mathbf{r}) &= -\nabla V_{\text{opt}} = -\frac{1}{2} \nabla \left( (\mathbf{r} - \mathbf{r}_0)^\dagger K (\mathbf{r} - \mathbf{r}_0) \right) = \\ &= -K \cdot (\mathbf{r} - \mathbf{r}_0)\end{aligned}\tag{4.4}$$

where  $K$  is the trap stiffness of the optical trap represented by the diagonal Hessian matrix of  $V_{\text{opt}}$  at  $\mathbf{r}_0$ . Note that  $z_0$ , and therefore  $\mathbf{r}_0$ , are time dependent in a modulated optical trap according to Eq.(4.3). In the limit of small modulation signal amplitudes however,  $K$  can be assumed constant, i.e.  $K(\mathbf{r}_0) \approx K(\mathbf{0})$ .

A second force term arises from the damping of the particle due to the surrounding medium. In a first description we assume a uniform laminar flow of the fluid around the particle moving through the medium and discuss the corrections for real particles later in Section 4.3. In the uniform laminar regime the drag force is proportional to the particle speed, which is written as

$$\mathbf{F}_{\text{drag}} = -\gamma \dot{\mathbf{r}}\tag{4.5}$$

where  $\gamma$  is the laminar drag coefficient. For spherical particles, including liquid droplets, the drag coefficient can be calculated using Stokes' law:

$$\gamma = 6\pi\mu R\tag{4.6}$$

where  $R$  is the radius of the particle and  $\mu$  is the dynamic viscosity of the surrounding medium. The interaction between particle and medium gives further rise to a stochastic force, responsible for the Brownian motion. However, as explained later, this random force can be neglected for the purpose of the mass measurement experiments.

With Eq.(4.4) and Eq.(4.5), Newton's equation of motion for a particle with

mass  $m$  can be written as

$$m\ddot{\mathbf{r}} = \mathbf{F}_{\text{opt}} + \mathbf{F}_{\text{drag}} = -K \cdot (\mathbf{r} - \mathbf{r}_0) - \gamma\dot{\mathbf{r}} \quad (4.7)$$

Eq.(4.7) represents three independent equations for the coordinates  $x$ ,  $y$  and  $z$ . Since there is no driving force along  $x$  and  $y$ , the relevant particle dynamics is captured by the equation for  $z$ :

$$m\ddot{z} = -k \cdot (z - z_0) - \gamma\dot{z} \quad (4.8)$$

where  $k = K_{zz} = \frac{d^2V_{\text{opt}}}{dz^2}$  at  $z = z_0$ , or equivalently by

$$\ddot{z} + 2\pi\Gamma_0\dot{z} + 4\pi^2\Omega_0^2 z = 4\pi^2\Omega_0^2 z_0 \quad (4.9)$$

Here we have introduced the eigenfrequency  $\Omega_0$  and the damping rate  $\Gamma_0$  of the harmonic oscillator according to

$$\Omega_0 = \frac{1}{2\pi} \sqrt{\frac{k}{m}} \quad (4.10)$$

$$\Gamma_0 = \frac{1}{2\pi} \frac{\gamma}{m} \quad (4.11)$$

Eq.(4.9) describes a one-dimensional driven and damped harmonic oscillator. The solutions of interest are periodic in  $T = \frac{1}{f}$ , where  $f$  is the frequency of the optical trap modulation in accordance with Eq.(4.2). We therefore make a Fourier ansatz for the particle position  $z$ ,

$$z(t) = \sum_{n=-\infty}^{\infty} \hat{z}_n e^{2\pi i n f t} \quad (4.12)$$

where  $\hat{z}_n$  is the  $n$ -th Fourier component of  $z$ . Similarly, using Eq.(4.3), we have for the time dependent trapping position

$$z_0(t) = Z_0 \sin(2\pi f t) = \frac{-iZ_0}{2} e^{2\pi i f t} + \frac{iZ_0}{2} e^{-2\pi i f t} \quad (4.13)$$

Inserting Eq.(4.12) and Eq.(4.13) into Eq.(4.9), two different sets of equations



are obtained:

$$\begin{aligned}
 n = \pm 1 : \\
 (-f^2 \pm if\Gamma_0 + \Omega_0^2) \hat{z}_{\pm 1} &= \mp i \frac{Z_0 \Omega_0^2}{2} \\
 n \neq \pm 1 : \\
 (-n^2 f^2 \pm in f \Gamma_0 + \Omega_0^2) \hat{z}_n &= 0
 \end{aligned} \tag{4.14}$$

Thus the only non-vanishing Fourier components are

$$\hat{z}_{\pm 1} = \mp \frac{i}{2} A e^{\mp i \varphi} \tag{4.15}$$

where

$$A = Z_0 \frac{\Omega_0^2}{\sqrt{(\Omega_0^2 - f^2)^2 + (\Gamma_0 f)^2}} \tag{4.16}$$

$$\varphi = \arctan \left( \frac{\Gamma_0 f}{\Omega_0^2 - f^2} \right) \tag{4.17}$$

are the amplitude and phase of the particle oscillation, respectively. Substituting back into Eq.(4.12) yields the solution

$$\begin{aligned}
 z(t) &= \frac{-i}{2} A e^{2\pi i f t - \varphi} + \frac{i}{2} A e^{-(2\pi i f t - \varphi)} \\
 &= A \sin(2\pi f t - \varphi)
 \end{aligned} \tag{4.18}$$

The predicted amplitude  $A$  and phase  $\varphi$  of the particle oscillation in a modulated optical trap is shown in Fig.(4.2) as function of  $f$  for typical values of  $\Omega_0$  and  $\Gamma_0$  using Eq.(4.16) and Eq.(4.17), respectively. For small micrometer and submicrometer sized particles at atmospheric conditions, the oscillation is typically largely overdamped ( $\Gamma_0 \gg \Omega_0$ ). As a consequence,  $A$  depends mostly on the ratio  $\Omega_0^2/\Gamma_0$ , even if the individual values of  $\Omega_0^2$  and  $\Gamma_0$  change by a factor larger than 2, as shown in Fig.(4.2). The same is not true for  $\varphi$ , for which  $\Omega_0$  can be determined independently from  $\Gamma_0$  via the relation  $\varphi(\Omega_0) = \frac{\pi}{2}$ . This observation is of key importance for the determination of the particle mass from experimental data as explained later in Section 4.4.

Finally, the impact of the Brownian motion on the observed particle dynamics is estimated. The magnitude of the induced particle oscillation described by

Eq.(4.18) is characterized by  $Z_0$ , which has typical values in the range 10–50  $\mu\text{m}$ . The power spectral density of the Brownian motion on the other hand is given by<sup>38</sup>

$$S_{\text{Brown}}(f) = \frac{k_B T}{2\pi^2 \gamma} \frac{\Gamma_0^2}{(\Omega_0^2 - f^2)^2 + (\Gamma_0 f)^2} \quad (4.19)$$

where  $k_B$  is the Boltzmann constant and  $T$  the temperature. An upper bound of  $S_{\text{Brown}}$  is obtained by considering a small particle in nitrogen gas, which has low viscosity. Setting  $R = 300 \text{ nm}$  and  $\mu_{\text{N}_2} = 17.6 \text{ }\mu\text{Pa}\cdot\text{s}$  in Eq.(4.6) yields  $\gamma = 9.6 \cdot 10^{-11} \text{ kg s}^{-1}$ . The particle mass is estimated by assuming a low density of  $\rho = 800 \text{ kg m}^{-3}$  which yields  $m = \frac{4}{3}\pi R^3 \rho = 9.0 \cdot 10^{-17} \text{ kg}$ . It follows that  $\Gamma_0 = \frac{1}{2\pi} \frac{\gamma}{m} = 1.7 \cdot 10^5 \text{ Hz}$ . A low typical value for  $\Omega_0 = 1500 \text{ Hz}$  for small particles, and a temperature  $T = 300 \text{ K}$  is assumed. The resulting upper estimate for the mean amplitude of the Brownian motion is then

$$\begin{aligned} \langle z \rangle^{\text{max}} &= \left( \int_{-\infty}^{\infty} df S_{\text{Brown}}^{\text{max}}(f) \right)^{\frac{1}{2}} \\ &= 0.7 \text{ }\mu\text{m} \end{aligned} \quad (4.20)$$

Therefore even at extreme conditions, the amplitude of the Brownian motion is more than one order of magnitude lower than the induced oscillation amplitude, and may be neglected.

### 4.3 Damping model corrections

The uniform laminar damping force defined by Eq.(4.5) and Eq.(4.6) describes the real damping of a spherical particle under certain assumptions only, which are discussed in the following. Where necessary, corrections to the damping model are introduced. These corrections affect the numerical results of the calculated particle dynamics, however, they do not change the concept of the derivations shown in the previous section.

Laminar flow requires that the Reynolds number of the fluid surrounding the particle is smaller than the critical Reynolds number, which has an approximate value of  $10^{72}$ . An upper bound for the Reynolds number in our experiments can be found by assuming a particle with a large radius of  $R = 5 \text{ }\mu\text{m}$  modulated at high frequency of  $f = 5000 \text{ Hz}$  and large os-

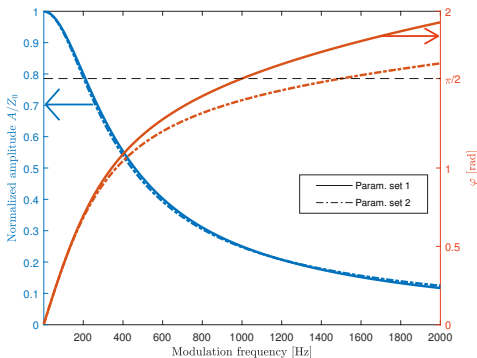


Figure 4.2: Simulated oscillation amplitude and phase of a particle trapped in a modulated harmonic potential. The normalized amplitude  $A/Z_0$  and the phase  $\varphi$  are shown for two sets of typical parameters, set 1:  $\Omega_0 = 1000$  Hz,  $\Gamma_0 = 4000$  Hz and set 2:  $\Omega_0 = 1500$  Hz,  $\Gamma_0 = 9000$  Hz. The ratio  $\frac{\Omega_0}{\Gamma_0}$  is equal for both sets. The two amplitude graphs virtually coincide with each other, while the phase graphs are clearly distinguished and cross the horizontal line at  $\frac{\pi}{2}$  at their respective eigenfrequency,  $f = \Omega_0 = 1000$  Hz, 1500 Hz.

cillation amplitude of  $Z_0 = 50 \mu\text{m}$  resulting in a maximum particle speed of  $v = Z_0 \cdot 2\pi f = 1.6 \text{ m s}^{-1}$ . Note that for the real oscillation amplitude,  $A \ll Z_0$  at high frequencies, therefore the calculated speed is a great overestimate. The corresponding Reynolds number is

$$\text{Re}^{\max} = \frac{\rho_{\text{N}_2} v 2R}{\mu_{\text{N}_2}} = 1.2 \quad (4.21)$$

where  $\rho_{\text{N}_2} = 1.2 \text{ kg m}^{-3}$  and  $\mu_{\text{N}_2} = 17.6 \mu\text{Pa s}$  are the density and viscosity of nitrogen gas, respectively. Thus even at extreme conditions, the flow around the particle is laminar in very good approximation.

The oscillatory motion of the particle gives rise to additional force terms due to the inertia of the fluid surrounding the particle. These correction terms depend on the particle speed as well as acceleration and, for a spherical

particle with radius  $R$  modulated at a frequency  $f$ , can be written as<sup>72</sup>

$$F_{\text{drag}}^{\text{corr}} = -6\pi\mu R \cdot \sqrt{\frac{\pi\rho}{\mu}} R\sqrt{f} \dot{z} - \frac{2\pi}{3}\rho R^3 \left( \frac{9}{2}\sqrt{\frac{\mu}{\pi\rho}} \frac{1}{R\sqrt{f}} + 1 \right) \ddot{z} \quad (4.22)$$

where  $\mu$ ,  $\rho$ , are the viscosity and density of the surrounding fluid, respectively. Using  $\gamma = 6\pi\mu R$  and introducing the abbreviation  $\nu = \sqrt{\frac{\pi\rho}{\mu}}$ , the following terms are defined:

$$\begin{aligned} \gamma_1 &= \gamma \cdot \nu R \\ \gamma_2 &= \gamma \cdot \frac{2}{9} (\nu R)^2 \end{aligned} \quad (4.23)$$

with which Eq.(4.22) is simplified to

$$F_{\text{drag}}^{\text{corr}} = -\gamma_1 f^{\frac{1}{2}} \dot{z} - \left( \gamma_1 f^{-\frac{1}{2}} + \gamma_2 \right) \frac{1}{2\pi} \ddot{z} \quad (4.24)$$

The analogous calculation of the particle dynamics as presented in the previous section yields the corrected oscillation amplitude and phase:

$$A = Z_0 \frac{\Omega_0^2}{\sqrt{\left( \Omega_0^2 - (1 + \Gamma_2) f^2 - \Gamma_1 f^{\frac{3}{2}} \right)^2 + \left( \Gamma_0 f + \Gamma_1 f^{\frac{3}{2}} \right)^2}} \quad (4.25)$$

$$\varphi = \arctan \left( \frac{\Gamma_0 f + \Gamma_1 f^{\frac{3}{2}}}{\Omega_0^2 - (1 + \Gamma_2) f^2 - \Gamma_1 f^{\frac{3}{2}}} \right) \quad (4.26)$$

where  $Z_0$ ,  $\Omega_0$  and  $\Gamma_0$  are as defined before and  $\Gamma_{1,2} = \frac{1}{2\pi} \frac{\gamma_{1,2}}{m}$  are the corresponding damping term corrections. Note that the free parameters of the model are only  $Z_0$ ,  $\Omega_0$  and  $\Gamma_0$  as in the basic model discussed previously, since from Eq.(4.23) it follows that  $\Gamma_1$  and  $\Gamma_2$  are connected to  $\Gamma_0$  by constants depending on the surrounding medium ( $\mu$  and  $\rho$ ) and independently determined quantities ( $R$ ). Fig.(4.3) shows the predicted phase according to Eq.(4.26) for a similar set of typical experimental parameters as discussed previously. For comparison, the simulated data is fitted with the simple model, Eq.(4.17), and the best fits are shown as well. From the comparison it is seen that the simple model is able to describe qualitatively the simulated data very well, however, cannot retrieve the simulation parameters  $\Omega_0$  and  $\Gamma_0$  very accurately, with deviations ranging between 4–10%. Therefore, the extended damping model is necessary to accurately determine eigenfrequency  $\Omega_0$  and damping rate  $\Gamma_0$  from experimental data.

---

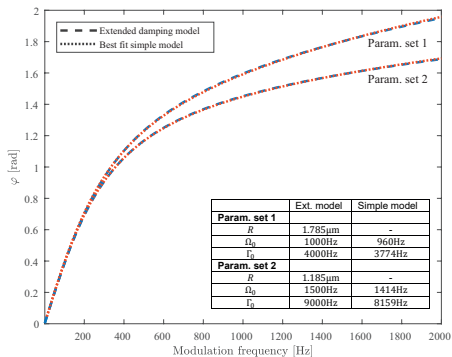


Figure 4.3: Comparison between models with and without damping term corrections. The corrected phase  $\varphi$  is plotted (dashed lines) for two sets of typical parameters  $R$ ,  $\Omega_0$  and  $\Gamma_0$  and compared to best fits obtained by the simple model (dotted lines). The inset table shows the simulation parameters for the extended model and the corresponding best fit values for the simple model. In the simple model, the phase does not depend on the radius  $R$  of the particle.

Finally, the treatment of the drag force within fluid dynamics applies strictly only to particles which have a size much larger than the mean free path of the surrounding medium. For particles approaching this characteristic length scale, the non-continuous distribution of the atoms and molecules in the surrounding medium leads to a reduction of the drag force experienced by the particle. This reduction is treated empirically by introduction of a Cunningham slip correction factor<sup>73</sup>:

$$\begin{aligned}
 \gamma &\rightarrow \frac{1}{C_c(R)} \gamma, \\
 \Gamma_0 &\rightarrow \frac{1}{C_c(R)} \Gamma_0, \\
 C_c(R) &= 1 + C_0 \cdot \frac{\lambda_{\text{free}}}{R}
 \end{aligned} \tag{4.27}$$

where  $\lambda_{\text{free}}$  is the mean free path of the surrounding medium and  $C_0$  is an empirical constant. For a particle trapped in nitrogen, the mean free path is assumed to be equal to air at room temperature,  $\lambda_{\text{free}} = 68 \text{ nm}$ . Literature values of  $C_0$  range from 1.142–1.257<sup>74</sup>. Largely independent of the exact

value of  $C_0$ , the Cunningham slip correction factor leads to a reduction of  $\gamma$  and  $\Gamma_0$  of 4–16 % for particles with radii  $R = 2.0$ – $0.5 \mu\text{m}$ , respectively.

## 4.4 Experimental setup for mass measurement

Measurement of the induced particle dynamics for accurate retrieval of the particle mass requires precise tracking of the particle oscillation during the modulation of the optical trap. To this end, a part of the laser light scattered by the particle is collected and focused on a position sensing photodiode (PSP, Thorlabs PDP90A), as illustrated in Fig.(4.4). The oscillation  $z(t)$  of the particle leads to a corresponding oscillation of the particle image  $z'(t)$  on the photosensitive area of the PSP. The position of the image is tracked by measuring the differential signal (diff) between the four electrodes of the PSP and dividing it by the total signal (sum) of the four electrodes. The position signal is recorded by a lock-in amplifier (Zurich instruments MFLI 500kHz) in real time or as demodulated amplitude and phase. The reference for the demodulation is the periodic modulation signal applied to the EOM, see Eq.(4.2), which is provided by the signal generator of the MFLI itself. The implementation of the signal division and lock-in detection vary for different setups. In a first version, the signals diff and sum are divided using an analogue voltage divider and then demodulated directly by the MFLI. In a second version, diff and sum are recorded as raw signals by the MFLI and then divided and demodulated computationally to improve accuracy.

Measurement of the induced particle dynamics and a simultaneous size measurement using BLS (see Chapter 3) are sufficient to determine the mass  $m$  of the particle. As discussed in Section 4.2, and shown in Fig.(4.2) in particular, the phase measured as function of modulation frequency,  $\varphi(f)$ , is better suited for retrieval of  $\Omega_0$  and  $\Gamma_0$  of the harmonic oscillation than the amplitude,  $A(f)$ . In addition, the determination of  $\Omega_0$  and  $\Gamma_0$  via  $\varphi(f)$  does not require calibration of the PSP, as it is independent of the absolute length scale of the position measurement. The measured phase does however include the signal delay due to the impedance of the PSP and the read-out electronics,  $\varphi_{\text{meas}} = \varphi + \varphi_{\text{imp}}$ , which has to be corrected for the analysis. To this end,  $\varphi_{\text{imp}}$  is measured by putting the PSP in the path of one of the trapping beams with the respective beam focused off-center on the photosensitive area. The phase of the oscillation in the diff chan-

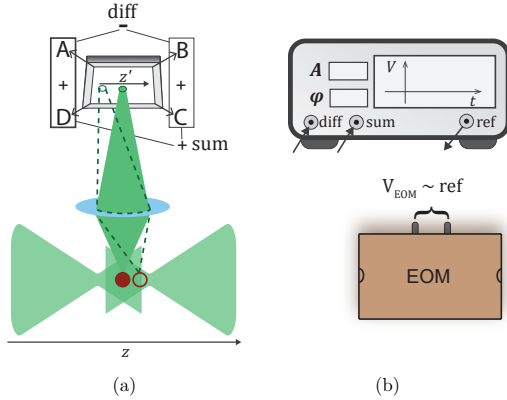


Figure 4.4: Particle position tracking setup. (a) Position sensing using a lateral effect sensor. The full and hollow brown circle indicate two instances of the particle oscillation along the trapping beam axis  $z$  during a modulation cycle. The image travels along  $z'$  on the sensor active area accordingly. From the photoinduced current at electrodes  $A$ ,  $B$ ,  $C$ ,  $D$ , the position of the particle image is obtained as  $z' = \frac{\text{diff}}{\text{sum}}$ , where  $\text{diff} = (A + D) - (B + C)$  and  $\text{sum} = A + B + C + D$ . (b) Signal demodulation for retrieval of oscillation amplitude  $A$  and phase  $\varphi$ . See main text for details.

nel is then measured in this configuration. As the EOM operates on much faster timescales than the maximum modulation frequency and the time for light propagation can be neglected, the measured phase is purely due to the impedance that is to be determined. This phase is characterized over the maximum frequency range of the experiments, 1–5000 Hz, and subtracted from the measurements in order to obtain the true phase of the particle oscillation,  $\varphi(f) = \varphi_{\text{meas}}(f) - \varphi_{\text{imp}}(f)$ . Fig.(4.5) shows the numerical result of the impedance characterization, which predominantly depends on the PSP and is therefore virtually identical for all measurements setups used in this thesis. With  $\Gamma_0$  obtained from fitting of  $\varphi(f)$  using Eq.(4.26) and the radius  $R$  of the particle determined by BLS, the mass of the particle is found using the definition of  $\Gamma_0 = \frac{1}{2\pi} \frac{\gamma}{m}$ :

$$m = \frac{1}{2\pi} \frac{\gamma}{\Gamma_0} = \frac{3\mu R}{(1 + C_0 \frac{\lambda_{\text{free}}}{R}) \Gamma_0} \quad (4.28)$$

where we have used Eq.(4.6) for  $\gamma$  and Eq.(4.27) for the slip correction,

respectively.

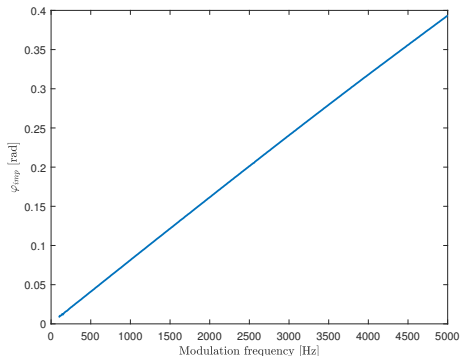


Figure 4.5: Phase delay due to impedance in the measurement setup. The slope of the data is almost linear, with a best fit value of  $(82.5 - 5.1 \cdot 10^{-4} \cdot f) \mu\text{s}$ .

## 4.5 Example data set

The following example illustrates the principle of the single particle mass measurement and demonstrates the feasibility and accuracy of the method. For this example, a single liquid droplet of pure squalane ( $\text{C}_{30}\text{H}_{62}$ ) is optically trapped and characterized using the techniques explained in this chapter and in Chapter 3.

Fig.(4.6) shows the oscillation amplitude and impedance corrected phase measured during a sweep of the modulation frequency. The measurement is repeated for different modulation amplitudes  $Z_0$ . The comparison reveals no discernible difference between phase curves for different modulation amplitudes in agreement with the model, which predicts that  $\varphi$  is independent of  $Z_0$  (see Eq.(4.17) or Eq.(4.26)). This feature is specific to the harmonic potential, therefore, this observation indicates that anharmonic contributions to the trapping potential can be neglected as is assumed in the model.

The size of the squalane droplet is determined using broad-band light scattering (BLS). Fig.(4.7) shows the BLS spectrum at the time of the phase



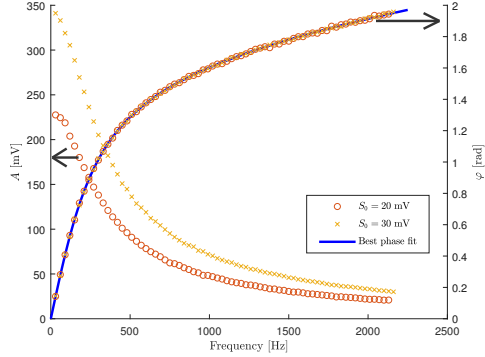


Figure 4.6: Oscillation amplitude  $A$  and phase  $\varphi$  as function of frequency of a squalane droplet. For  $A$  the value is given as the signal amplitude in units of volts. The frequency is swept from 30–3000 Hz and the measurement is repeated for different modulation amplitudes indicated by  $S_0$ . Only datapoints for which the  $A > S_0$  are shown. The best fit of the phase curve using Eq.(4.26) is shown as a solid line.

measurements and the best fit from Mie theory. As explained in Chapter 3, the best fit is determined by optimizing the radius  $R$  and the constant and dispersive part of the refractive index,  $n_0$  and  $n_1$ , respectively, until best agreement between measurement and spectrum is observed by eye. Similarly, the uncertainty is found as the range of  $R$ ,  $n_0$  and  $n_1$  for which satisfactory agreement can be observed. Table (4.1) lists the corresponding fit values obtained from BLS.

Using the data presented in Fig.(4.6) and the particle size obtained from BLS, values for  $\Omega_0$  and  $\Gamma_0$  are obtained from fitting with Eq.(4.26). The best fit values and uncertainties are shown in Table (4.1). The best fit is determined as the least squares fit between experimental data and model function. For determination of the fit uncertainties of  $\Omega_0$  and  $\Gamma_0$  a few considerations are necessary: Many text book algorithms exist for the calculation of the fit uncertainties, however, they typically rely on certain assumptions regarding the measurement data, in particular that there be no correlation between the individual measurement errors. This assumptions breaks down in our case for two reasons: First, if the signal amplitude from the particle oscillation is small, artifacts arising from systematic uncertainties in the position mea-

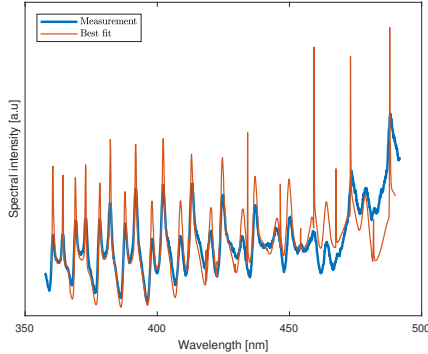


Figure 4.7: Experimental broad-band light scattering (BLS) spectrum and simulation using Mie theory. The simulated spectrum corresponds to the best fit as determined by visual inspection. Best fit parameters are  $R = 1.792 \mu\text{m}$ ,  $n_0 = 1.455$  (at 475 nm) and  $n_1 = 0.020$ .

surement by the PSP become relevant, which introduce a bias in the phase measurement. These artifacts depend on the variation of the total light intensity on the PSP during a modulation cycle, and are therefore more significant for larger modulation signal amplitudes  $S_0$ . Second, optically trapped liquid droplets exhibit drifts and sudden jumps of the trapping position along the trapping beam axis. This affects the phase measurement as the overall optical force on the particle changes for varying trapping positions. Although the original trapping position is typically restored after a few seconds, the variation in trapping position introduces correlation between subsequent phase measurements during a frequency sweep.

For the aforementioned reasons, the uncertainty of the fit parameters  $\Omega_0$  and  $\Gamma_0$  are determined according to the following procedure: Only data points, for which the oscillation signal amplitude exceeds a certain threshold, 20 mV, are considered for the fit. In addition, the oscillation signal amplitude must exceed the modulation signal amplitude,  $S_0$ . Both the absolute threshold and the threshold given by  $S_0$  are empirical values. The best fit is then determined by the minimum sum of squared errors. Using this, we define the uncertainty range of  $\Omega_0$  and  $\Gamma_0$  as the range for which the sum of squared errors is smaller than twice the least squared error. This range is equivalent to the range of fit parameters that is compatible with the observed data, taking

Quantity	Best fit	uncertainty
$R$	1.792 $\mu\text{m}$	0.017 $\mu\text{m}$
$n_0$ (475 nm)	1.455	0.015
$n_1$	0.020	0.001
$\Omega_0$ (20 mV)	985.5 Hz	10.2 Hz
$\Omega_0$ (30 mV)	985.0 Hz	7.9 Hz
$\Gamma_0$ (20 mV)	4565.9 Hz	99.2 Hz
$\Gamma_0$ (30 mV)	4539.8 Hz	73.1 Hz
$m$ (20 mV)	$19.90 \cdot 10^{-15}$ kg	$0.62 \cdot 10^{-15}$ kg
$m$ (30 mV)	$20.00 \cdot 10^{-15}$ kg	$0.51 \cdot 10^{-15}$ kg
$\rho$ (20 mV)	$819.0$ kg m $^{-3}$	$33.3$ kg m $^{-1}$
$\rho$ (30 mV)	$825.0$ kg m $^{-3}$	$28.9$ kg m $^{-3}$

Table 4.1: Best fit values and uncertainties for the example data set. The voltages in parentheses indicate  $S_0$ .

into account the shifting trapping position. This holds true even in the case of maximum (anti-)correlation between individual phase measurements, i.e., when the particle shifts between two discrete trapping positions between every individual phase measurement.

Finally, mass  $m$  and density  $\rho$  are determined using Eq.(4.28) and  $\rho = m \cdot (\frac{4}{3}\pi R^3)^{-1}$ , respectively. The obtained values for  $m$  and  $\rho$  are listed in Table (4.1) where the uncertainties represent the propagated uncertainties of  $R$  and  $\Gamma_0$ . The measured densities agree very well with the density of squalane at room temperature<sup>75</sup>,  $\rho = 808 \pm 1$  kg m $^{-3}$ , demonstrating the accuracy of the measurement. The relative errors for both mass and density are of the order of a few percent, which is comparable to the relative accuracy of measurements with EDB.

A systematic investigation of different squalane droplets in the size range 1.0–2.0  $\mu\text{m}$  has been performed, and the density measurements are summarized in Fig.(4.8). It is observed that data which has a high variance in the corresponding phase measurement tends to deviate from the expected value given by the bulk density. The variance is obtained by the least mean squared error of the phase fitting. An empirical threshold value of  $(0.006 \text{ rad})^2 = (0.34^\circ)^2$  is used to group the data into categories according to the noise level of the phase measurement: Phase measurements that exceed this value by more than a factor of 2 represent noisy data, or equivalently, data where the particle position has been shifting significantly during the measurement. As illustrated in

Fig.(4.8), this subset has a low confidence level on the resulting density values and is therefore deemed unreliable. Data sets with a variance comparable or smaller than the threshold generally agree very well with the expected bulk value, depending on the exact value of the variance. We find for measurements below the threshold value an average density of  $832 \pm 35 \text{ kg m}^{-3}$ , where the uncertainty is the standard deviation. The average uncertainty for these measurements is  $42 \text{ kg m}^{-3}$ . For measurements with variance between 1 and 2 times the threshold, the corresponding values are  $862 \pm 52 \text{ kg m}^{-3}$  for the average density and  $67 \text{ kg m}^{-3}$  for the mean uncertainty. Stable trapping conditions are therefore crucial for the mass measurement. The variance of the phase measurement provides an independent a posteriori criterion to distinguish reliable from unreliable data.

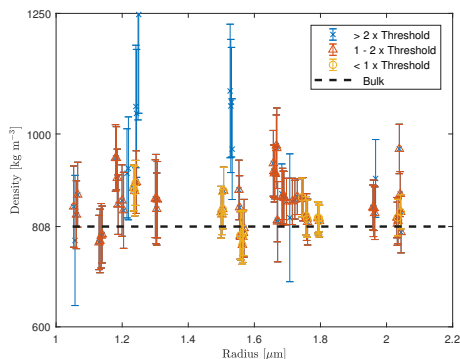


Figure 4.8: Density measurements of squalane droplets of different sizes. The data is grouped into categories according to the variance in the corresponding phase measurement with respect to the best fit. Blue crosses indicate noisy data, red triangles slightly noisy data and yellow circles low noise data. The threshold value for the noise is defined as  $(0.006 \text{ rad})^2$ . The expected density is indicated by the black dashed line and corresponds to the bulk density of squalane. The correlation between noise level and the agreement between measurement and expectation is apparent. In particular, the noisier data appears to be biased towards larger densities.

## 5 Weighing picogram aerosol droplets with an optical balance

This chapter is a copy of a journal publication:

<b>Title</b>	Weighing picogram aerosol droplets with an optical balance
<b>Authors<sup>a</sup></b>	Oliver Reich, Grégory David, Kivanç Esat and Ruth Signorell
<b>Original article</b>	Comm. Phys. <b>3</b> , 223 (2020)
<b>License</b>	Creative Commons Attributions v4.0 International (CC-BY) <a href="http://creativecommons.org/licenses/by/4.0/">http://creativecommons.org/licenses/by/4.0/</a>

<sup>a</sup> Department of Chemistry and Applied Biosciences, ETH Zurich, Vladimir-Prelog-Weg 2, CH-8093, Zurich, Switzerland

The style of the text and the style, size and placement of the figures and tables have been adapted, as have the numbering of figures, tables and sections. The supplementary material is attached as Section 5.8. The author contributions are specified in Section 5.6.

## Abstract

Optical traps are used to isolate and manipulate small objects in air and liquids, enabling the thorough characterization of their properties in situ. However, no broadly applicable technique for mass measurements of optically trapped objects is currently available. Here we propose an optical balance for mass measurements of optically trapped aerosol particles. By analyzing light-induced harmonic oscillations of a particle, its mass is determined nondestructively and with high accuracy on a time scale of seconds. Its performance is demonstrated for aqueous salt droplets, where masses as low as 4 pg ( $4 \cdot 10^{-15}$  kg) have been measured with an accuracy of  $\sim 100$  fg. The balance is straightforward to implement and broadly applicable.

## 5.1 Introduction

Optical traps are widely used to isolate small objects in the liquid phase, in the gas phase and in vacuum. The importance such traps have gained has been recognized by the 2018 Nobel prize in Physics awarded to Arthur Ashkin for the invention of optical tweezers and their applications<sup>4</sup>. Optical traps serve to manipulate small objects in different environments (liquid, gas, vacuum), and for ultrasensitive measurements of forces and torques<sup>22,76–85</sup>. With many applications in the liquid phase related to biological systems<sup>17,86</sup>, such as proteins or living cells, they play a key role in developing and shaping the fields of biophysics and biology<sup>17,78,86</sup>. Optical trapping has also been realized in low-pressure environments, e.g., for the quantification of the Brownian motion<sup>87</sup> or to study fast particle rotations<sup>76,88</sup> and the momentum transfer from light to trapped particles<sup>89</sup>. In the gas phase, optical traps enable the characterization and manipulation of single isolated aerosol particles and droplets in the submicrometer-size and micrometer-size range with attoliter to picoliter volumes<sup>42,78,90,91</sup>. Studies typically focus on properties such as size, shape, refractive index, chemical composition, viscosity, and surface tension<sup>25–28,33</sup> with the goal to improve our understanding of aerosol processes, such as phase transitions<sup>92</sup>, diffusion<sup>28</sup>, evaporation<sup>91,93,94</sup>, coagulation<sup>95</sup>, photochemistry<sup>32</sup>, reactions with gases or radicals<sup>24,29,91</sup>, and hygroscopic growth<sup>91,93</sup>.

Despite the fact that the mass is a key quantity, a broadly applicable method for the determination of the mass of optically trapped aerosol droplets and particles has so far not been demonstrated. Currently, the electrodynamic balance (EDB)<sup>43,45,96–98</sup> is the reference technique to determine the mass of single particles isolated in air. EDBs provide non-destructive, high-accuracy (in the percent range) mass measurements of particles, but they require prior charging of the particles and mass calibration. They usually provide mass measurements for larger particles with radii ranging from a few to many micrometers, not accessing the submicron range. Submicron-sized droplets and particles are particularly relevant in many atmospheric processes, such as scattering and absorption of sunlight<sup>99,100</sup> or size-dependent enhanced kinetics<sup>26,101,102</sup>. Mass measurements of aerosol particles in optical traps are limited to the special case of photophoretic traps<sup>40,41</sup>. They require the particle to absorb the light of the trapping laser, which heats the particle. In addition to the size limitation to particles of at least a few<sup>41</sup> to a few ten<sup>40</sup> micrometers in radius, the heating substantially restricts the applicability of these traps to absorbing, non-volatile particles, basically excluding all

volatile and semi-volatile particles, in particular also aqueous droplets. With a typical accuracy of 15%<sup>40,41</sup>, they do currently not reach the accuracy of EDBs.

This study reports an optical balance for the non-destructive mass determination of optically trapped aerosol droplets and particles with sizes down into the submicron range (lower picogram range). Using modulated counter-propagating optical tweezers, the mass of an aqueous NaCl droplet is determined by inducing harmonic oscillations and analyzing the resulting dynamics. The mass is obtained with high accuracy (less than 2%) at different relative humidities (RH), and the hygroscopic mass growth of the droplet is quantified. The optical balance is straightforward to implement, does not require particle charging, and can even be used without prior mass calibration, which makes it broadly applicable for many studies in aerosol science, or other scientific fields which use optical trapping.

## 5.2 Results

### 5.2.1 Principle of mass measurement

Dual beam traps are widely used to trap particles<sup>35,87,103–107</sup>. Fig.(5.1a) shows a sketch of the counter-propagating optical tweezers<sup>31,32</sup> (CPT) used for trapping single aqueous NaCl droplets at ambient pressure (see “Methods” section for droplet generation and control of the relative humidity). Light from a continuous 532 nm laser (Opus 532, Laser Quantum, typical power  $\approx 1$  W) passes through a Faraday isolator (Thorlabs, IO-5-532-HP) to avoid back reflections returning to the laser. A half-wave plate is used to orient the polarization of the laser horizontally before the electro-optic modulator (EOM, Conoptics, 350-50-01-RP), which is used to control the polarization of the laser beam. The laser beam is then expanded four times by a two-lens telescope (focal lengths of 50 and 200 mm). A polarization beam-splitter cube (PBC) splits the incident laser beam into two counter propagating beams. The beams are focused with two aspherical lenses (CVI, BFPL-25.4-50.0-UV, 56.6mm focal length at 532 nm) in the center of a trapping cell, where a single aerosol droplet is immobilized (brown dot). One half-wave plate is used in each trapping beam to align the polarization of the two beams parallel to each other. A path length difference of approximately 50 cm between the two trapping beams is used on purpose to avoid interference between the two



beams (the coherence length of the laser is 7 mm). The optical forces are controlled via the power ratio of the two counter-propagating beams with the EOM. By modulating the power ratio of the two beams sinusoidally in time, a harmonic oscillation of the particle is induced along the beam propagation direction (Fig.(5.1b)). The driven harmonic oscillation of the droplet is described by the following equation of motion (see “Methods” section):

$$\ddot{z} + 2\pi\Gamma_0\dot{z} + 4\pi^2f_0^2z = 4\pi^2f_0^2Z_0\sin(2\pi ft) \quad (5.1)$$

where  $z$  is the position of the droplet along the axis of the laser beams,  $f_0$  is the natural frequency of the oscillator and  $\Gamma_0$  is its damping rate. The modulation amplitude  $Z_0$  (amplitude corresponding to the position change of the minimum of the trapping potential) and the modulation frequency  $f$  of the oscillation are controlled by the modulated voltage applied to the EOM. Eq.(5.1) is solved by

$$z(t) = a\sin(2\pi ft - \varphi) \quad (5.2)$$

where  $a$  is the amplitude of the droplet’s oscillation and  $\varphi$  is its phase. The droplet position is measured by a position sensitive photodiode (PSP) connected to a lock-in amplifier. During the harmonic oscillation of the droplet, the lock-in amplifier directly measures  $a$  and  $\varphi$ . For the data analysis, we prefer  $\varphi$  over  $a$  because of correlation issues with the latter (see “Discussion” section). A sweep of the modulation frequency provides  $\varphi(f)$ , from which  $f_0$  and  $\Gamma_0$  are retrieved by fitting the experimental data to Eq.(5.3):

$$\tan(\varphi) = \frac{\Gamma_0 f}{f_0^2 - f^2} \quad (5.3)$$

The absolute mass  $m$  of the droplet is then determined from Eq.(5.4):

$$m = \frac{3R\mu}{C_c\Gamma_0} \quad (5.4)$$

where  $R$  is the particle radius,  $\mu$  is the dynamic viscosity of the surrounding fluid (nitrogen in our case) and  $C_c$  is Cunningham’s correction factor<sup>73</sup>. Eq.(5.4) shows that an additional measurement of  $R$  is sufficient to calculate the mass of the droplet from  $\Gamma_0$ . We use broad-band light scattering (BLS)<sup>31,32</sup> to determine  $R$  (Fig.(5.1b), “Methods” section and Section 5.8.1). With our optical balance,  $m$  can be retrieved without mass calibration, in contrast to mass measurements with EDBs which require calibration.

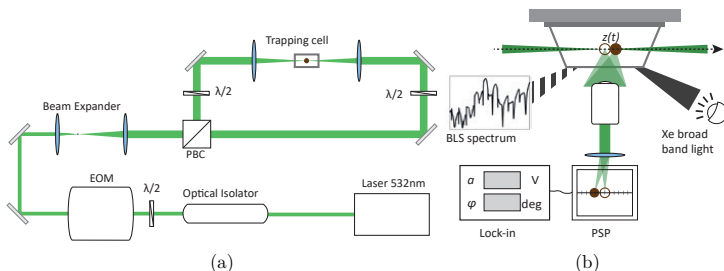


Figure 5.1: (a) Layout of the counter-propagating optical tweezers. A half-wave plate ( $\lambda/2$ ) is used to adjust the polarization at  $45^\circ$  to the crystal axes of the electro-optic modulator (EOM). The laser beam is split at the polarization beam splitter cube (PBC) according to the polarization of the light set by the EOM. The particle (brown dot) is trapped in the cell between the foci of the two trapping beams. (b) Determination of the droplet's shift in position  $z(t)$  along the axis of the trapping beams (dashed arrow) and of its radius  $R$ . A position sensitive photodiode (PSP) tracks  $z(t)$  by measurements of the light scattered by the droplet. When the droplet moves from the position of the brown empty circle to the full circle, the position of the collected scattered light on the PSP changes accordingly. During the modulation of the trap the amplitude  $a$  and phase  $\varphi$  of the particle oscillation are measured with a lock-in amplifier. The broad-band light scattering spectra (BLS) are obtained by illuminating the particle with a broad-band Xe lamp (filled triangular beam), and recording the light elastically scattered by the droplet as a function of the wavelength (hatched black triangular beam).

## 5.2.2 Harmonicity of the droplet oscillation

The harmonicity of the trapping potential and the induced particle oscillation is verified by the results presented in Fig.(5.2). Fig.(5.2a) shows an example measurement of  $\varphi$  as a function of  $f$  for a trapped aqueous NaCl droplet at an RH of 68 % for four different EOM modulation voltages between 10 mV to 40 mV. The latter correspond to values for the amplitudes  $Z_0$  between  $\sim 10 \mu\text{m}$  to  $40 \mu\text{m}$ . The measured  $\varphi(f)$  are essentially identical for the four different modulation voltages. Fig.(5.2b) illustrates that the values for  $\Gamma_0$  (right ordinate) and  $f_0$  (left ordinate) retrieved from the data in panel (a) using Eq.(5.3) agree within their uncertainty for the four different modulation voltages. These uncertainties lie below 0.5 % for the measurements with the 20, 30, and 40 mV modulation voltage. For the measurement at 10 mV modulation voltage, the uncertainties of  $\Gamma_0$  and  $f_0$  are slightly larger

(2% and 1%, respectively). This is due to the smaller  $Z_0$  resulting in a lower signal-to-noise ratio for  $\varphi(f)$ . From Fig.(5.2) it is clear that  $\varphi(f)$ ,  $\Gamma_0$  and  $f_0$  are virtually independent of  $Z_0$  (i.e. the modulation voltage), which demonstrates that the harmonic approximation provides a very good description of the trapping potential and the induced particle oscillation. In the rare case when the droplet size and the wavelength of the trapping laser precisely match a resonance condition, so that a Mie resonance (also called morphology dependent resonance or whispering gallery mode) is excited in the droplet<sup>50</sup>, its dynamics does no longer follow a harmonic oscillation (see Section 5.8.2 and Fig.(5.7)). Fortunately, Mie resonances are limited to very specific combinations of particle size and wavelength so that they do not pose any practical limitation to the mass measurement. If a resonance is encountered, a minute (subpercent) change of the relative humidity is enough to restore the harmonic oscillation of the particle.

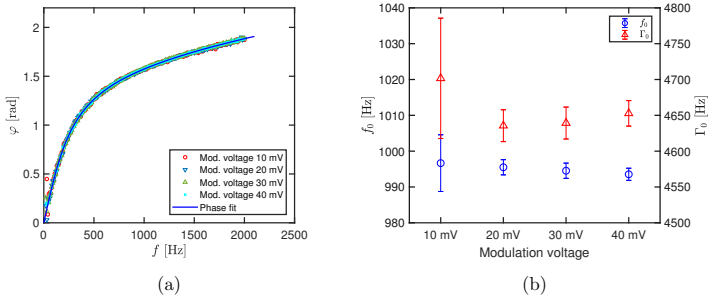


Figure 5.2: Phase ( $\varphi$ ) measurements and retrieved  $f_0$  and  $\Gamma_0$  for different modulation voltages. (a)  $\varphi$  as a function of the frequency  $f$  for a trapped aqueous NaCl droplet at a relative humidity of 68% for four different electro-optic modulator voltages of 10, 20, 30, and 40 mV (see symbols in the legend). The data points for the different voltages virtually coincide with each other. The same holds for the fits. For clarity, we only show one of the fitted  $\varphi(f)$  curves (solid blue trace). (b) Natural frequency  $f_0$  (blue circles) and damping rate  $\Gamma_0$  (red triangles) as a function of the modulation voltage, retrieved from fits to the phase measurements in panel (a). The error bars indicate the 68% confidence interval of the fits.

### 5.2.3 Mass measurement and related quantities

Fig.(5.3a) shows the mass  $m$  (red triangles) retrieved for aqueous NaCl droplets with the same NaCl content, but varying water content given by the RH. The chosen range of RH covers both supersaturated and undersaturated concentrations (the critical RH of NaCl is  $75.3 \pm 0.3\%$ <sup>108</sup>).  $m$  is retrieved from  $\Gamma_0$  and  $R$  using Eq.(5.4). The accuracy of  $m$  is limited by systematic errors and random errors. The systematic error mainly arises from uncertainties of the spot size of the scattered light on the PSP, and is estimated to lie below 3.5% of the droplet mass (see “Methods” section, Section 5.8.3 and Fig.(5.8)). We further estimate the random error to be less than 2-3% of the droplet mass. With a maximum systematic error of 3.5% and a maximum random error of 2-3%, we specify a maximum total error of 5.5-6.5%. For the specific data in Fig.(5.3a) — which cover droplet sizes in the micron range — we determined a systematic error of 2% (see below) and random errors between 0.5 and 1.9% (Table (5.1)). The maximum random error for submicron droplets ( $R \sim 800$  nm,  $m$  of few picograms; not listed in Table (5.1)) is somewhat larger around 3%. A maximum total error of 5.5-6.5% represents a high accuracy, in particular when one considers that this is achieved for very low absolute droplet masses in the lower picogram range without any mass calibration. Access to the lower picogram mass range combined with this level of accuracy already provides satisfactory results for many applications. Mass calibration with a suitable reference allows us to correct for the systematic error and thus to improve the accuracy even further to the level of the random error of less than 2-3%. The calibration can be performed by comparing the measured density of the aqueous NaCl droplets (from  $R$  and  $m$ ) to the density of corresponding bulk solutions<sup>109</sup> (Fig.(5.3b)). We determine a constant calibration factor  $C = 0.98$  for the density ( $\rho_c = C \cdot \rho$ ), and use the same factor for mass calibration ( $m_c = C \cdot m$ ).  $m_c$  and  $\rho_c$  denote the mass and the density, respectively, after calibration (Fig.(5.3a) and Fig.(5.3b) and Table (5.1)). A constant mass calibration factor of 0.98 indicates a systematic bias of 2%, and corrects the systematic error mentioned above. (See the “Discussion” section for a further discussion of Fig.(5.3b)).

In addition to the droplet mass and density, our optical balance also allows us to retrieve hygroscopic mass and size growth factors. The mass growth factor is defined as  $m^*(RH) = m(RH)/m_{\text{NaCl}}$ , where  $m(RH)$  is the droplet mass at a given RH and  $m_{\text{NaCl}}$  is the NaCl mass in the solution droplet (see “Methods” section). Note that  $m^*(RH)$  does not depend on the calibration. Fig.(5.3c) compares  $m^*$  from this study with re-

sults from a previous investigation with an EDB<sup>45</sup>. Almost perfect agreement is observed between the two different studies, which demonstrates that mass measurements with the optical balance can easily compete with mass measurements in EDBs. The droplet size growth factor is defined as  $R^*(\text{RH}) = R(\text{RH})/R_{\text{dry}}$ , where  $R(\text{RH})$  is the droplet radius at a given RH and  $R_{\text{dry}}$  is the radius of a completely dried particle (see Section 5.8.4 for calculation of  $R^*$ ). The  $R^*$  values retrieved for the data in Table (5.1) lie between 1.75 and 2.19 (see Section 5.8.4 and Fig.(5.9)). To allow comparison with previous measurements performed with hygroscopic tandem differential mobility analyzers (HTDMA) at 90% RH, we extrapolate  $R^*$  to 90% RH (see Section 5.8.4). The retrieved  $R^*(90\%) = 2.40 \pm 0.02$  agrees within uncertainties with theoretical predictions<sup>110</sup> and the HTDMA measurements ( $R^*(90\%) = 2.27 - 2.46$ )<sup>49</sup>.

RH [%]	$R$ [ $\mu\text{m}$ ]	$m$ [ $10^{-15}$ kg]	$m_c$ [ $10^{-15}$ kg]	$\rho_c$ [ $\text{kg m}^{-3}$ ]	$m^*$
67.5	$1.385 \pm 0.013$	$14.70 \pm 0.59$	$14.39 \pm 0.11$	$1294 \pm 15$	$3.19 \pm 0.02$
77.6	$1.537 \pm 0.018$	$18.70 \pm 0.79$	$18.33 \pm 0.19$	$1204 \pm 18$	$4.06 \pm 0.04$
80.7	$1.600 \pm 0.008$	$20.30 \pm 0.76$	$19.90 \pm 0.10$	$1161 \pm 8$	$4.41 \pm 0.02$
86.1	$1.733 \pm 0.010$	$25.10 \pm 0.95$	$24.62 \pm 0.13$	$1129 \pm 9$	$5.45 \pm 0.03$

Table 5.1: Radius ( $R$ ), mass before ( $m$ ) and after calibration ( $m_c$ ), density after calibration ( $\rho_c$ ), and mass growth factor ( $m^*$ ) for micron-sized NaCl droplets at different relative humidities (RH). The uncertainties quoted for  $R$  and  $m$  account for both systematic and random errors. Those for  $m_c$ ,  $\rho_c$ , and  $m^*$  only include random errors.  $m_c$  and  $\rho_c$  are obtained with a calibration constant  $C = 0.98$ .

## 5.3 Discussion

### 5.3.1 Range and accuracy of mass measurements

The optical balance permits mass measurements of aerosol particles in the picogram range, down to at least  $4 \cdot 10^{-15}$  kg. The accuracy lies at 5.5–6.5% without and at 2–3% with mass calibration. The latter corresponds to a sensitivity of  $\sim 1 \cdot 10^{-16}$  kg (100 fg) for the smallest droplet reported here. The optical balance extends particle mass measurements into the submicrometer size range, i.e., to masses that are a few orders of magnitudes lower

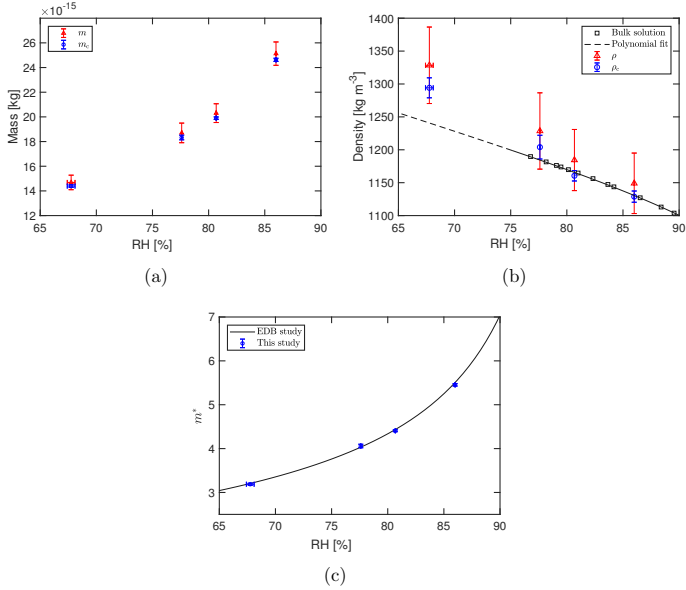


Figure 5.3: Mass, density, and mass growth factor of aqueous NaCl droplets. (a) Droplet mass before ( $m$ , red triangles) and after calibration ( $m_c$ , blue circles) as a function of relative humidity (RH). (b) Droplet densities before ( $\rho$ , red triangles) and after calibration ( $\rho_c$  blue circles) as a function of RH. The density of the bulk solution is indicated by black squares<sup>109,111</sup>. The black line represents bulk densities with an extrapolation into the supersaturation region (dashed line)<sup>45</sup>. The discrepancy between the extrapolation and our measurement is addressed in the “Discussion” Section. (c) Mass growth factors  $m^*$  from this study (blue circles) and from an earlier study with an electrodynamic balance (EDB) (black line)<sup>45</sup> as a function of RH. Horizontal error bars indicate the RH variation during the measurements. Vertical error bars for the uncalibrated  $m$  and  $\rho$  are the sum of the systematic error and the random error, while the error bar for the calibrated  $m_c$  and  $\rho_c$  and for  $m^*$  indicate the random error only.

than typical measurements in EDBs<sup>45,96</sup> and photophoretic traps<sup>40,41</sup>, and hence substantially broadens the range of applications (see below). It is not only the extended mass range that makes it more versatile compared with photophoretic traps and EDBs, but also the fact that the balance is neither limited to charged particles (as EDBs are) nor to non-volatile, light-absorbing solid particles (as photophoretic traps are). The very high mass accuracy of the optical balance could only be achieved because we use the phase ( $\varphi$ ) and not the amplitude ( $a$ ) in the analysis of the droplet dynamics. The example in Fig.(5.4) illustrates that in certain ranges the mass cannot be determined unambiguously from  $a(f)$  because  $\Gamma_0$  and  $f_0$  are strongly correlated. As a consequence,  $a(f)$  can become indistinguishable for different combinations of  $\Gamma_0$  and  $f_0$  (blue full and dashed line); i.e., for different masses (in Fig.(5.4) for two masses that differ by a factor of 2.25). This issue does not arise for  $\varphi(f)$  because  $f_0$  is the frequency  $f$  at which  $\varphi(f_0) = \frac{\pi}{2}$  (crosses in Fig.(5.4)). Hence, a unique solution is obtained for the particle mass when the phase is used instead of the amplitude. The issue with  $a(f)$  especially arises when the particle motion is overdamped. i.e., for smaller aerosol particles and for particles suspended in liquids.

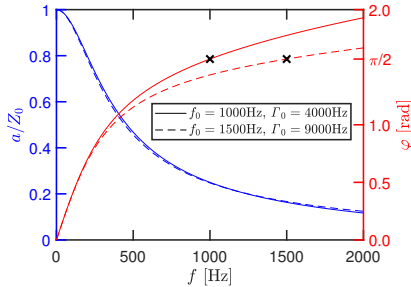


Figure 5.4: Simulated phase and amplitude measurement.  $\varphi$  (red lines) and  $a$  (blue lines), normalized by the modulation amplitude  $Z_0$  as a function of the frequency  $f$  for two different parameter sets  $f_0$  and  $\Gamma_0$  (dashed lines and full lines), where  $f_0$  is the natural frequency of the particle and  $\Gamma_0$  is its damping rate. The black crosses mark the points where  $\varphi(f = f_0) = \frac{\pi}{2}$ . A unique solution for the mass can only be obtained from  $\varphi(f)$ , but not from  $a(f)$ .

### 5.3.2 Applications

The optical balance allows one to access properties of supersaturated solutions, which in general cannot be retrieved from bulk measurements because of precipitation. Among those properties is the density of supersaturated solutions. Comparison with bulk densities is only possible in the undersaturated regime, i.e. for aqueous NaCl solutions above the critical RH of 75.3% (Fig.(5.3b)). Tang et al.<sup>45</sup> suggests a polynomial extrapolation for the bulk density down to RHs of  $\sim 50\%$ . The corresponding extrapolation (black line in Fig.(5.3b)), however, reveals that a  $\sim 4\%$  lower density is obtained at an RH = 68% using this bulk extrapolation compared with our experimental value – a difference that lies outside the experimental uncertainty of  $\sim 1.2\%$  (Table (5.1)). The origin of this discrepancy between droplet experiment and bulk extrapolation is not obvious and offers an intriguing subject for further studies.

The knowledge of hygroscopic properties of atmospheric droplets is crucial for determining their radiative forcing<sup>48</sup>. To fully capture their effects, a comprehensive quantification of RH dependent droplet properties (e.g. size, mass, and density) is required. An interesting phenomenon is the so far unexplained size-dependence of  $R^*$  for NaCl and sea salts droplets that was previously reported in droplet studies with HTDMAs<sup>49,112,113</sup>. Depending on the instrument, HTDMA studies are limited to droplets with corresponding dry salt radii in the range  $R_{\text{dry}} \sim 100\text{--}175\text{ nm}$ <sup>114</sup>. EDBs, on the other hand, typically cover much larger particle sizes ( $R_{\text{dry}}$  of a few micrometers), so that the size range in-between remains unexplored.  $R^*$  studies with our optical balance will allow us to fill this gap (this study  $R_{\text{dry}} \sim 500\text{ nm}$  and larger), and to address potential size-dependent effects of  $R^*$  in this intermediate size range. Similarly, the optical balance also opens up studies of  $m^*$  in this intermediate size range. To the best of our knowledge,  $m^*$  has only been reported for supermicrometer-sized particles using EDBs. These are only few examples of the broad applicability of our optical balance. Aerosol science is expected to be a major area of use of this method. However, we also anticipate the optical balance to be of broad interest for mass measurements of small objects in the liquid phase, such as cells and other biological samples. Many studies exist that determine the mass of objects in liquids<sup>115–118</sup> and many studies apply optical trapping in the liquid phase<sup>77,84,85,119</sup>, but a combination of both methods has not yet been demonstrated. The optical balance we propose solves the issue of mass determination under overdamped conditions (Fig.(5.4)), so that it might offer a possibility to combine optical



trapping applications with mass determination in the liquid phase.

Our optical balance permits mass measurements of aerosol particles with masses in the picogram range, and probably beyond, with a high accuracy of 2–3%, covering a particle size range from micrometers down to submicrometers. The implementation of the balance combines the advantage of a straightforward experimental setup with the applicability to a wide variety of particles (liquid, solid, volatile, non-volatile, charged, uncharged). Its demonstrated performance extends mass measurements of aerosol particles into regions previously inaccessible. Aerosol studies related to atmospheric and technical processes, including pharmaceutical and medical applications, will profit from this extended capability. Beyond aerosol studies, the proposed optical balance holds promise for applications in the liquid phase, enabling the combination of optical trapping and mass measurements with intriguing possibilities, e.g., for the investigation of optically trapped cells and other biological objects.

## 5.4 Methods

### 5.4.1 Droplet generation and relative humidity control

The particles were generated from 0.5 M aqueous NaCl solutions using a commercial atomizer (TSI 3076) with pressurized humidified nitrogen (purity 5.0). The use of humidified nitrogen ensures the delivery of liquid droplets to the trapping cell. The concentration of the trapped aqueous NaCl solution droplets is determined by the RH in the trap (and not by the concentration of the initial solution) where the trapped droplets equilibrate quickly to the surrounding RH. The RH in the cell is varied between  $\sim 60\%$  and  $90\%$  by mixing dry and wet nitrogen with individually adjustable flow rates. The RH in the trapping cell is measured with a sensor (Sensirion, SHT31) placed a few millimeters away from the trapped droplets. The trapping cell is shown in Fig.(5.5). The cell is equipped with fused silica windows to transmit the light beams of the CPT, the BLS and the scattered light used for the position measurement. Additional apertures are used for the RH sensor and the gas flows through the cell.

### 5.4.2 Droplet dynamics

The time dependent position  $z(t)$  of the trapped droplet along the trapping axis is described by Newton's equation of motion,  $m\ddot{z} = F_{\text{drag}} + F_{\text{opt}}$ , where  $F_{\text{opt}}(z)$  is the optical force,  $F_{\text{drag}} = -\gamma\dot{z}$  is the drag force due to the surrounding fluid and  $\gamma$  is the drag coefficient. The droplet motion perpendicular to  $z$  is negligible in our experiments and is not considered here. Following the harmonic oscillator model, the optical potential  $V_{\text{opt}}(F_{\text{opt}}) = -\frac{\partial}{\partial z}V_{\text{opt}}$  is defined by a second order Taylor expansion  $V_{\text{opt}} = \frac{k}{2}(z - z_0(t))^2$ , where  $k$  is the trap stiffness and  $z_0(t)$  is the time dependent position of the minimum of the trapping potential during the modulation. For a sinusoidal modulation of the EOM voltage, the minimum of the trapping potential oscillates as  $z_0(t) = Z_0 \sin(2\pi ft)$ , where  $Z_0$  is the amplitude and  $f$  the frequency of the oscillation. Stokes' law is used to calculate  $\gamma(R) = 6\pi \frac{\mu R}{C_c(R)}$ , where  $R$  is the radius of the droplet,  $\mu$  is the dynamic viscosity of the surrounding fluid (nitrogen) and  $C_c(R)$  is the size dependent Cunningham correction factor. As explained in details in ref.<sup>74</sup>, the Cunningham correction factor accounts for the nonlinear decrease in the Stokes' drag force when the particle size approaches the molecular mean free path of the surrounding fluid. It is given by  $C_c(R) = 1 + 1.26 \frac{\lambda_N}{R}$ .  $\lambda_N$  is the mean free path in nitrogen ( $\lambda_N \approx \lambda_{\text{air}} = 68 \text{ nm}$  at  $20^\circ$ ). Using the quantities defined in this paragraph,  $f_0 = \frac{1}{2\pi} \sqrt{\frac{k}{m}}$  and  $\Gamma_0 = \frac{\gamma}{2\pi m}$  in Newton's equation yields Eq.(5.1). Substitution of  $\gamma$  in the expression for  $\Gamma_0$  yields Eq.(5.4).

### 5.4.3 Phase measurement and systematic error

$z(t)$  is measured with a commercially available PSP connected to a lock-in amplifier (Zurich Instruments, 500 kHz MFLI). The reference output of the lock-in amplifier is used to drive the EOM (ConOptics) and serves as the reference for the demodulation. During the frequency sweeps of the reference output ( $f \in [0, 2]\text{kHz}$ ), the raw phase is obtained directly from the demodulation of the signal of the droplet position along  $z$  by the lock-in amplifier. The signal is obtained by dividing the differential photodiode current by the total photodiode current. The measurement of the particle position is slightly delayed by the frequency-dependent impedance of the PSP and the readout electronics. This delay as a function of modulation frequency, which has to be subtracted from the raw phase to yield  $\varphi(f)$ , is determined separately by monitoring the modulation of one of the trapping beams in the frequency

range [0, 5]kHz. The phase of this signal is equal to the delay of the PSP and readout electronics because the response time of the EOM to the applied voltage and the light propagation are much faster than the modulation periods used in this study. The PSP and its collecting optics (Fig.(5.1b)) are mounted on a translation stage to adjust the focus of scattered light on the photosensitive area of the PSP. The focusing of the collected light on the PSP sensor affects the accuracy of the particle position tracking. It is mostly responsible for the systematic error of the mass measurement. We have quantified this effect on the accuracy of the mass measurement by repeating phase measurements for different focus sizes. This data is reported in the Supplementary Information (Section 5.8.3 and Fig.(5.8)). Generally, we estimate that the maximal error in the mass measurement caused by the light focus can be up to 3.5% of the absolute droplet mass. For the current measurements, it is 2%. The light focus is not changed between measurements at different RHs, so that the same systematic error applies to all mass measurements reported here.

#### 5.4.4 Random error

The random error of the mass measurement is calculated by propagating the random error of  $\Gamma_0$  and the error of  $R$  (see Section 5.8.1) using Eq.(5.4). The random error of  $\Gamma_0$  is determined from the measurements of  $\varphi(f)$  for voltage modulations of 20, 30, and 40 mV (Eq.(5.3)) as the average error of these three measurements. The measurements at 10 mV are not used for the analysis because of their lower signal-to-noise ratio. The error of  $R$  is found by fitting experimental BLS spectra (see below and Section 5.8.1).

#### 5.4.5 Broad-band light scattering (BLS)

The principle of the BLS measurements is described in David et al.<sup>32</sup>. The output of a fiber-coupled broad-band Xe lamp (Energetiq EQ-99XFC LDLS, spectral range 190–2100 nm) is collimated with a reflective collimator (Thorlabs, RC04FC-F01) and then focused on the particle with a reflective objective (Edmund Optics, 89–722). The elastically scattered light is collected over an angular range of 26.6° centered at a scattering angle of  $\theta \approx 37^\circ$  with another identical reflective objective. The collected scattered light is then focused on the fiber of the spectrometer (Andor, Kymera 328i with a Newton

A-DU940P-BV camera) with a reflective collimator (Thorlabs, RC04SMA-F01). Two shortpass filters (Edmund optics, 49 825, OD > 4) reduce the signal of the elastic scattering of the trapping laser. The wavelength range  $\lambda = 350\text{--}500\text{ nm}$  is used to retrieve the droplet radius  $R$  from fits of the experimental spectra to simulations using Mie theory.  $R$ ,  $\theta$ , and  $n_0$  and  $n_1$  of the wavelength-dependent refractive index of the droplet,  $n(\lambda)$ , are fit parameters. A first order Cauchy parametrization is used for  $n(\lambda)$ :

$$n(\lambda) = n_0 + n_1 \left( \left( \frac{\lambda_0}{\lambda} \right)^2 - 1 \right) \quad (5.5)$$

with a reference wavelength of  $\lambda_0 = 475\text{ nm}$ . Fig.(5.6) shows representative BLS spectra and the values of  $R$  and  $n_0$  determined in this study.

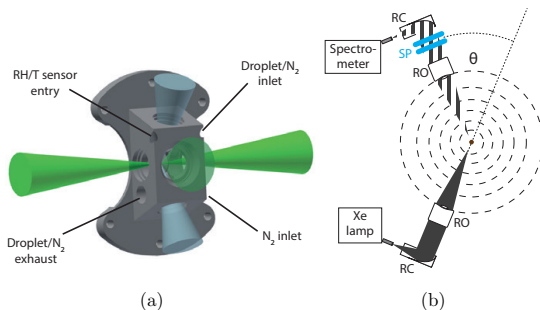


Figure 5.5: Drawing of the trapping cell and sketch of the BLS optics. The trapping cell is shown in (a). The counter-propagating tweezer beams propagate through the trapping cell as shown by the two green cones on the sides of the cell. The broadband light scattering (BLS) emission and collection are represented by the two blue cones. The scattering light used to measure the particle position is shown by the large green cone in front of the cell. Humidified nitrogen ( $N_2$ ) flow is used to control the relative humidity in the cell. The BLS optics is sketched in panel (b). The broadband light of a Xe lamp is shone on the particle by using reflective collimators (RC) and a reflective objective (RO). The dashed circles represent the elastically scattered light. The black dashed triangle indicates the fraction of the scattered light collected by the second RO around the scattering angle  $\theta$ , which is then coupled into the spectrometer using another RC. Two shortpass filters (SP) in the collection optics of the BLS attenuate the scattering of the trapping laser.

### 5.4.6 Mass growth factor $m^*$

In the present experiments, the mass change of a NaCl droplet caused by variation of the RH is purely due to the uptake or loss of water. Hence, the salt mass ( $m_{\text{NaCl}}$ ) in the droplet remains constant. As a cross-check, we determined  $m_{\text{NaCl}}$  of the trapped droplet at the different constant RHs using the water activity of bulk solutions with known mass fractions<sup>111</sup>. The retrieved values of  $m_{\text{NaCl}}$  at 78 %, 81 %, and 86 % RH ( $4.56 \pm 0.05$ ,  $4.50 \pm 0.02$  and  $4.49 \pm 0.02 \cdot 10^{-15}$  kg, respectively, for one given droplet) agree within 1.5 %. Below the critical RH (supersaturated solutions) bulk measurements are not possible so that  $m_{\text{NaCl}}$  cannot be determined in this way. We thus use the average values of  $m_{\text{NaCl}}$  determined at 78 %, 81 % and 86 % RH to calculate the mass growth factor  $m^* = \frac{m}{m_{\text{NaCl}}}$  of the droplet for undersaturated and supersaturated solutions (RH = 68 %).

## 5.5 Acknowledgements

This work was supported by the Swiss National Science Foundation (SNSF grant no. 200020\_172472) and ETH Zurich. We would like to thank David Stapfer and Markus Steger from the ETH mechanical and electronic shop for their help. We would like to acknowledge the contributions of Johannes Cremer in the early stage of this project.

## 5.6 Author contributions

R.S. conceived the project. R.S. and G.D. supervised the project. G.D., O.R., and K.E. implemented the experimental setup. O.R. performed the experiments and the analysis of the experimental data with assistance from G.D. O.R., G.D., and R.S. wrote the paper. All authors discussed the results and the manuscript.

## 5.7 Competing interests

The authors declare no competing interests.

## 5.8 Supplementary information

### 5.8.1 BLS spectra

The retrieval of  $R$ ,  $\theta$ ,  $n_0$  and  $n_1$  from the experimental spectra is described in the “Methods” part in the main manuscript (Eq.(5.5)). For all measurements, a constant central scattering angle of  $\theta = 37 \pm 2^\circ$  and a constant value of  $n_1 = 0.019 \pm 0.002$  were determined. The best fits are determined by visual inspection (Fig.(5.6a)). The errors of the fit parameters indicate the range of the fit parameters from which reasonable fits are obtained by visual inspection (Fig.(5.6b)).

### 5.8.2 Droplet dynamics at Mie resonances

Fig.(5.7a) visualizes the droplet dynamics in the vicinity of a Mie resonance (traces 1-3) and off-resonant (traces 6-9). The droplet dynamics is driven at a frequency of 1 Hz to ensure that the droplet can almost instantaneously follow the minimum of the trapping potential. Traces 1 to 9 are measured at very similar RHs (less than 1% change) and hence for very similar droplet sizes (less than 1.2% change). At resonance (trace 1), there is barely any droplet motion observable, despite the modulation of the trap. Hence, the droplet seems to be locked in a more or less fixed position. A step-like oscillatory motion is observed for conditions that are slightly off resonant (traces 2 and 3). For traces 4 and 5 - recorded under conditions that are even further away from the resonance - the step-like oscillatory motion is almost eliminated. The ideal sinusoidal oscillation is restored for curves 6 to 9. Such conditions are used to retrieve the droplet mass. Only a subpercent change in the RH is sufficient to restore the harmonic oscillation of the droplet. Fig.(5.7b) shows the intensity of the light scattered by the droplet and the RH as a function of the trace index. The scattered intensity gradually decreases for decreasing droplet size.

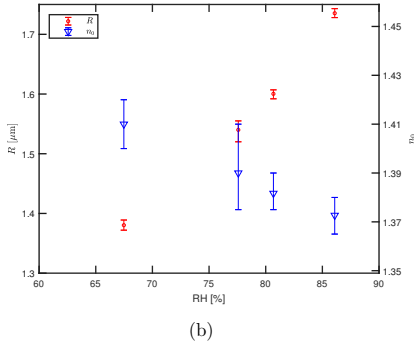
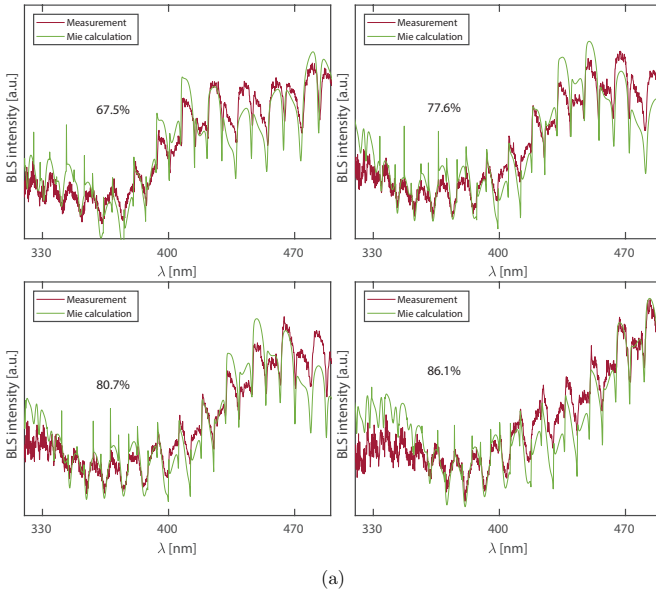


Figure 5.6: (a) Experimental BLS (broad band light scattering) spectra (brown traces) and best fits (light green traces) for the measurements at RHs (relative humidities) of 67.5 %, 77.6 %, 80.7 % and 86.1 %. (b) Optimal values of  $R$  and  $n_0$  for the different measurements at RHs of 67.5 %, 77.6 %, 80.7 % and 86.1 %. Error bars indicate the estimated uncertainty of the fits of the BLS spectra.



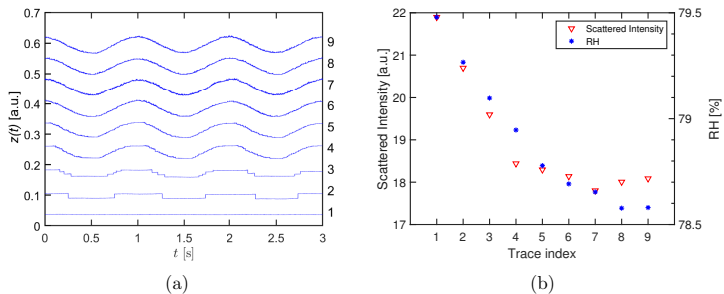


Figure 5.7: Droplet dynamics at a Mie resonance. (a) Droplet position  $z$  as a function of time  $t$  during the trap modulation for nine slightly different droplet sizes (trace index 1-9). A decreasing trace index indicates an increasing proximity to the resonance. The traces are offset in  $y$ -direction for better visibility. (b) Intensity of the scattered light (left axis) and RH (right axis) as a function of the trace index 1 to 9. The initial droplet radius lies at  $\sim 980$  nm.

### 5.8.3 Influence of the light focus on the phase measurement

The measured phase of the oscillation depends on the spot size of the collected light on the photosensitive area of the PSP (“Methods”, main manuscript). The signal measured by the PSP is the centroid position of the light pattern on its sensitive area. This centroid must correspond to the center of the light pattern to correspond to the real droplet position. When the collected scattered light is nicely focused onto the PSP photosensitive area, the oscillation of the centroid during the modulation corresponds to the droplet motion. The particle motion is hence properly measured and the mass of the particle can be calculated accurately. However, when the light is defocused from the photosensitive area of the PSP, the centroid position is affected by the change of the light scattering pattern during modulation. The pattern changes primarily due to the relative power of the trapping beams. Therefore, the PSP signal changes artificially in phase with the modulation of the trapping beams. The effect of this artifact on the measured phase,  $\varphi$ , is illustrated in Fig.(5.8a). It shows the phase difference,  $\Delta\varphi$ , between an underfocused and a focused beam (red, upside down triangles) and between an overfocused and a focused beam (blue triangles) as a function of the frequency. The focused beam corresponds to the beam with the smallest achievable focus. It is used

as the reference for the determination of  $\Delta\varphi$ . Fig.(5.8b) shows the retrieved  $f_0$  and  $\Gamma_0$  for underfocused, focused (black circles) and overfocused beams. The maximum systematic error that arises from the light focus is defined as the change of  $\Gamma_0$  and  $f_0$  between the two focused beams and the closest beam that is clearly identified as overfocused or underfocused. This is indicated by the dashed rectangle. The obtained systematic error of  $f_0$  and  $\Gamma_0$  are 3% and 3.5%, respectively.

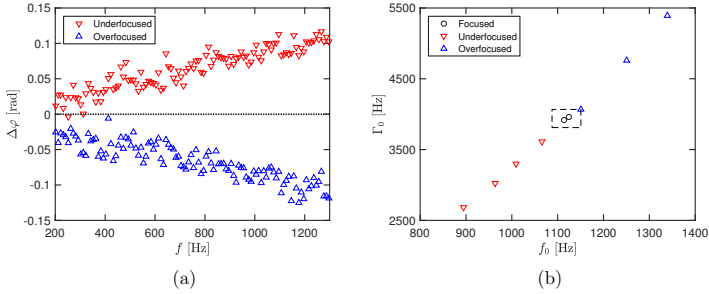


Figure 5.8: Phase measurement at different foci. (a) Phase difference,  $\Delta\varphi$ , between an underfocused and a focused beam (red, upside down triangles) and between an overfocused and a focused beam (blue triangles) as a function of the modulation frequency  $f$ . The horizontal black, dashed line indicates zero phase difference. (b) Fit parameters  $f_0$  and  $\Gamma_0$  measured for the same droplet for underfocused, focused and overfocused beams. The uncertainty of  $f_0$  and  $\Gamma_0$  within the rectangle is  $\pm 3\%$  and  $\pm 3.5\%$ , respectively. These representative measurements are for a droplet with  $R = 1.6\ \mu\text{m}$ .

#### 5.8.4 Size growth factor

To calculate the hygroscopic size growth factor  $R^*(\text{RH}) = R(\text{RH})/R_{\text{dry}}$ , we use the values of  $R(\text{RH})$  determined from BLS measurements (Fig.(5.6); Table (5.1)).  $R_{\text{dry}} = \left(\frac{3}{4\pi} \cdot \frac{m_{\text{NaCl}}}{\rho_{\text{NaCl}}}\right)^{\frac{1}{3}}$  is the radius of a water-free NaCl sphere which has the same mass,  $m_{\text{NaCl}}$ , as the completely dried droplets (“Methods”).  $\rho_{\text{NaCl}} = 2170\ \text{kg m}^{-3}$  is the NaCl density. Several previous studies report  $R^*$  at an RH of 90%<sup>49</sup>. We thus extrapolate our data to an RH of 90% assuming the empirical power law<sup>120</sup>:  $R^*(\text{RH}) = R_0 \cdot \left(1 - \frac{\text{RH}}{100}\right)^{-\alpha}$ , where  $R_0$  and  $\alpha$  are fit parameters. The best fit is shown in Fig.(5.9) (black curve)

together with the optimal fit parameters (legend). The extrapolated value is  $R^*(90\%) = 2.40 \pm 0.02$  in agreement with the theoretical model<sup>110</sup>.

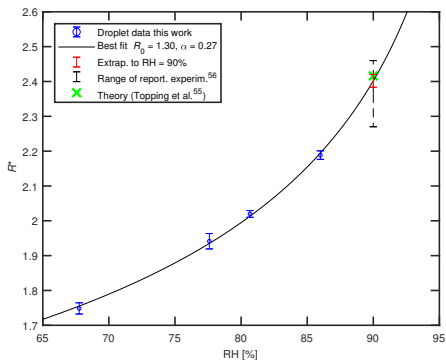


Figure 5.9: Hygroscopic size growth factor  $R^*$  as a function of the RH. Experimental data from this work (blue circles). The error bars of the experimental data indicate the estimated uncertainty of the fits of the BLS (broad band light scattering) spectra; Empirical fit from this work (black curve); Extrapolated value from this work at an RH (relative humidity) of 90% (red interval) with the error bar indicating a 68% confidence interval of the extrapolation; Range of experimental literature values taken from Supplementary Table 1 in Zieger et al.<sup>49</sup> (black dashed interval); Theoretical value from Topping et al.<sup>110</sup> (green cross) assuming the value of pure water ( $72 \text{ mN m}^{-1}$ ) for the droplet surface tension.

## 6 Hygroscopic growth of single atmospheric sea salt aerosol particles from mass measurement in an optical trap

This chapter is a copy of a journal publication:

<b>Title</b>	Hygroscopic growth of single atmospheric sea salt aerosol particles from mass measurement in an optical trap
<b>Authors<sup>a</sup></b>	Oliver Reich, Michael J. Gleichweit, Grégory David, Nicole Leemann and Ruth Signorell
<b>Original article</b>	Environmental Science: Atmospheres (2023)
<b>License</b>	Creative Commons Attributions v4.0 International (CC-BY) <a href="http://creativecommons.org/licenses/by/4.0/">http://creativecommons.org/licenses/by/4.0/</a>

<sup>a</sup> Department of Chemistry and Applied Biosciences, ETH Zurich, Vladimir-Prelog-Weg 2, CH-8093, Zurich, Switzerland

The style of the text and the style, size and placement of the figures and tables have been adapted, as have the numbering of figures, tables and sections.

Author contribution of O.R.: O.R. conceived the project, measured and analyzed most of the data and wrote the main part of the manuscript.

## Abstract

Sea salt aerosol is among the most abundant aerosol species in Earth's atmosphere, and its hygroscopicity is an important parameter to quantify their interaction with solar radiation. Conflicting values for the hygroscopic growth have been reported in the literature, which decreases the accuracy with which their impact on Earth's climate can be modelled. Here we report new values of the hygroscopic growth for a selection of salt compositions representative of atmospheric sea salt. These values are obtained from single optically trapped aqueous droplets with dry Radii between 0.3–2  $\mu\text{m}$ , using a recently developed method for single particle mass measurement in an optical trap. We compare our results to earlier studies and propose a way to reconcile the apparent discrepancies found in the literature. Within our studies, we also observe the crystallization of  $\text{CaSO}_4 \cdot 2\text{H}_2\text{O}$  (Gypsum) during the drying of optically trapped sea salt droplets at significantly larger relative humidity of 65–68 % than the main efflorescence relative humidity at 50 %. This preceding transition occurred in the absence of any contact of the particle with a surface.

## 6.1 Introduction

Atmospheric aerosol particles influence Earth's global radiation budget by scattering and absorbing sun light and by their ability to facilitate cloud formation<sup>1</sup>. Quantitative determination of this impact within the scope of theoretical climate models relies on accurate data about the physical properties of the atmospheric aerosol particles<sup>121</sup>. Along with their distribution in the atmosphere, these include their optical properties and their ability to act as cloud condensation nuclei as well as their hygroscopicity, that is, their ability to take up water from their environment. Depending on the relative humidity (RH) of their environment, hygroscopic particles may change drastically both in mass and size, which in some cases, such as certain inorganic salt aerosol particles, leads to a change of their scattering cross-section by one order of magnitude<sup>48</sup>. The hygroscopicity also plays an important role in the activation of cloud condensation nuclei, as described by Köhler theory<sup>122–124</sup>, which facilitates cloud formation.

Sea salt aerosol is one of the most abundant aerosol species in the atmosphere<sup>125,126</sup>, and as such, has been the subject of many atmospheric studies over the last couple of decades. Usual sea salt aerosol properties such as chemical composition, formation mechanisms and size distributions are explained in detail in the literature<sup>126</sup>. Nowadays sea salt aerosols are also referred to as sea spray when organic components of the marine aerosol are considered<sup>49,127,128</sup>. In this article, we focus on the inorganic sea salt component of sea spray aerosol. Despite the continuing effort, the hygroscopicity of sea salt is not yet quantified with high confidence. In the submicron size range, the hygroscopic growth of an aerosol is typically measured in size selected particle ensembles using hygroscopic tandem mobility analyzers (HTDMA)<sup>114</sup>. The hygroscopic size growth factor at RH 90%, that is, the ratio of the particle size at RH 90% and at low RH, has been reported between 2.11–2.46<sup>49,112,129</sup>, thus spanning a range of approximately 15%. For particles with sizes of a few micrometers, trapping and measuring the hygroscopic growth of single levitated particles using electro-dynamic balances (EDB)<sup>43,96,97</sup> has been widely used. In this size range, the hygroscopic growth of sea salt was for a long time believed to be similar to that of pure NaCl<sup>126</sup>, as measured by Tang et al.<sup>45</sup> In their work, Tang et al. determined the hygroscopic mass growth factor, that is, the ratio of the particle masses at given RH and RH = 0%, of several sea salt compositions and reported values at RH 90% of 7.0 for NaCl and 6.8 for the sea salts. Recently, these values were critically evaluated by Zieger et al.<sup>49</sup>, who found a significantly reduced hygroscopic growth

for submicron and micron sized sea salt particles. For the same size range as in the work of Tang et al. a hygroscopic mass growth factor of 5.24 at RH 90 % was found using EDBs. In the same study, it was shown that such a reduction of the hygroscopic growth parameter in climate models would lead to a reduction in the predicted aerosol optical density over oceanic areas of up to 15 %. The present uncertainty in the available literature data thus significantly limits the accuracy with which the impact of atmospheric sea salt on Earth's climate can be modelled.

In this work, we report new measurements of the hygroscopic mass growth of single NaCl and sea salt particles as well as values for their densities as a function of RH. In contrast to previous studies, we use optical trapping to investigate single particles. The measurement of the hygroscopic mass growth and density is facilitated by an approach combining the measurement of the particle's size and molecular composition via Raman spectroscopy with a recently developed method for mass measurement of single optically trapped aerosol particles<sup>60</sup>. While mass measurements with EDBs are typically limited to particles with sizes of a few micrometers and above, our approach enables us to report data also for the large submicron size range. In comparison with the values reported by Tang et al.<sup>45</sup> and Zieger et al.<sup>49</sup> for micrometer sized particles, we find that our data are very similar to the results of Tang et al. We also take a critical look at the definition of the reference dry mass used for the derivation of the hygroscopic mass growth factors, which has to be taken into account for their correct implementation into existing climate models. This is discussed in particular with regard to the presence of hydrates in sea salt at dry conditions, which might explain the apparent discrepancies observed in the literature.

## 6.2 Methods

### 6.2.1 Optical trapping

We use counter-propagating optical tweezers (CPT)<sup>31,32,60,87,103,105-107</sup> to confine and isolate single particles under tightly controlled environmental conditions. The layout of the optical trap is shown in Fig.(6.1) and consists of a continuous green laser beam (Novanta Photonics, Opus 532) that is expanded roughly 4 times and afterwards split using a polarizing beam splitter (PBS). The two counter-propagating beams are aligned on a single axis and

focused into the trapping cell to form the electrodynamic trapping potential. The power ratio of the two trapping beams is adjusted by changing the polarization state of the beam prior to the PBS using an electro-optic modulator (EOM, ConOptics, 350-50-01 RP). Harmonic oscillation of the trapped particle along the beam propagation axis is induced by periodically modulating the relative power of the two trapping beams<sup>60</sup>, which is exploited to measure the particle's mass as explained below.

The trapped particles investigated in this study are aqueous droplets generated from bulk solution using an atomizer (TSI, 3076). To study the hygroscopicity of atmospheric sea salt aerosol droplets, aqueous solutions with three different salt compositions were prepared and used as representatives: Pure NaCl (> 99%, Merck, 1.06404.1000), a mixture of NaCl + MgCl<sub>2</sub>·6 H<sub>2</sub>O (Sigma-Aldrich, 63068) + Na<sub>2</sub>SO<sub>4</sub> (Sigma-Aldrich, 238597) which we denote sea water 1 (SW 1) and a commercial sea water solution (Sigma Aldrich, SSWs) which we denote sea water 2 (SW 2). The specific ionic compositions of SW 1 and SW 2 are listed in Table (6.1). Note that the absolute ion concentrations in the bulk solutions do not correspond to the absolute ion concentrations in the trapped droplet, since the latter also depend on the RH inside the trapping cell, which governs the amount of water in the droplet. The relative concentrations in the bulk solution and the droplets, however, are the same.

The droplets are trapped inside a custom made cell, shown in Fig.(6.2), which enables us to control the droplets's environment. The cell is filled with nitrogen gas, and the RH inside the cell is controlled by mixing a wet and dry nitrogen flow with adjustable flow rates. All experiments were conducted at room temperature ( $T = 21.7 \pm 0.2^\circ$ ) and ambient pressure. Temperature and RH are monitored by a sensor (Sensirion, SHT35) during the experiments.

## 6.2.2 Size measurement

Aqueous droplets are almost perfectly spherical by virtue of the water surface tension. For sizing of spherical particles, we use broad-band light scattering<sup>32</sup> (BLS), as depicted in Fig.(6.2). A fiber coupled broad-band light source (Energetiq, LDLS EQ-99X) with spectral range 190–2500 nm is focused on the particle through the bottom window of the cell. The elastically scattered light is collected under a scattering angle of  $105 \pm 13^\circ$  and fiber-coupled into a high sensitivity, low-noise spectrometer (Andor, SR-303i-A).



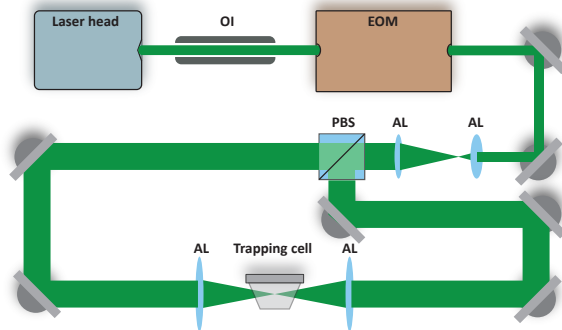


Figure 6.1: Counter-propagating optical tweezers setup. The purpose of the electro-optic modulator (EOM) and the polarizing beam splitter (PBS) is explained in the main text. The beams are expanded and later focused into the trapping cell using aspherical lenses (AL). An optical isolator (OI) protects the laser cavity from the trapping beams propagating backwards towards the source. Figure adapted from Reich et al.<sup>59</sup> under Copyright 2021 Society of Photo-Optical Instrumentation Engineers (SPIE).

The BLS spectrum is recorded in the range 300–500 nm and compared with simulations using Mie theory. The fitting of the experimental BLS spectrum with the simulated spectra proceeds as described in detail in our previous work<sup>60</sup>. From the fit, the radius and wavelength dependent refractive index of the particle are determined with a typical size accuracy of better than 1%.

### 6.2.3 Harmonic oscillator model for determination of particle mass

Optical trapping is currently not widely used for mass measurement of single aerosol particles, and the technique used in this paper has been developed only recently<sup>60</sup>. Its principle is based on the relation between the particle mass and the observed phase delay of the induced particle oscillation with respect to the trap modulation. In quantitative terms, the particle oscillation in the modulated CPT is described using a one-dimensional driven and damped harmonic oscillator model. Denoting  $z(t)$  the position of the particle in time along the trapping beam axis and  $z_0(t) = Z_0 \sin(2\pi ft)$  the time

	SW 1	SW 2	Zieger et al. <sup>49</sup>	Tang et al. <sup>45</sup>
Na <sup>+</sup>	10.45 (100)	11.03 (100)	10.87 (100)	(100)
Cl <sup>-</sup>	18.87 (183)	19.84 (180)	19.53 (180)	(171)
Mg <sup>2+</sup>	1.37 (13)	1.33 (12)	1.32 (12)	(12)
SO <sub>4</sub> <sup>2-</sup>	2.68 (28)	2.77 (25)	2.66 (25)	(25)
Ca <sup>2+</sup>		0.42 (3.8)	0.40 (3.7)	
K <sup>+</sup>		0.39 (3.6)	0.35 (3.2)	
HCO <sub>3</sub> <sup>-</sup>		0.15 (1.3)	0.17 (1.6)	
Br <sup>-</sup>		0.067 (0.6)		
BO <sub>3</sub> <sup>3-</sup>		0.029 (0.3)	0.031 (0.3)	
Sr <sup>2+</sup>		0.013 (0.1)	0.008 (0.081)	
F <sup>-</sup>		0.0014 (0.01)		

Table 6.1: Sea salt compositions used in this study and in the reference studies, with units of [g / 1 kg H<sub>2</sub>O]. Values in brackets are normalized with respect to Na<sup>+</sup>. The absolute values for the results of Tang et al. are unknown.

dependent equilibrium position of the optical trap during modulation, with  $f$  the frequency and  $Z_0$  the amplitude of the modulation, the optical force on the particle can be written as

$$F_{\text{opt}} = -k \cdot (z(t) - z_0(t)) = -k z(t) + kZ_0 \sin(2\pi ft) \quad (6.1)$$

Here  $k$  is the spring constant, or optical stiffness, of the trapping potential. For particles trapped at ambient conditions, an additional force arises due to the damping of the surrounding medium. For spherical droplets, the damping can be divided into a main contribution from the Stokes' drag and correction terms<sup>72</sup> accounting for the non-uniform motion of the particle and the inertia of the surrounding gas:

$$F_{\text{damp}} = F_{\text{Stokes}} + F_{\text{corr}} \quad (6.2)$$

where

$$F_{\text{Stokes}} = -\gamma \cdot \dot{z} \quad (6.3)$$

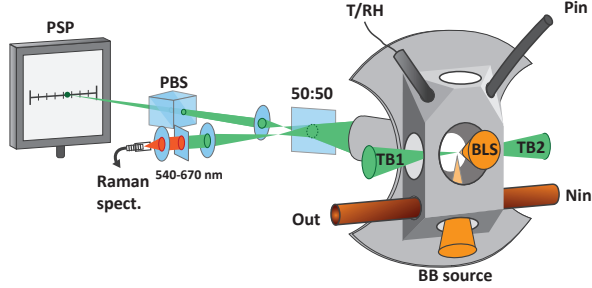


Figure 6.2: Trapping cell and measurement setups. The cell is custom made with an opening for the temperature and relative humidity sensor (T/RH). Particles are introduced into the cell via the inlet at the top (Pin). The nitrogen flow enters at the bottom of the cell (Nin) and exits together with the excess particles via an exhaust (Out). The scattered light of the trapping beams (TB1 and TB2) is collected through the back window. The scattered light beam is split, with half the power being focused on the position sensing photodiode (PSP) for the tracking of the particle position. The polarizing beam splitter (PBS) effectively removes one of the two scattered light beams and improves the accuracy of the particle tracking. The other half of the scattered light is fiber coupled into a spectrometer for measurement of the Raman spectrum. To determine the size of the particle, light from a broad-band light source is focused on the trapped particle from the bottom window (BB source) and the scattered light is collected through the front window for measurement of the broad-band light scattering (BLS) spectrum. Part of the figure adapted from Reich et al.<sup>59</sup> under Copyright 2021 Society of Photo-Optical Instrumentation Engineers (SPIE).

and

$$F_{\text{corr}} = - \left( \frac{\pi \rho_{N_2}}{\mu_{N_2}} f \right)^{\frac{1}{2}} R \gamma \cdot \dot{z} - \frac{1}{2\pi} \left( \left( \frac{\pi \rho_{N_2}}{\mu_{N_2}} \frac{1}{f} \right)^{\frac{1}{2}} R + \frac{2}{9} \frac{\pi \rho_{N_2}}{\mu_{N_2}} R^2 \right) \gamma \cdot \ddot{z} \quad (6.4)$$

Here  $\dot{z}$  and  $\ddot{z}$  are the velocity and acceleration of the particle, respectively,  $\gamma = 6\pi\mu_{N_2}R\frac{1}{1+C_c(R)}$  is the Stokes' drag coefficient with Cunningham slip correction<sup>73</sup> ( $C_c$ ),  $\mu_{N_2}$  is the viscosity of the surrounding nitrogen gas,  $R$  is the radius of the droplet and  $\rho_{N_2}$  the density of nitrogen gas. The value of  $C_c$  for micrometer sized particles is given by  $C_c(R) = C_0 \frac{\lambda_{\text{free}}}{R}$ , where  $\lambda_{\text{free}}$  is the mean free path in the surrounding nitrogen gas and  $C_0 = 1.257$  an empirical constant<sup>74</sup>.

The optical force and the damping forces combined drive the particle dynamics according to

$$m\ddot{z} = F_{\text{opt}} + F_{\text{damp}} \quad (6.5)$$

where  $m$  is the mass of the particle. Plugging Eq.(6.1)-Eq.(6.4) into Eq.(6.5) yields

$$\left(1 + \Gamma_1 f^{-\frac{1}{2}} + \Gamma_2\right) \cdot \ddot{z} + 2\pi \left(\Gamma_0 + \Gamma_1 f^{\frac{1}{2}}\right) \cdot \dot{z} + 4\pi^2 \Omega_0^2 \cdot z = 4\pi^2 \Omega_0^2 Z_0 \sin(2\pi f t) \quad (6.6)$$

where

$$\Omega_0 = \frac{1}{2\pi} \left(\frac{k}{m}\right)^{\frac{1}{2}} \quad (6.7)$$

$$\Gamma_0 = \frac{1}{2\pi} \frac{\gamma}{m} \quad (6.8)$$

are the eigenfrequency and the damping rate of the harmonic oscillator, respectively, and  $\Gamma_1 = \left(\frac{\pi\rho_{\text{N}_2}}{\mu_{\text{N}_2}}\right)^{\frac{1}{2}} R \cdot \Gamma_0$  and  $\Gamma_2 = \frac{2}{9} \frac{\pi\rho_{\text{N}_2}}{\mu_{\text{N}_2}} R^2 \cdot \Gamma_0$  are the damping rate correction terms. Eq.(6.6) is solved by  $z(t) = A \cdot \sin(2\pi f t - \varphi)$ , where the particle oscillation amplitude  $A$  and phase  $\varphi$  are given by

$$A = Z_0 \frac{\Omega_0^2}{\sqrt{\left(\Omega_0^2 - (1 + \Gamma_2)f^2 - \Gamma_1 f^{\frac{3}{2}}\right)^2 + \left(\Gamma_0 f + \Gamma_1 f^{\frac{3}{2}}\right)^2}} \quad (6.9)$$

$$\varphi = \arctan\left(\frac{\Gamma_0 f + \Gamma_1 f^{\frac{3}{2}}}{\Omega_0^2 - (1 + \Gamma_2)f^2 - \Gamma_1 f^{\frac{3}{2}}}\right) \quad (6.10)$$

We thus obtain measurable quantities which depend on the free parameters  $\Omega_0$  and  $\Gamma_0$  and the controlled parameters  $Z_0$  and  $f$ . Note that  $\Gamma_1$  and  $\Gamma_2$  are not independent parameters as they are connected to  $\Gamma_0$  by constants and the radius of the particle, which is known from BLS.

## 6.2.4 Mass measurement

By measuring the phase  $\varphi$  as a function of modulation frequency  $f$  and fitting it with Eq.(6.10) we can determine the eigenfrequency  $\Omega_0$  and damping rate  $\Gamma_0$  of the harmonic oscillator. As explained in more detail in our previous

work<sup>60</sup>, the oscillation amplitude  $A$  is not suited for retrieval of  $\Omega_0$  and  $\Gamma_0$  due to the large correlation between these parameters in Eq.(6.9).

The phase  $\varphi$  of the particle oscillation is measured by tracking the particle position along the trapping beam axis during the trap modulation as shown in Fig.(6.2). The scattered light from the trapping beams is collected under a scattering angle of  $90 \pm 24^\circ$  using an objective (Mitutoyo, Plan Apo 20x) with relatively high numerical aperture (NA 0.42). This scattered light is split equally in power to allow simultaneous Raman measurements explained later, and one branch is focused on a position sensing photodiode (PSP, Thorlabs, PDP90A). The oscillation of the particle translates into an amplified oscillation of the focused image on the photosensitive area of the PSP, and the PSP signal is measured together with the modulation signal used to drive the EOM. From these two measurements, the demodulated amplitude and phase of the particle oscillation is obtained using a lock-in detection scheme. For accurate mass measurements, the artificial increase in the phase measurement due to the impedance of the PSP is determined and corrected as described in our previous work<sup>60</sup>. Previously, an additional systematic measurement bias of up to 3.5% in the position was reported for micrometer sized particles. This bias arises due to the superposition of the two particle images from the respective trapping beam on the PSP. Using cross-polarized trapping beams and filtering the scattered light using a PBS effectively suppresses one of the particle images and thus removes this bias.

From  $\Gamma_0$  determined by the measurement of  $\varphi$  and the particle radius  $R$  determined by BLS, the mass of the particle is obtained using Eq.(6.8)

$$m = \frac{1}{2\pi} \frac{\gamma}{\Gamma_0} = \frac{3\mu_{N_2} R}{\left(1 + C_0 \frac{\lambda_{\text{free}}}{R}\right) \Gamma_0} \quad (6.11)$$

As an added benefit, the density of the spherical particle is obtained as

$$\rho = \frac{m}{V} = \frac{\frac{1}{2\pi} \frac{\gamma}{\Gamma_0}}{\frac{4}{3}\pi R^3} = \frac{9\mu_{N_2}}{4\pi \left(1 + C_0 \frac{\lambda_{\text{free}}}{R}\right) R^2 \Gamma_0} \quad (6.12)$$

### 6.2.5 Raman measurement and determination of particle dry mass

To determine the trapped particle's molecular composition, its Raman spectrum is measured as shown in Fig.(6.2). The second branch of the scattered trapping beams not used for the particle tracking is fiber-coupled into a high sensitivity, low-noise spectrometer (Andor, KY-328i-A). The elastically scattered light at 532 nm is filtered out prior to the fiber coupling and only the range 540–670 nm is measured, which corresponds to Stokes shifts of approximately 270–3800  $\text{cm}^{-1}$ . This range contains in particular the S–O symmetric stretching vibration of  $\text{SO}_4^{2-}$  ( $\nu_1\text{-SO}_4^{2-}$ ,  $\sim 980 \text{ cm}^{-1}$ ) and the O–H symmetric stretching vibration of  $\text{H}_2\text{O}$  ( $\nu_s\text{-H}_2\text{O}$ , 2700–3750  $\text{cm}^{-1}$ ).

Many examples of quantitative Raman spectroscopy for the determination of the sulfate mass fraction of a given aqueous solution can be found in the literature<sup>130–133</sup>. In particular, the ratio of the peak heights of the  $\nu_1\text{-SO}_4^{2-}$  and  $\nu_s\text{-H}_2\text{O}$  modes and the ratio of their peak areas have both been shown to be proportional to the sulfate concentration of the solution to a good approximation<sup>131,133</sup>. With respect to these earlier studies on bulk samples, the analysis of single particle Raman spectra is made more complex due to the presence of morphology dependent resonances, or whispering gallery modes (WGM)<sup>58</sup>, that arise due to the particle's spherical shape. More precisely, only Raman spectra where the  $\nu_1\text{-SO}_4^{2-}$  and  $\nu_s\text{-H}_2\text{O}$  bands do not overlap with a WGM can be used for quantitative analysis. After these spectra have been identified by visual inspection, the peak heights of the  $\nu_1\text{-SO}_4^{2-}$  and  $\nu_s\text{-H}_2\text{O}$  modes are determined and compared with the calibration curve, which is obtained from a dilution series of SW 1. The data used to obtain the calibration curve is shown in Fig.(6.3). From the standard deviation of the calibration curve with respect to the known mass fractions of the bulk solutions, we find an average uncertainty of 5.1 % for the determination of the  $\text{SO}_4^{2-}$  mass fraction. The calibration curve is also suited for the commercial solution with composition SW 2, since the two compositions differ only in terms of trace ion species in very low abundance.

The mass of  $\text{SO}_4^{2-}$  is determined from the mass measurements and the calibrated Raman spectra of each particle. The total amount of salt is determined from the  $\text{SO}_4^{2-}$  mass using the relative mass fractions listed in Table (6.1) for the respective composition. We refer to this salt mass as  $m_{\text{dry}}$ , the dry mass of the particle. Different definitions of the dry mass are used in the literature, in particular, the dry mass is often used to describe the mass of the

particle in an environment at 0% RH, or at a RH below a certain threshold. This is not necessarily the same mass as the one used in our case, due to the presence of hydrates that persist at dry conditions. We will comment on the implications of the different definitions of the dry mass at a later stage in this work. For now, we return to the definition of the hygroscopic mass growth factor,  $m^*$ , which is obtained from the dry mass as

$$m^*(\text{RH}) = \frac{m(\text{RH})}{m_{\text{dry}}} \quad (6.13)$$

where  $m(\text{RH})$  is the mass of the particle at relative humidity RH.

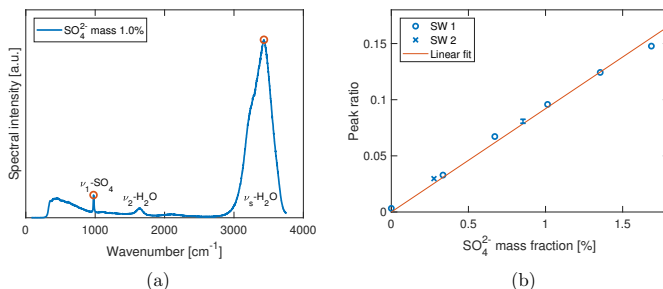


Figure 6.3: Calibration of Raman spectra for the determination of the  $\text{SO}_4^{2-}$  mass fraction. (a) Example spectrum of a bulk solution with composition SW 1 diluted to 1%  $\text{SO}_4^{2-}$  mass fraction. The S–O symmetric stretching ( $\nu_1\text{-SO}_4$ ), H–O bending ( $\nu_2\text{-H}_2\text{O}$ ) and symmetric O–H stretching ( $\nu_s\text{-H}_2\text{O}$ , 2700–3750  $\text{cm}^{-1}$ ) modes are labeled, and the  $\nu_1\text{-SO}_4$  and the  $\nu_s\text{-H}_2\text{O}$  peaks used for quantitative analysis are indicated by empty circles. (b) Ratio of the  $\nu_1\text{-SO}_4$  to  $\nu_2\text{-H}_2\text{O}$  peak as function of the  $\text{SO}_4^{2-}$  mass fraction in a dilution series of composition SW 1. The corresponding values for the commercial solution with composition SW 2 are indicated as well. The solid line represents the best linear fit through the origin. The single error bar indicates the standard deviation over 7 repetitions which have been performed for one of the dilutions of SW 1.

## 6.3 Results and discussion

### 6.3.1 Hygroscopicity of NaCl droplets

Aqueous NaCl is the simplest system commonly used to represent atmospheric sea salt droplets. The bulk properties are very well known<sup>109,111</sup>. Our hygroscopic measurements of NaCl droplets allow us to demonstrate the accuracy of our mass and size measurement. To compare droplets with different sizes directly with bulk solutions, the density and the hygroscopic mass growth factor of the droplets is calculated from the mass and size measurements. A list with the mass and size measurements used to calculate the densities and mass growth factors can be found in the data repository.

The resulting densities are shown in Fig.(6.4a). For reference, the data from previous EDB work by Tang et al.<sup>45</sup> is also shown and compared with bulk solution densities. The RH range above the critical value of 75.3% for NaCl<sup>108</sup> corresponds to undersaturated droplets/solutions. In this range the bulk values coincide with the EDB measurements. In contrast to bulk solutions, for RH below the critical RH the droplets remain homogeneous and liquid in a supersaturated state until efflorescence occurs at an RH of approximately 50%. In the supersaturated range, only the comparison with EDB results is possible. Overall, we observe good agreement between our measurement data and the results of Tang et al. To further analyze the size dependency of our accuracy, the data is grouped into three size categories: “Submicron” indicates droplets with dry radii  $R_{\text{dry}} < 0.5 \mu\text{m}$ , “intermediate” indicates  $R_{\text{dry}} = 0.5\text{--}1.0 \mu\text{m}$  and “supermicron”  $R_{\text{dry}} > 1.0 \mu\text{m}$ . The reference data by Tang et al. accordingly classifies as supermicron. The dry size of each of our droplets is obtained from the dry mass  $m_{\text{dry}}$  and the density of pure NaCl,  $\rho_{\text{NaCl}} = 2170 \text{ kg m}^{-3}$ . The dry mass is determined from the mass measurements at undersaturation and the NaCl salt mass fractions obtained from the comparison with bulk solutions with corresponding water activities. The dry mass of a given droplet is obtained as the average over all retrieved values for that droplet. For a small number of droplets, no suitable mass measurements were performed in the undersaturated RH range. For these droplets, the dry mass was determined from the hygroscopic mass growth factors at supersaturation measured by Tang et al.<sup>45</sup> and treated as estimates by way of precaution. In the study presented here, droplets with dry sizes in the range  $R_{\text{dry}} = 0.3\text{--}2 \mu\text{m}$  have been investigated. Intermediate and supermicron droplets are observed to exhibit average measurement uncertainties of



8 % and 4 %, respectively, for the droplet density. This uncertainty rises to approximately 10 % for submicron droplets.

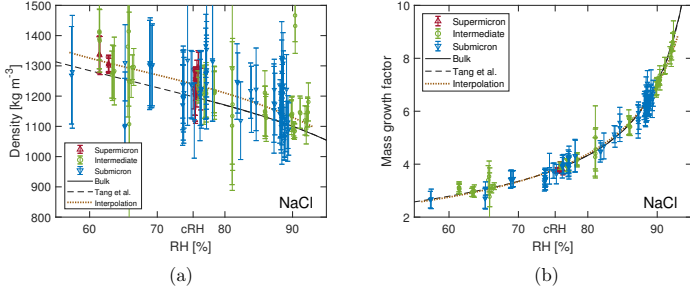


Figure 6.4: Hygroscopicity of aqueous NaCl droplets. (a) density and (b) hygroscopic mass growth factor as a function of relative humidity (RH). Our data is divided into three groups according to the dry size of the corresponding droplets. For comparison, the bulk values and data of supermicron particles from previous EDB work by Tang et al.<sup>45</sup> are also shown as solid and dashed line, respectively (the data by Tang et al. is represented by a fourth order polynomial using the coefficients given in their work). The dotted line represents the interpolation of our data with a weighted polynomial fit. The critical RH of NaCl at 75.3% is indicated as cRH. Vertical error bars indicate the uncertainty arising from the droplet size and mass measurement.

Compared with the results of Tang et al. we observe a small bias towards larger densities in our measurements for all droplet sizes. For a quantitative analysis we interpolate our data using a third order polynomial fit, weighted by the inverse square of the individual measurement uncertainties. The third order represents the best compromise between determinacy and flexibility of the interpolation. On average our values lie 2–3% above the bulk densities in the undersaturated RH range, a value that is within the indicated experimental uncertainty of the setup. This small bias may be a residual artifact of the phenomenon reported in our previous work<sup>60</sup>, where for certain particle size-to-laser wavelength ratios, the particle oscillation has been observed to stop at specific instances during the modulation cycle. This additional delay leads to an artificial increase in the phase  $\varphi$  in the harmonic oscillator model and thus to an increase of the mass and density. This phenomenon is prevalent in CPTs with parallel polarized trapping beams<sup>59</sup>, and is therefore not significant in this work where we use perpendicular polarized beams, although a residual artifact of 2–3% cannot be ruled out.

The hygroscopic mass growth factors derived from the mass measurements and the determined dry masses are shown in Fig.(6.4b). For the droplets, where the dry mass could not be determined from the bulk solutions due to lack of measurements at undersaturation, no hygroscopic mass growth factors are reported. Very good agreement with the reference bulk data and the data by Tang et al. is observed. It is common to report the hygroscopic growth factors at the RH of 90 %. To determine the average hygroscopic mass growth factor, we interpolate our data with an empirical two parameter hygroscopic growth function

$$m^*(\text{RH}) = m_{90}^* \cdot \left( 10 - 10 \frac{\text{RH}}{100\%} \right)^{-\alpha} \quad (6.14)$$

where  $m_{90}^*$  is the value at RH 90 % and  $\alpha$  is the empirical hygroscopic growth parameter. For the fit, the same weights are applied as for the density data. The hygroscopic mass growth at RH = 90 % is found to be  $6.99 \pm 0.02$ , where the error indicates the uncertainty of the interpolation (standard deviation of the fitted  $m_{90}^*$ ). It should be noted that by construction of the mass growth factors, any systematic bias in the mass measurement is effectively removed by the normalization with the calculated  $m_{\text{dry}}$ . This allows to determine the random error of our measurements. The standard deviation of our individual mass growth factors with respect to the bulk solution for RH above the critical RH of 75.3 % indicates an absolute value of 0.13 and a relative value of 2 % for supermicron and intermediate droplets, and respective values of 0.22 and 4 % for submicron droplets. The measurement uncertainty for supermicron and intermediate droplets is comparable to previous EDB studies. For submicron droplets, to the best of our knowledge, no comparable EDB data exists. In conclusion, the technique provides reliable measurement data over a wide range of droplet masses and sizes.

### 6.3.2 Hygroscopicity of mixed salt droplets

We used the same procedure as above to analyze the mass and size measurements of the two sea salt compositions SW 1 and SW 2. Our results are compared to previous EDB work of Tang et al.<sup>45</sup> and Zieger et al.<sup>49</sup>, who published conflicting values for the hygroscopic growth factors of sea salt. The sea salt compositions used for these studies are listed in Table (6.1). Our compositions are very similar to that of Zieger et al. with regard to the relative abundance of major ions ( $\text{Na}^+$ ,  $\text{Cl}^-$ ,  $\text{Mg}^{2+}$ ,  $\text{SO}_4^{2-}$ ). While Zieger et

al. have conducted a systematic study across different measurement setups and particle sizes, for particle sizes larger than the nanometer size range, only single values for the hygroscopic mass and size growth factor at RH 90% were reported. Thus we can only compare the hygroscopic mass growth factor at RH 90% directly with the results of Zieger et al.

The densities of SW 1 and SW 2 are shown in Fig.(6.5). For quantitative comparison, a weighted third order polynomial fit is performed on our density data as described above for the NaCl measurements. No significant difference of the densities between SW 1 and SW 2 can be observed. We observe slightly larger densities for RH below 90% for both sea salt solutions than the corresponding values by Tang et al. The average deviations between our fit and the data by Tang et al. are 3% and 2% for RH above 90%, 5% and 4% for RH in the range 80–90%, and 5% and 6% for RH < 80% for composition SW 1 and SW 2, respectively. For the range RH < 90%, the discrepancy is larger than the bias observed in the NaCl data. At the same time, the experimental uncertainties for measurements with SW 1 and SW 2 are slightly smaller (3–7% at average) than those with NaCl due to overall better trapping alignment during the measurement series. Even taking into account the indicated measurement uncertainty, a small but systematic discrepancy in the droplet density of 1–2% remains for RH below 90% between our measurements and the results of Tang et al.

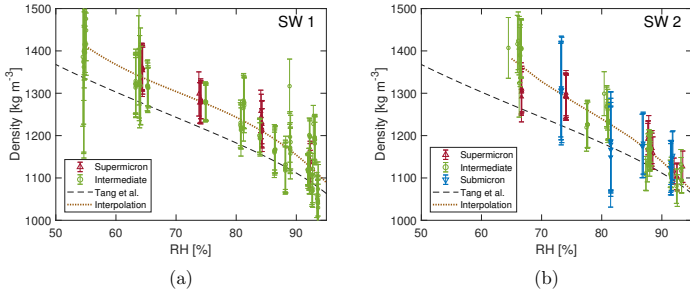


Figure 6.5: Density of sea salt as a function of RH. (a) data of composition SW 1. (b) data of composition SW 2. The same size categories as for the NaCl measurements are applied. Data from previous EDB work by Tang et al.<sup>45</sup> is shown for comparison (dashed line, polynomial interpolation). The dotted line represents the interpolation of our data with a weighted polynomial fit for quantitative analysis. The error bars are defined as for the NaCl measurements.

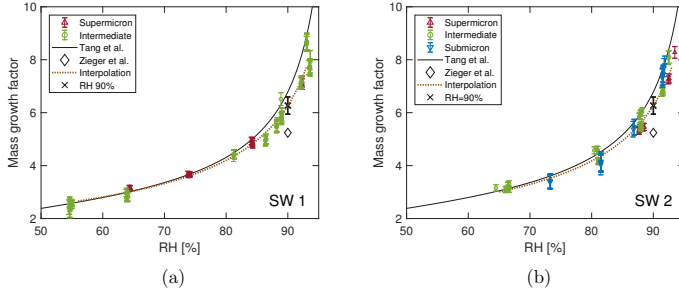


Figure 6.6: Hygroscopic mass growth factors of sea salt. (a) data of composition SW 1. (b) data of composition SW 2. The same size categories as for the NaCl measurements are applied. Data from previous EDB work Tang et al.<sup>45</sup> (solid line, polynomial interpolation) and Zieger et al.<sup>49</sup> (diamonds) are shown for comparison. The dotted line represents the interpolation of our data (Eq.(6.14)) and the cross indicates the value at RH 90% with the systematic uncertainty of the Raman calibration in the determination of the dry mass. The error bars of our measurement data are defined as for the NaCl measurements.

In addition to the size and mass measurement, a Raman spectrum is recorded every two minutes for quantitative determination of the salt mass fraction. From this data and the droplet mass, the hygroscopic mass growth factors are determined as explained in the Methods section. This data is shown in Fig.(6.6). For both sea salt composition SW 1 and SW 2, overall good agreement with the reference data by Tang et al. is observed. We observe somewhat smaller growth factors for  $RH > 85\%$ . As for the NaCl data, we quantify the average hygroscopic mass growth factor by performing a weighted fit with Eq.(6.14). From this interpolation, we obtain an average value of  $m^*(90\%) = 6.3 \pm 0.3$  for both compositions SW 1 and SW 2. The uncertainty range is given by the uncertainty of 5.1% of the calibration of the Raman spectra as specified in the Methods section. Our value is very similar to the one reported by Tang (6.8) and approximately 20% larger than the mass growth factors published by Zieger et al. (5.24 for supermicron particles). The similarities between SW 1 and SW 2 in both the densities and the hygroscopic mass growth factors show that the presence of the ions of low abundance ( $\text{Ca}^{2+}$ ,  $\text{K}^+$ ,  $\text{HCO}_3^-$ ,  $\text{Br}^-$ ,  $\text{BO}_3^{3-}$ ,  $\text{Sr}^{2+}$ ,  $\text{F}^-$ ) is not significant for the hygroscopic growth of sea salt particles.

### 6.3.3 Importance of the definition of the salt dry mass for hygroscopic mass growth factors

How to reconcile the different experimental results regarding the hygroscopic mass growth factors in the literature? The hygroscopic mass growth factors in both the study by Tang et al. and that by Zieger et al. are defined with respect to the mass of the particle measured at RH 0%. It has already been pointed out by Tang et al., and reiterated by Zieger et al., that even at this low RH, the presence of hydrates in the crystalline salt sample is likely. However, neither study reports the composition of the hydrates in the salt mass used for the determination of the mass growth factors. The presence of hydrates leads to an increased salt mass compared with the anhydrous salt mass, which is used for reference in our study. Accordingly, the mass growth factors derived from the hydrated salt mass are expected to tend towards lower values than mass growth factors derived from the anhydrous salt mass.

The comparison with our data implies that in the case of Tang et al. there is only an insignificant amount of hydrates in the dried salt mass, as we do not observe larger hygroscopic mass growth values as would be expected otherwise. By contrast, our data even tends towards 3–13% lower values at RH 90%, which may be due to the slightly different sea salts used in the studies, in particular with regard to the  $\text{Na}^+/\text{Cl}^-$  ratio of the composition. Conversely, the hygroscopic mass growth factors of Zieger et al. are approximately 20% smaller. This is a plausible deviation if one considers the presence of hydrates in the dried sample of Zieger et al. If, as an example, in a salt crystal with ionic composition SW 2 the naturally occurring hydrates  $\text{MgCl}_2 \cdot 6\text{H}_2\text{O}$  and  $\text{Na}_2\text{SO}_4 \cdot 10\text{H}_2\text{O}$  were formed instead of the anhydrous  $\text{MgCl}_2$  and  $\text{Na}_2\text{SO}_4$ , the salt mass would increase by 30% and the mass growth factors would decrease by the same relative amount. At this point, the question arises as to why Tang et al. and Zieger et al. obtain significantly different hydration states in their respective dry sample, even though they employ the same measurement principles. We are not familiar with all the details of either of the used setups, hence our explanation here must remain speculative. It is, however, worth highlighting a few features of the experimental setups in question. Zieger et al. generate single droplets from salt solution using an ink-jet cartridge<sup>49</sup>, while a custom made “particle gun”<sup>71,134</sup> with similar functionality was used in the study by Tang et al. The particle generation methods are comparable; hence they are likely not related to the observed differences in the measurement data. Tang et al. initially pump the trapping chamber down to pressures of approximately

$10^{-7}$  mbar<sup>71</sup> before the dry mass is determined, whereas the pressure in the setup by Zieger et al. does not go below 150 mbar<sup>135</sup>. Although previous studies suggest that vacuum pumping without heating is not efficient in removing hydrates from macroscopic samples<sup>136</sup>, it is plausible that it has an enhanced effect on a single micrometer sized levitated sample. The absence of hydrates in the experiments by Tang et al. could therefore be related to their removal by vacuum pumping prior to the measurement of the dry mass.

The above considerations underline the importance of the definition of the salt mass in quantifying the hygroscopic growth of atmospheric particles. In our study, the anhydrous salt mass is used as reference. In studies, where it is not possible or not desired to use the anhydrous mass as reference, quantitative determination of the hydrates in the dried sample is suggested as a method to improve comparability with other literature data. Calibrated Raman spectroscopy may be used to this end, in analogy to the determination of the dry mass of a droplet presented earlier, however, this approach was not investigated further in this study. Such complementary data increases the transferability and overall reliability of determined values and might reconcile apparent discrepancies in hygroscopic growth factors reported in the literature.

### 6.3.4 Significance of these hygroscopicity measurements of sea salt droplets

As explained hereafter, the hygroscopicity measurements presented here are expected to be applicable to most sea salt aerosols (the inorganic part of sea spray or marine aerosols). The composition of generated sea salt droplets is very similar to the composition of the sea waters from which the droplets are formed<sup>126</sup>, and the oceans have a very similar chemical composition<sup>126</sup>. The difference in salinity of different bodies of water does not affect the hygroscopicity of the generated droplets. Hence generated sea salt droplets have, to a good approximation, a similar chemical composition around the globe. As an example, consider the following two sea waters:

- a) 10 g of  $\text{Na}^+$ /kg  $\text{H}_2\text{O}$ , 19 g of  $\text{Cl}^-$ /kg  $\text{H}_2\text{O}$ , 1 g of  $\text{Mg}^{2+}$ /kg  $\text{H}_2\text{O}$ , 3 g of  $\text{SO}_4^{2-}$ /kg  $\text{H}_2\text{O}$
- b) 40 g of  $\text{Na}^+$ /kg  $\text{H}_2\text{O}$ , 76 g of  $\text{Cl}^-$ /kg  $\text{H}_2\text{O}$ , 4 g of  $\text{Mg}^{2+}$ /kg  $\text{H}_2\text{O}$ , 12 g of  $\text{SO}_4^{2-}$ /kg  $\text{H}_2\text{O}$ .

Sea salt droplets made from sea waters a) and b) will have exactly the same hygroscopicity, because the different ions have the same relative abundance. At any RH, the thermodynamic equilibrium of the droplet, which determines the equilibrium concentrations of the ions and water in the droplet, is only dictated by this relative abundance of the ions (which remains the same between the sea water and droplet at any RH). Hence droplets made from two bodies of water with different salinities will still have the same mass growth factor and size growth factor, as long as they have the same relative abundance of ions. Droplets made from sea water with slightly different relative abundance of ions may have a slightly different thermodynamic equilibrium and hence slightly different hygroscopicity. However our results show that small changes of the relative abundance of ions in the sea water, like between SW 1 and SW 2, have no significant influence on the particle hygroscopicity. Even NaCl and sea salt droplets have similar hygroscopic growths. Hence the hygroscopicity measurements presented in this paper appear to be representative for most inorganic sea salt droplets when the influence of hydrates is properly taken into account.

## 6.4 Evolution of Raman spectra and phase transition preceding efflorescence

Extending the analysis of the measured Raman spectra, we can gain further insight into the drying process of aqueous sea salt droplets. The evolution of the Raman spectra for a representative selection of sea salt particles is shown in Fig.(6.7). Over the course of the measurement series, the RH is gradually lowered from approximately 90 % to a final RH of 50–60 % and a Raman spectrum is recorded every 2 minutes. To separate the molecular peaks of interest from the WGM present in spectra of spherical particles, the Raman spectra are normalized with respect to the water peak at  $1632\text{ cm}^{-1}$  and stacked from left to right in chronological order. The molecular peaks are identified as the horizontal lines which do not shift position during the shrinking as a consequence of the drying of the particle. In particular, the S–O symmetric stretching ( $\nu_1\text{-SO}_4$ ,  $976\text{ cm}^{-1}$ ), H–O bending ( $\nu_2\text{-H}_2\text{O}$ ,  $1632\text{ cm}^{-1}$ ) and symmetric O–H stretching ( $\nu_s\text{-H}_2\text{O}$ ,  $2700\text{--}3750\text{ cm}^{-1}$ ) modes are identified as well as the stretching mode of the nitrogen in the gas phase ( $\nu_1\text{-N}_2$ ,  $2323\text{ cm}^{-1}$ ). For particles with composition SW 1 the molecular peaks are observed to remain qualitatively the same down to RH of approximately 50 %, where efflorescence occurs. By contrast, particles with composition SW 2 undergo

a preceding transition at RH of approximately 68 %, where the  $\nu_1\text{-SO}_4$  at  $976\text{ cm}^{-1}$  splits into two peaks at  $976\text{ cm}^{-1}$  and  $1007\text{ cm}^{-1}$ . Every investigated particle with composition SW 2 showed the same behavior. The preceding transition was observed between 65–68 % RH. When adding an amount of 0.12 g / 100 mL of  $\text{CaCl}_2$  to composition SW 1 and repeating the measurement series, the preceding transition occurred, indicating that the origin of this transition is linked to the presence of  $\text{Ca}^{2+}$  ions.

By comparison of the Raman signal of different  $\text{CaSO}_4$  hydrates<sup>137</sup>, the emerging peak centered at  $1007\text{ cm}^{-1}$  can be assigned to crystalline  $\text{CaSO}_4 \cdot 2\text{H}_2\text{O}$  (Gypsum). The residual peak at  $976\text{ cm}^{-1}$  is identified as the remaining  $\text{SO}_4^{2-}$  in the aqueous phase that does not partake in the crystallization reaction (there is a large excess of  $\text{SO}_4^{2-}$  with respect to  $\text{Ca}^{2+}$  ions in the sea salt composition). The crystallization of  $\text{CaSO}_4 \cdot 2\text{H}_2\text{O}$  has a negligible effect on density and mass growth of the particle. The transition is not noticeable in the respective data sets (Fig. 5 and 6). This agrees with the observation that sea salt compositions SW 1 and SW 2 show very similar densities and hygroscopic mass growth factors, implying that ions in lower abundance play a negligible role for these quantities. As such, removal of the  $\text{Ca}^{2+}$  ions and the corresponding amount of  $\text{SO}_4^{2-}$  from the aqueous phase is not expected to have a noticeable impact on either size, mass or density of the particle. An upper estimate of the effect of the phase transition on the density can be obtained by assuming that all  $\text{Ca}^{2+}$  ions take part in the crystallization process. The mass fraction of crystallized  $\text{CaSO}_4 \cdot 2\text{H}_2\text{O}$  with respect to the whole anhydrous salt mass is then approximately 4.5 %. Taking into account the experimentally determined mass growth factor of 3.0 at the transition  $\text{RH} \approx 65\%$  and the density of  $\text{CaSO}_4 \cdot 2\text{H}_2\text{O}$  of approximately  $2300\text{ kg m}^{-3}$ , roughly twice the density of the aqueous solution, the change in particle density upon phase transition can be estimated to be approximately 0.75 %. The change in density during phase transition is therefore lower than our experimental uncertainty.

The efflorescence RH (ERH) of sea salt is reported at approximately 45 %<sup>45,49</sup>. Experimentally, we find our sea salt droplets to go through the main efflorescence phase transition at somewhat larger values at approximately 50 % (see Fig.(6.7)). Regardless of the exact ERH, the  $\text{CaSO}_4 \cdot 2\text{H}_2\text{O}$  crystallization is observed at considerably larger RH. Experimentally, we therefore observe efflorescence in two steps at distinct RH, with the main step being the efflorescence transition at approximately 50 % preceded by the crystallization of  $\text{CaSO}_4 \cdot 2\text{H}_2\text{O}$  at around 65 %. Similar phase transitions of sea salt solutions in multiple steps have previously been studied for droplets on a sub-



strate<sup>138,139</sup>. For samples containing  $\text{Ca}^{2+}$  ions the crystallization of  $\text{CaSO}_4$  hydrates was observed at RH as large as 90%<sup>138</sup>. The presence of a substrate implies the existence of a contact surface for heterogeneous nucleation, which is known to facilitate phase transitions at larger RH<sup>140</sup>, but which is absent for the levitated droplets in this work. Heterogeneous nucleation processes are thought to be suppressed in the absence of a contact surface, and the associated multiple step phase transitions have not been previously reported for levitated particles to the best of our knowledge. Our findings however show that such transitions may occur even for levitated droplets with no apparent contact surface.

We note that the multistep transitions of sea salt droplets discussed here are to be distinguished from similarly denoted processes which describe a single phase transition for which one or several precursor states have been identified<sup>141–143</sup>, or from phase transitions which proceed over one or several intermediate states to the final product as governed by the Ostwald step rule<sup>31,144,145</sup>. Such multistep transitions have been reported for levitated particles and other systems and, while of great interest for fundamental studies of nucleation processes, are beyond the scope of the present work.

## 6.5 Conclusions

We have demonstrated the capabilities of optical trapping for accurate hygroscopic measurements of single aerosol particles, for particles with approximate dry sizes of  $R_{\text{dry}} = 0.3\text{--}2\ \mu\text{m}$ . In particular, our measurements of atmospherically relevant sea salt droplets are numerically in good agreement with earlier measurements by Tang et al.<sup>45</sup> With regard to the reference dry mass used in our study and in the one by Tang et al., we suggest that our values (the ones obtained in this study and by Tang et al.) represent the hygroscopic growth with respect to the anhydrous salt particle. Based on this, we further suggest in accordance with Zieger et al.<sup>49</sup>, who measured approximately 20% lower hygroscopic mass growth factors for micrometer sized particles, that these apparent discrepancies are due to the presence of hydrates in the dried salt particle of Zieger et al. The same reasoning might apply to the measurements on particles in the nanometer size range, where similar discrepancies are observed in the literature, however, this range is outside the scope of this work. It is proposed for future hygroscopic growth studies that the amount of hydrates in the dry sample used for reference is

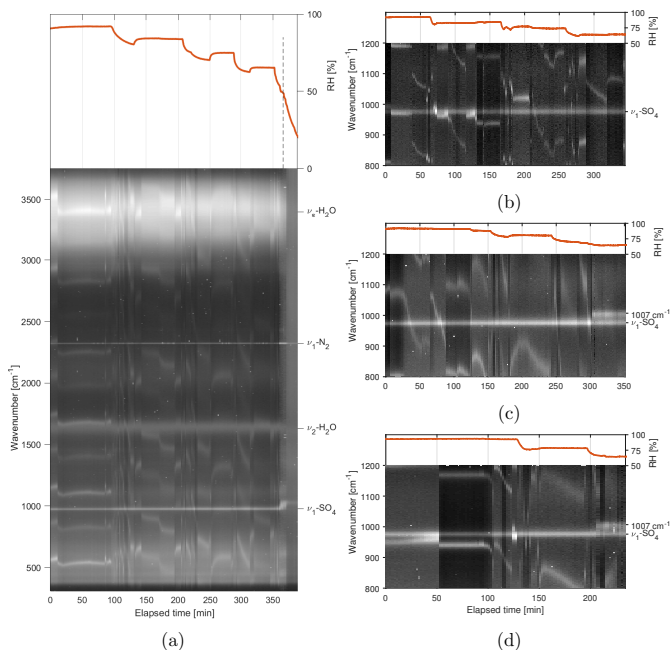


Figure 6.7: Time evolution of the Raman spectrum of drying sea salt droplets. (a) Evolution of whole spectrum for a particle of composition SW 1. The peaks in the Raman spectra are visible as white lines on the dark background. Shifting lines indicate morphology dependent resonances, or whispering gallery modes, shifting with the size of the particle upon changes of the RH (indicated at the top by the red solid line). The molecular Raman peaks are visible as horizontal lines, which do not change position upon changing the RH. The S–O symmetric stretching ( $\nu_1\text{-SO}_4$ ), H–O bending ( $\nu_2\text{-H}_2\text{O}$ ) and symmetric O–H stretching ( $\nu_s\text{-H}_2\text{O}$ , 2700–3750 cm<sup>-1</sup>) modes are indicated as well as the stretching mode of the nitrogen in the gas phase ( $\nu_1\text{-N}_2$ ). At around 380 min, the RH reaches 50 % and efflorescence of the particle is observed (dashed vertical line). (b)–(d) zoom on the region around  $\nu_1\text{-SO}_4$  for three particles with composition (b) SW 1, (c) SW 2 and (d) SW 1 + CaCl<sub>2</sub>. In (b) no qualitative change of the  $\nu_1\text{-SO}_4$  peak is observed, even as the RH drops to 63%. In (c) and (d), when the RH drops below 68 % the  $\nu_1\text{-SO}_4$  peak at 976 cm<sup>-1</sup> splits into two peaks at 976 cm<sup>-1</sup> and 1007 cm<sup>-1</sup> indicating a partial crystallization of the particle.

specified. We expect this information to be crucial to reconcile the data reported in the literature and improve the transferability and reliability of the retrieved values, which in turn will enable more accurate climate modelling. The effect of the potential aging of sea salt droplets<sup>146</sup> on their hygroscopicity, which has not been studied here, could also be studied in the future using the measurement method described here.

Finally, in sea water compositions containing  $\text{Ca}_2^+$  and  $\text{SO}_4^{2-}$ , the crystallization of  $\text{CaSO}_4 \cdot 2\text{H}_2\text{O}$  (Gypsum) was observed at RH of 65–68 %, which is significantly larger than the RH at which the efflorescence of the particle occurred (RH  $\approx$  50 %). This crystallization is typically attributed to heterogeneous nucleation processes that occur when the particle is in contact with a surface, such as a substrate or the surface of a secondary particle. By contrast, we observe the crystallization of  $\text{CaSO}_4 \cdot 2\text{H}_2\text{O}$  in the absence of any apparent contact surface.

## 6.6 Acknowledgements

The authors are very grateful to David Stapfer and Markus Steger from the electronic and the mechanical workshop for technical support. Financial support was provided by the Swiss National Science Foundation (project no. 200020\_200306).

## 6.7 Data availability

Data needed to evaluate the conclusions of the paper are presented in the paper or deposited in the ETH Research Collection doi: 10.3929/ethz-b-000572190. The data collection also includes a table, which provides the measurement data for the NaCl, SW 1 and SW 2 droplets, in particular the obtained values for the sizes, the masses, the densities and the dry masses at specified RHs with their uncertainties. Additional data related to this paper may be requested from the authors.

# 7 Optical trapping and mass measurement in water

## 7.1 Introduction

It is hard to overstate the importance of water in biology. Water constitutes a major part of most living organisms and makes up approximately 50–70 % of the mass of the human body<sup>147</sup>. Most biomolecules, bacteria, viruses and other microscopic biological entities exist naturally only in aqueous solution, and require an aqueous environment for their physiological functions. Water takes an active role in stabilizing proteins and inducing structural changes and is fundamental for protein folding<sup>148–150</sup>. Aqueous environments are therefore of particular interest for the study of biological particles.

In contrast to alternative techniques for trapping of single particles such as the electrodynamic balance (EDB)<sup>65</sup>, optical traps are not limited to trapping in air or vacuum and can be readily applied to a liquid environment as well. This is illustrated by the fact that the first demonstration of the optical trapping principle by Ashkin was performed in water<sup>4</sup>, with the first demonstration of optical trapping in air arriving only afterwards<sup>151</sup>. Optical trapping of biological particles in aqueous solution has been used to measure the viscoelastic properties of human cells<sup>6</sup> and DNA<sup>7</sup>, to observe individual binding events during ATPase reactions<sup>13</sup>, for microrheology of biologically relevant systems<sup>8</sup> and for force sensing of individual motor proteins along microtubules<sup>9</sup> as well as in a large number of other studies<sup>16,17</sup>. Combining these studies with a method of mass measurement *in vivo* could yield complementary data necessary for a thorough characterization of the observed processes. This makes the application of our optical mass measurement technique to the aqueous phase an intriguing perspective.

Here it is shown that the same optical trapping setup that is used to investigate droplets in air (see Chapter 5 and Chapter 6) is suitable for optical trapping of micrometer sized glass spheres in water. We then proceed to apply the mass measurement method explained in Chapter 4 to the liquid phase to determine the mass of the trapped microspheres. It is found that currently, the accuracy of the setup is not sufficient for practical purposes due to the large damping of the particle motion as a consequence of the high viscosity and density of water with respect to air. Based on these results, a value for the accuracy of the particle tracking required for the retrieval of the particle mass is derived and compared to the accuracy achieved with the current setup.

## 7.2 Methods

The optical trapping setup used to trap single microspheres in water is identical to the setup shown in Chapter 6, Fig.(6.1), with the trapping cell replaced with a design that allows for containment and circulation of water, see Fig.(7.1). The cell is filled with purified water (resistivity 18.2 M $\Omega$ s) through an inlet in the cell using a high performance liquid chromatography pump (Hitachi L-6200A) and the monospheres for trapping are introduced thereafter. Once a single particle is trapped, the cell is flushed with water until only the trapped particle remains in the cell.

Sample label	$R$ [ $\mu\text{m}$ ]	$\rho_{\text{part}}$ [ $\text{kg m}^{-3}$ ]	Company/Catalogue no.
SiO <sub>2</sub>	2.49	2000	Bangs Labs./SS05003
BoSiO <sub>2</sub>	$3.95 \pm 0.45$	2550	Thermo Fisher/9008

Table 7.1: Properties of particles used in this study.

The particles used in this study are spherical silica (SiO<sub>2</sub>) and borosilicate (BoSiO<sub>2</sub>) spheres with radii of  $R = 2.5 \mu\text{m}$  and  $R = 4 \mu\text{m}$ , respectively. This size range is representative for larger bacteria, but smaller than typical eukaryotic cells. Table (7.1) lists the relevant properties of the monospheres used in this study.

The measurement of the particle oscillation during trap modulation and subsequent retrieval of the particle mass proceeds as explained in Chapter 4 and Chapter 6. Here the essential steps are recapitulated. Harmonic oscilla-

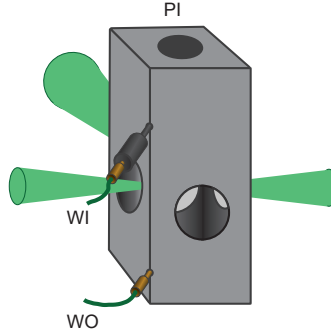


Figure 7.1: Cell design for optical trapping in water. Particles are introduced in the cell via the particle inlet (PI). Once a suitable particle is trapped, water is pumped through the water inlet (WI) to flush the remainder of the particles through the water outlet (WO). The two trapping beams are indicated by the green cones entering the cell via the side windows. The scattering light used for particle tracking is indicated by the green cone at the rear of the cell.

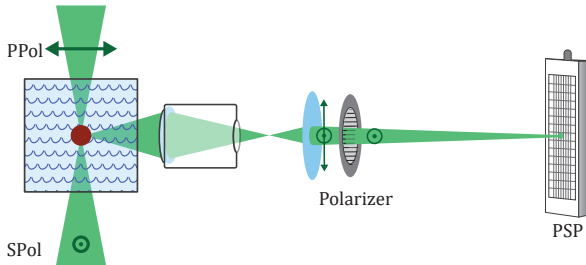


Figure 7.2: Particle position tracking setup. The scattered light is collected under a mean scattering angle of  $90^\circ$  and focused on the position sensing photodiode (PSP). The tracking accuracy is improved using a linear polarizer to suppress the scattered light of the parallel polarized trapping beam (PPol), so that mainly the scattered light of the perpendicular polarized trapping beam (SPOL) is recorded.

tion of the particle along the trapping beam axis is induced by modulating the relative power of the two trapping beams. The particle position during modulation is tracked using a position sensing photodiode (PSP, Thorlabs PDP90A) as shown in Fig.(7.2). Oscillation amplitude  $A$  and phase  $\varphi$  with respect to the trap modulation are measured as function of modulation frequency  $f$  by recording the PSP signal and the modulation signal using a lock-in amplifier (Zurich instruments MFLI 500kHz). The resulting amplitude and phase are described using a harmonic oscillator model:

$$A(f) = Z_0 \frac{\Omega_0^2}{\left( \left( \Omega_0^2 - (1 + \Gamma_2)f^2 - \Gamma_1 f^{\frac{3}{2}} \right)^2 + \left( \Gamma_0 f + \Gamma_1 f^{\frac{3}{2}} \right)^2 \right)^{\frac{1}{2}}} \quad (7.1)$$

$$\varphi(f) = \arctan \left( \frac{\Gamma_0 f + \Gamma_1 f^{\frac{3}{2}}}{\Omega_0^2 - (1 + \Gamma_2)f^2 - \Gamma_1 f^{\frac{3}{2}}} \right) \quad (7.2)$$

where the modulation amplitude  $Z_0$ , the eigenfrequency  $\Omega_0$  and the damping rate  $\Gamma_0$  are free parameters of the model and

$$\begin{aligned} \Gamma_1 &= \Gamma_0 \cdot R \cdot \left( \pi \frac{\rho_{\text{H}_2\text{O}}}{\mu_{\text{H}_2\text{O}}} \right)^{\frac{1}{2}} \\ \Gamma_2 &= \frac{2}{9} \Gamma_0 \cdot R^2 \cdot \pi \frac{\rho_{\text{H}_2\text{O}}}{\mu_{\text{H}_2\text{O}}} \end{aligned} \quad (7.3)$$

are the correction terms to  $\Gamma_0$  with  $R$  the radius of the particle and  $\rho_{\text{H}_2\text{O}}$  the density and  $\mu_{\text{H}_2\text{O}}$  the viscosity of water. Note that in Eq.(7.1) the absolute length scale is secondary, and that for later discussions,  $A(f)$  is given by the measured voltage value of the oscillation amplitude relative to the modulation signal amplitude,  $A \rightarrow \frac{A}{S_0}$ . See Chapter 4, Eq.(4.2) for the definition of  $S_0$ . Parameters  $\Omega_0$  and  $\Gamma_0$  depend on the optical trap stiffness  $k$ , the laminar drag coefficient  $\gamma = 6\pi\mu_{\text{H}_2\text{O}}R$  and the particle mass  $m$  as follows:

$$\begin{aligned} \Omega_0 &= \frac{1}{2\pi} \left( \frac{k}{m} \right)^{\frac{1}{2}} \\ \Gamma_0 &= \frac{1}{2\pi} \frac{\gamma}{m} \end{aligned} \quad (7.4)$$

From the known properties of the  $\text{SiO}_2$  and  $\text{BoSiO}_2$  particles, see Table (7.1),

the damping rates are predicted to be

$$\begin{aligned}
 \text{SiO}_2 : \quad \Gamma_0^{\text{theo}} &= \frac{9\mu_{\text{H}_2\text{O}}}{4\pi R^2 \rho_{\text{part}}} = 54\,000 \text{ Hz} \\
 \text{BoSiO}_2 : \quad \Gamma_0^{\text{theo}} &= \frac{9\mu_{\text{H}_2\text{O}}}{4\pi R^2 \rho_{\text{part}}} = 17\,000 \text{ Hz}
 \end{aligned}
 \tag{7.5}$$

### 7.3 Results and discussion

Oscillation amplitude and phase of a representative BoSiO<sub>2</sub> particle are shown in Fig.(7.3) as function of modulation frequency. The phase is observed to reach 90° at frequencies of approximately  $f_{90} = 20$  Hz, which is much lower than typical values obtained from particles in the gas phase, which range around 1000 Hz (see for example Chapter 5). From the amplitude data it is further evident that the oscillation decays rapidly with increasing frequency and already at  $f_{90} = 20$  Hz, the signal amplitude  $A$  has reached a value that is approximately half the modulation signal amplitude  $S_0$ . For comparison, in the gas phase, the oscillation signal amplitude decreases to the value of the modulation signal amplitude only at frequencies of several kHz (Fig.(4.6)). The low oscillation amplitude limits the accuracy of the phase fitting due to the lower signal-to-noise ratio and the presence of measurement artifacts that are otherwise not relevant at higher signal amplitudes. This is evident from the best fit of the presented data, which yields a value for the damping rate,  $\Gamma_0 = 750$  Hz, that is more than an order of magnitude below the theoretical value of  $\Gamma_0^{\text{theo}} = 17\,000$  Hz. Before these artifacts and the associated measurement uncertainties are discussed in greater detail, we identify the main reasons for the comparatively low values of  $A$  and  $f_{90}$  for the oscillation in water.

An indicator for the damping of the oscillation with increasing frequency is the damping ratio  $\zeta = \frac{\Gamma_0}{2\Omega_0} = \frac{\gamma}{2} \cdot (mk)^{-\frac{1}{2}}$ . Since  $\gamma$  and therefore also  $\Gamma_0$  are proportional to the viscosity of the surrounding medium, the damping ratio is approximately 50 times larger in water than in air due to the larger viscosity of water. In addition, the optical force on the particle, and hence the trapping stiffness  $k$ , is generally smaller in water than for the same particle trapped in air. The optical force scales with the optical contrast between particle and surrounding, which for BoSiO<sub>2</sub> in water is only  $\frac{n_{\text{BoSiO}_2}}{n_{\text{H}_2\text{O}}} = 1.17$ . The same BoSiO<sub>2</sub> particle trapped in air would have an optical contrast of  $\frac{n_{\text{BoSiO}_2}}{n_{\text{air}}} \approx n_{\text{BoSiO}_2} = 1.56$ . The optical force is further reduced due to the



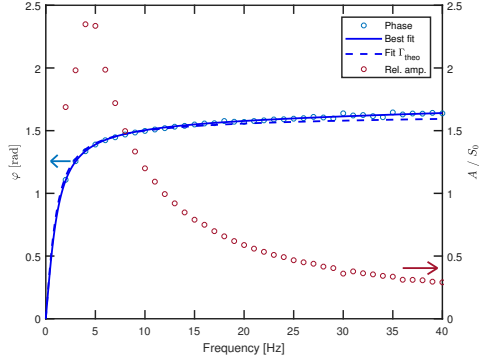


Figure 7.3: Oscillation phase and amplitude of a  $\text{BoSiO}_2$  particle in water as function of modulation frequency. The amplitude signal is given relative to the modulation signal amplitude of  $S_0 = 120 \text{ mV}$ . The best fit of the phase data is indicated with a solid line and corresponds to  $\Omega_0 = 28 \text{ Hz}$  and  $\Gamma_0 = 750 \text{ Hz}$ . The fit using the theoretical  $\Gamma_0^{\text{theo}} = 17000 \text{ Hz}$  and the fitted  $\Omega_0(\Gamma_0^{\text{theo}}) = 128 \text{ Hz}$  is indicated by the dashed line. At low frequencies, the oscillation amplitude exceeds the size of the PSP sensor area, which results in the apparent initial increase of the amplitude values with increasing frequency.

distortion of the trapping beams at the interface between air and water at the cell windows, which leads to a defocusing of the trapping beams and decrease in light intensity at the position of the particle.

The smaller value of  $\Omega_0$  also explains the smaller value for the observed  $f_{90}$  in water. The value of  $f_{90}$  is reduced with respect to  $\Omega_0$  by the inertia of the fluid that is accelerated as part of the particle oscillation. This effect can be understood by comparing the value of  $f_{90}$  with  $\Omega_0$ . In the gas phase, where the density and therefore the inertia of the fluid is small, it was found in Chapter 4 that  $\Omega_0 \approx f_{90}$  (see for example Fig.(4.3) and compare  $\Omega_0$  with  $f_{90}$  in the extended model, where the value of  $f_{90}$  is the same than  $\Omega_0$  in the simple model). For the aqueous phase on the other hand we find with

$f_{90} = 20 \text{ Hz}$  and Eq.(7.2)

$$\begin{aligned} \varphi(f_{90}) &= \frac{\pi}{2} \\ \Omega_0^2 - (1 + \Gamma_2^{\text{theo}})f_{90}^2 - \Gamma_1^{\text{theo}}f_{90}^{\frac{3}{2}} &= 0 \\ \Omega_0 &= \underbrace{\left(1 + \Gamma_2^{\text{theo}} + \Gamma_1^{\text{theo}}f_{90}^{-\frac{1}{2}}\right)^{\frac{1}{2}}}_{=7.1} f_{90} \end{aligned} \quad (7.6)$$

where  $\Gamma_1^{\text{theo}}$  and  $\Gamma_2^{\text{theo}}$  are given by Eq.(7.3) and the theoretical value for  $\text{BoSiO}_2$   $\Gamma_0^{\text{theo}}$  given by Eq.(7.5). In other words, at the frequency  $f_{90}$  the effective mass of the oscillator is more than 7 times larger than the particle mass due to the interaction of the particle with the surrounding water. The larger effective mass leads to larger values of  $\varphi$  at low modulation frequencies in comparison to typical values observed for a particle trapped in air.

It was explained in Chapter 4 that the ratio  $\frac{A}{S_0}$  is an indicator for the significance of artifacts in the position measurement of the particle during modulation. One of these artifacts, termed the “focus artifact”, arises from the finite size of the particle image on the PSP. The particle image on the PSP is a superposition of the scattered light of the two trapping beams. Since the light scattering pattern is not symmetric with respect to the scattering angle, and the particle image has a non-negligible spatial extension even for the best achievable focus, the centroid positions of the two particle images do not exactly coincide. Here the centroid position denotes the intensity weighted average position of the respective image on the PSP. As the relative intensity of the two particle images oscillates during trap modulation, the spatial separation of the two centroid positions induces an artificial oscillation signal in phase with the trap modulation. The focus artifact can be characterized as shown in Chapter 5 by repeating the phase measurements for different foci of the particle image on the PSP. Since a larger image results in a larger separation of the two centroid positions, a focus dependence of the measured phase is expected if this artifact is relevant.

Fig.(7.4) shows the fitted value of  $\Gamma_0$  for a series of frequency sweeps at different foci. Although a small trend may be identified towards lower fit values when going from negative to positive focus positions, the difference between the individual measurements is not significant with respect to the indicated fit uncertainties. It is therefore concluded that the focus artifact is not limiting the current accuracy of the setup. In our setup, the focus artifact is suppressed by using cross-polarized trapping beams and filtering out the

scattered light of the parallel polarization component with a linear polarizer, effectively removing one of the two particle images (Fig.(7.2)). These results therefore show that this setup is effective in removing the focus artifact even in the case of small values of  $\frac{A_s}{S_0}$ . At the same time, the best fit values of  $\Gamma_0$  are approximately one order of magnitude below the theoretical expectations of  $\Gamma_0^{\text{theo}} = 17\,000\text{ Hz}$ , which indicates to other artifacts.

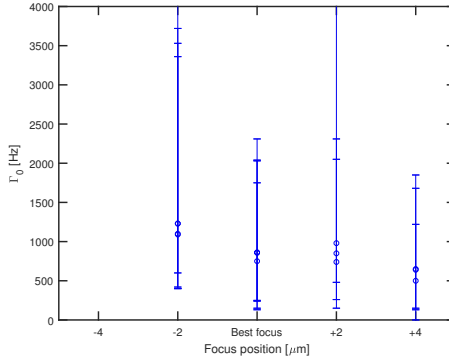


Figure 7.4: Fitted damping rates at different foci. The focus is indicated by the distance between particle and the light collection and focusing optics before the PSP. The displayed interval represents the range for which a tight focus is observed upon visual examination. Two fit values have a significantly larger uncertainty than the rest of the measurements, which indicates that the trapping stability may have been temporarily compromised during the corresponding phase measurements. For these values only part of the errorbar is displayed.

Systematic biases of the PSP and the readout electronics may become significant for low measurement signals. Here we present an empirical treatment of the overall effect of these artifacts by introducing a bias factor  $\alpha \approx 1$  that perturbs the position measurement according to

$$z'(t) = z(t) \cdot \alpha(z(t), I(t)) \quad (7.7)$$

where  $z(t)$  is the true position signal in time,  $z'(t)$  the measured position signal and  $\alpha(z, I)$  the artifact, for which a dependence on the position signal  $z$  and total intensity signal  $I$  of the PSP is assumed. The true position and

intensity signals follow approximately a sinusoidal time dependence,

$$\begin{aligned} z(t) &= \bar{z} + \Delta z = \bar{z}(t) + A_z \sin(2\pi f - \varphi_z) \\ I(t) &= \bar{I} + \Delta I = \bar{I}(t) + A_I \sin(2\pi f) \end{aligned} \quad (7.8)$$

where the quantities with bar represent time averaged values.  $A_z$  and  $A_I$  are the amplitude of position and intensity oscillation with frequency  $f$ , respectively, and  $\varphi_z$  is the phase of the oscillation with respect to the trap modulation. The intensity oscillation is approximately in phase with the trap modulation ( $\varphi_I = 0$ ). Using this, the first order effect of  $\alpha$  on the measurement is

$$\alpha(z, I) = \alpha(\bar{z}, \bar{I}) + \alpha'_z \cdot \Delta z + \alpha'_I \cdot \Delta I \quad (7.9)$$

where  $\alpha'_z$  and  $\alpha'_I$  are the first order coefficient of the Taylor expansion in  $z$  and  $I$ , respectively. Inserting this into Eq.(7.7) and using Eq.(7.8) results in

$$\begin{aligned} z' &= (\bar{z} + \Delta z) \cdot (\alpha(\bar{z}, \bar{I}) + \alpha'_z \cdot \Delta z + \alpha'_I \cdot \Delta I) \\ &= (\alpha(\bar{z}, \bar{I}) + \bar{z} \cdot \alpha'_z) \cdot \Delta z + \bar{z} \cdot \alpha'_I \cdot \Delta I + T_{0,2f} \end{aligned} \quad (7.10)$$

where  $T_{0,2f} = \bar{z} \cdot \alpha(\bar{z}, \bar{I}) + \alpha'_z \cdot \Delta z^2 + \alpha'_I \cdot \Delta z \cdot \Delta I$  denotes terms that do not oscillate at frequency  $f$  and therefore are irrelevant for the determination of the oscillation phase via lock-in detection. Eq.(7.10) allows one to extract essential trends. The average bias  $\alpha(\bar{z}, \bar{I})$  and the dependence of the artifact on  $z$ , indicated by  $\alpha'_z$ , only apply a scaling factor to the oscillatory part,  $\Delta z$ , and therefore do not change the result of the phase measurement. The phase measurement is only perturbed by the term  $\bar{z} \cdot \alpha'_I \cdot \Delta I$ , which depends on the average particle position  $\bar{z}$ . More precisely, since the phase of  $\Delta I$  is  $\varphi_I = 0$ , positive values of the prefactor  $\bar{z} \cdot \alpha'_z$  will shift the phase measurement towards  $\varphi = 0$ , whereas negative values will shift it towards  $\varphi = 180^\circ$ .

These considerations yield a comprehensible picture, in which one can use the dependence of the phase measurement on the average particle image position  $\bar{z}$  to assess the systematic bias in the signal of the PSP and read-out electronics. This artifact is termed ‘‘position artifact’’. Fig.(7.5) shows the measured oscillation phase of a  $\text{SiO}_2$  particle in water for different average image positions on the PSP. Note that the true average image position  $\bar{z}$  cannot be directly measured, and the average value of  $\bar{z}' = \bar{z} \cdot \bar{\alpha}$  is indicated as approximation instead. The position artifact is particularly apparent in the case of  $\text{SiO}_2$  particles, since the damping rate and therefore the damping ratio are much larger than for  $\text{BoSiO}_2$ , leading to a smaller oscillation amplitude

signal. Towards lower values of  $\bar{z}'$ , the phase is observed to decrease above approximately  $f = 5$  Hz. This trend is contrary to the model behavior, which illustrates that the artifact becomes dominant over the actual measurement signal. This illustrates that this data is not suited for determination of  $\Gamma_0$ , which is necessary for the retrieval of the particle mass, due to the limited accuracy of the particle tracking.

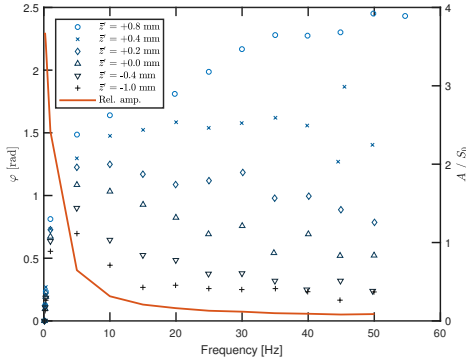


Figure 7.5: Phase measurements for different average particle image positions on the PSP. The value of  $\bar{z}'$  indicates the measured average position signal of the PSP during the respective phase measurements. The value  $\bar{z}' = 0$  mm corresponds approximately to the center of the PSP. The relative amplitude for  $\bar{z}' = 0$  mm indicated by the solid line is representative for all values of  $\bar{z}'$ .

Which accuracy of the phase measurement is required to yield reliable mass data with adequate levels of uncertainty? To answer this question, we turn again to  $\text{BoSiO}_2$  particles with radius  $R = 4 \mu\text{m}$ ,  $\Gamma_0 = 17\,000$  Hz, and typical  $\Omega_0 = 120$  Hz (see Fig.(7.3)). The minimum requirement that is imposed here is that the phase data can be fitted with reasonable accuracy if a noise level is assumed that corresponds to the level of the best observations in the gas phase. Typical noise levels in the gas phase are given in Chapter 4, Fig.(4.8). Here a standard deviation of 0.006 rad is assumed. Fig.(7.6) shows the fitting of the simulated phase data starting from  $f = 0$  over different frequency ranges indicated by the cut-off frequency  $f_{\text{cut}}$ . Larger  $f_{\text{cut}}$  are necessary for more accurate fit values, which requires that the position artifact must not be relevant even for smaller  $\frac{A}{S_0}$ . From the data in Fig.(7.6b) it is evident that a cut-off frequency of  $f_{\text{cut}} = 1000$  Hz is necessary to determine  $\Gamma_0$  with a modest uncertainty of 30%. At this frequency, a value of  $\frac{A}{S_0} \approx 10^{-4}$  is

predicted. This value should be compared with the data shown in Fig.(7.5), where the position artifact is significant already at ratios  $\frac{A}{S_0} \approx 2$ . Although a subsequent improvement of the particle tracking setup with only minor modifications showed that the position artifact can be suppressed for all ratios  $\frac{A}{S_0} > 1$  (see discussion in Chapter 4), far better accuracy is needed still for accurate mass retrieval for particles trapped in water.

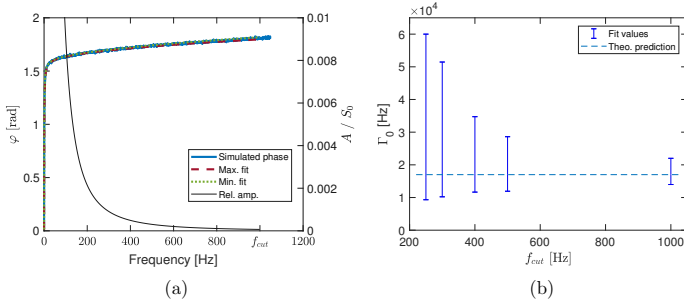


Figure 7.6: Fit accuracies of simulated data. (a) Simulated amplitude and phase data with fit range 0–1000 Hz for the phase measurements. The fits corresponding to the maximum and minimum values of fitparameters  $\Omega_0$  and  $\Gamma_0$  are indicated by the dashed and dotted line, respectively. The relative amplitude is shown as solid black line. (b) Fit uncertainty for  $\Gamma_0$  as function of cut-off frequency. The theoretical prediction is shown as dashed line.

## 7.4 Conclusions

The applicability of our optical trap to the liquid phase has been demonstrated by trapping single microspheres in water. While harmonic oscillation of the trapped particle has been successfully induced as a prerequisite for single particle mass measurement in water, the current accuracy of the particle tracking is insufficient for accurate mass retrieval. This is in major part a consequence of the larger damping of the particle oscillation in the aqueous phase with respect to air, which leads to a smaller oscillation signal. Among the artifacts that emerge for low measurement signals, the position artifact is currently the limiting factor of the measurement accuracy. Since this artifact arises from biases in the PSP and the read-out electronics, significant improvement in the accuracy is only expected by upgrading the measurement

hardware, in particular, the PSP itself. However, an additional suppression of the position artifact of about 3 to 4 orders of magnitudes would be required for the application of this particle mass measurement technique in the liquid phase. At the moment, such an improvement appears not feasible.

## 8 Photo-induced shrinking of aqueous glycine aerosol droplets

This chapter is a copy of a submitted manuscript:

**Title** Photo-induced shrinking of aqueous glycine aerosol droplets  
**Authors** Shimosuke Ishizuka<sup>a,b,c</sup>, Oliver Reich<sup>c</sup>, Grégory David<sup>c</sup>  
and Ruth Signorell<sup>c</sup>  
**Original article** Atmos. Chem. Phys. Discuss. [preprint]  
<https://doi.org/10.5194/acp-2023-6> (2023)  
**License** Creative Commons Attributions v4.0 International (CC-BY)  
<http://creativecommons.org/licenses/by/4.0/>

<sup>a</sup> Department of Chemistry and Applied Biosciences, ETH Zurich, Vladimir-Prelog-Weg 2, CH-8093, Zurich, Switzerland

<sup>b</sup> Institute of Advanced Research, Nagoya University, Nagoya 046-8601, Japan

<sup>c</sup> Institute of Space-Earth Environmental Research, Nagoya University, Nagoya 046-8601, Japan

The style of the text and the style, size and placement of the figures and tables have been adapted, as have the numbering of figures, tables and sections.

Author contribution of O.R.: O.R. contributed to the measurement and analysis of the data and wrote the main part of the manuscript.



## Abstract

Due to their small size, micrometer and submicron sized solution droplets can respond differently to physical and chemical processes compared with extended bulk material. Using optically trapped micrometer sized aqueous glycine droplets, we demonstrate photo-induced degradation of glycine upon irradiation with visible light, even though molecular glycine does not absorb light in the near UV/vis range to any significant extent. This reaction is observed as photo-induced shrinking of the droplet, which we characterize by analyzing the elastic light scattering and the Raman spectrum of the droplet over the course of the reaction. We find the volume to shrink with a constant rate over the major part of the shrinking process. This indicates the presence of a rate limiting photocatalyst, which we attribute to mesoscopic glycine clusters in the droplet solution. Our findings relate to previous reports of visible light absorption by photosensitizers. However, to the best of our knowledge, this is the first experimental evidence of a photochemical pathway facilitated by mesoscopic clusters. Light interaction with such mesoscopic photoactive molecular aggregates might be more important for aerosol photochemistry than previously anticipated.

## 8.1 Introduction

Aerosols, dispersions of solid and liquid particles in a gas, are ubiquitous in Earth's atmosphere and as such play an important role for many atmospheric processes<sup>1,2</sup>. Size, chemical composition, viscosity and thermodynamic phase of aerosol particles respond to their environment including the surrounding gas species, temperature, humidity<sup>45,49,114,152</sup> and light irradiation<sup>2,26,153,154</sup>. Particular attention has been paid to their chemistry distinct from that in the bulk, a phenomenon possibly arising from high surface to volume ratio of aerosol particles and the accessibility to highly supersaturated states<sup>155-157</sup>. Various chemical reactions have been shown to be accelerated in microdroplets<sup>26,158,159</sup>, with some reactions being exclusive to the droplet phase<sup>160</sup>. These unique reactors can act as medium for the birth, growth and degradation of atmospherically relevant particles<sup>161</sup>, and be utilized for organic synthesis<sup>162</sup>. Chemical processes in prebiotic aerosols have also been proposed as potential mechanisms for the origin of life<sup>163</sup>. However, molecular processes leading to the anomalous chemistry in micrometer and submicron aerosol particles are still largely unknown. Although some processes may be ascribed to the discontinuous and asymmetric intermolecular interactions at the particle surface<sup>161</sup>, the microphysical origins behind many of the aforementioned particle specific phenomena are still not adequately explored.

Glycine is an amino acid that acts as precursor to proteins and fulfills a number of other biological functions<sup>164-166</sup>. With its small size and simple structure, glycine often serves as a proxy for other amino acids and physiologically relevant molecules, and as such has been studied extensively in the past. It is generally accepted that molecular glycine does not absorb light in the near UV/vis range, similar to other amino acids<sup>167</sup>. However, it has been shown that their optical properties change when glycine molecules arrange themselves into mesoscopic clusters<sup>168</sup>. Furthermore, these formations respond to light irradiation in non-trivial ways which can be exploited to induce long range order inside the glycine solution<sup>169-172</sup> on a scale of up to millimeters<sup>173</sup>. While these interactions have the potential to change the optical properties of glycine ensembles significantly and to enable new photochemical reaction pathways, there has been little experimental evidence for such reactions so far.

In this work, we study the response of aqueous glycine droplets to irradiation by visible light. We observe the shrinking of optically trapped micrometer

sized glycine droplets, which can be unambiguously attributed to the exposure to the trapping laser with wavelength 532 nm. To the best of our knowledge, this interaction has not been reported before. We characterize it here with particular focus on the shrinking rate and its dependence on the light intensity. To explain our results, we discuss possible reaction schemes based on the available experimental data. Although further data is needed to elucidate the exact photochemical pathways of the observed reaction, these findings demonstrate the existence of a photochemical reaction for molecules which previously have been considered photochemically inert at visible wavelengths.

## 8.2 Methods

Dual beam optical traps are widely used to confine and isolate single particles<sup>31,42,60,105,174</sup>. The counter-propagating tweezers (CPT) setup for trapping aqueous glycine droplets is shown in Fig.(8.1) and consists of a continuous green laser beam (Novanta Photonics Opus 532 6W), which is expanded and then split into two beams of equal power. These two beams are aligned counter-propagating on a single axis and focused into the trapping cell, where a single droplet is trapped between the two focii.

The droplets are generated from 1.0 M or 2.0 M aqueous solutions of glycine (purity  $\geq 99\%$ , Sigma-Aldrich G7126) using a commercial atomizer (TSI 3076) with pressurized, humidified nitrogen gas (purity 5.0). A system of copper tubings directs the spray of particles into the trapping cell, where the droplets agglomerate at the designated trapping position. The humidification of the nitrogen flow is necessary to ensure that the droplets reach the trapping position in the liquid state. The trapping cell is filled with nitrogen gas (purity 5.0) and a steady nitrogen flow formed by combining wet and dry nitrogen with adjustable flow ratios is used to control the relative humidity (RH) in the cell. For the experiments reported here, the RH is set at  $77 \pm 3\%$  well above the efflorescence RH of glycine at approximately  $55\%$ <sup>120</sup>. At this RH, the droplet solution is supersaturated with an estimated glycine concentration of  $60\%$  in mass<sup>120</sup>, corresponding to approximately 5 M. Temperature and RH inside the trapping cell are monitored by a sensor (Sensirion SHT35) placed a few millimeters away from the trapping position. When the agglomerated particle reaches a size of approximately  $2\text{--}3\mu\text{m}$  in radius, the remainder of the droplets in the cell are flushed out

with nitrogen for 20–30 min to ensure that only the trapped droplet remains in the cell. After flushing, the power of the trapping laser is kept constant until the end of the measurement.

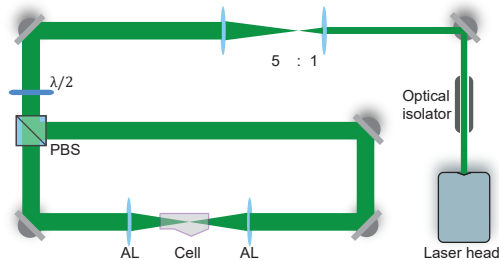


Figure 8.1: Counter-propagating tweezers setup. The laser beam is first expanded by a factor of 5 and then split into two beams by the polarizing beam splitter (PBS). The half-waveplate ( $\lambda/2$ ) rotates the polarization at  $45^\circ$  to the axes of the PBS to ensure equal power splitting between the two beams. The beams are aligned on a single axis and focused into the trapping cell using two aspherical lenses (AL). An optical isolator introduced at the start of the beam path prevents unwanted optical feedback into the laser head.

The particle shrinking is monitored by imaging the polarization resolved two-dimensional angular optical scattering (polarization resolved TAOS) of the particle<sup>175</sup>, as shown in Fig.(8.2). The TAOS image is obtained by collecting the elastically scattered light of the trapping beams under a scattering angle of  $90 \pm 24^\circ$  with an objective (Mitutoyo 20x NA 0.42). The parallel and perpendicular polarization components with respect to the scattering plane (TAOS PPol and TAOS SPol) are separated using a polarization beam splitter and recorded with separate CMOS cameras (Thorlabs DCC1545M). The scattering intensity for each polarization is calculated from the average of the respective TAOS image and recorded over time. At specific times, the shrinking spherical particle reaches a size at which it is in resonance with the light of the trapping beams, which corresponds to a Mie resonance<sup>50</sup>. From the comparison of the recorded evolution of the polarization resolved scattering intensity to simulations using Mie theory, the size of the particle can be determined at the specific times. Fig.(8.3) shows an example of such a TAOS analysis. The values of the size at the discrete points in time, obtained from the times where the particles experience a Mie resonance, can then be interpolated with high accuracy to obtain the full size evolution of the particle over the course of the measurement.

The molecular composition of the particle is monitored by continuous recording of Raman spectra<sup>30</sup> during the shrinking process. To this end, the light scattered by the particle is collected under a scattering angle of  $90 \pm 24^\circ$  by a second objective and fiber coupled into a low noise, high sensitivity spectrograph (Andor KY-328i-A). The inelastically scattered light is analyzed in the range 540–680 nm which corresponds to Raman shifts of 270–4100  $\text{cm}^{-1}$ . This range contains in particular the O–H symmetric stretching mode of water ( $\nu_s\text{-H}_2\text{O}$ , 2700–3750  $\text{cm}^{-1}$ ) as well as several vibrational modes of glycine, which we exploit for the characterization of the molecular composition (see later data for an example).

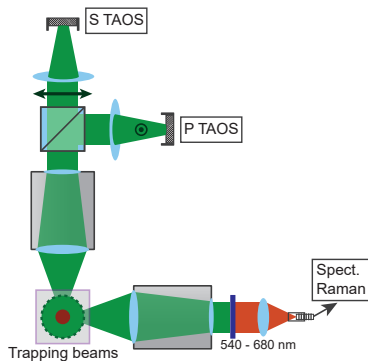


Figure 8.2: Setup for two-dimensional angular optical scattering spectrum (TAOS) imaging and Raman spectroscopy. The trapping beams run perpendicular to the figure plane. The elastically scattered light of the trapping beams is collected horizontally and vertically at a scattering angle of  $90 \pm 24^\circ$ . The vertical beam is split into parallel and perpendicular polarized light with respect to the scattering plane and the respective beam is loosely focused on a CMOS camera (P TAOS and S TAOS respectively). The horizontal beam is filtered for the spectral range of 540–680 nm and fiber coupled into a low noise, high sensitivity spectrometer (Spect. Raman) for measurement of the Raman spectrum.

### 8.3 Results and discussion

The shrinking of the aqueous glycine droplets over time is shown in Fig.(8.4) for three representative examples. The droplets are trapped using different

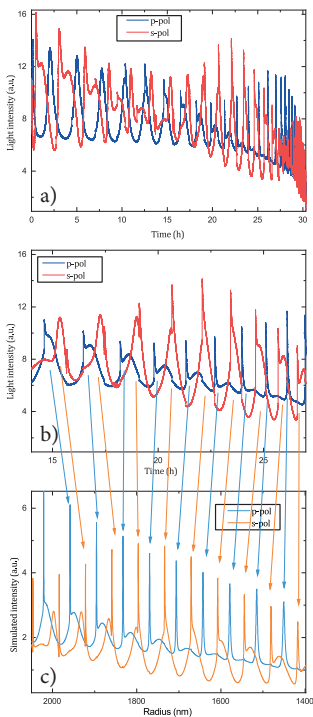


Figure 8.3: Analysis of the light scattering intensity. (a) Experimental polarization resolved scattering intensity over time. (b) Zoom on a specific time interval for clarity (c) Simulated polarization resolved scattering intensity as function of particle radius in the specific time interval. Arrows indicate the peak assignment based on the similarities between the peak shapes.

laser powers, which affects the rate at which their volume is decreasing. For all laser powers, the volume is observed to shrink linearly with time over a large portion of the shrinking process. After a certain point ('point of acceleration'), when the droplet has lost 60–80% of its volume, the shrinking suddenly accelerates, only to continue again approximately linearly with time, albeit at a higher rate.

To quantify the dependence of the shrinking rate on the light intensity incident on the particle, a linear fit is performed on the data before and after the point of acceleration. Since between different experiments, the alignment of the optical trap, and hence the focusing of the laser light on the particle, is subject to temporal mechanical drifts, the nominal laser power used for trapping of the droplets is not an optimal indicator for the incident intensity. Instead, we use the intensity of the scattered light as a measure that is proportional to the incident light intensity. The intensity of the scattered light is obtained from the average signal of the TAOS PPol and SPol images during the time of the droplet shrinking. To ensure consistency between the different experiments, the average of the light intensity is taken over the same volume interval of  $[65.4, 51.0] \mu\text{m}^3$  (radius  $[2.5, 2.3] \mu\text{m}$ ) for all droplets. This interval corresponds to the interval for which we obtained data for most droplets. Fig.(8.5) shows the resulting initial shrinking rates as function of light intensity. The shrinking rate is observed to be proportional to the light intensity, confirming that the shrinking is induced by the trapping laser at a wavelength of 532 nm.

To gain further insight into the shrinking mechanism, we analyze the evolution of the Raman spectra over the course of the shrinking process. A representative example of such an evolution is shown in Fig.(8.6). For Raman spectra of single spherical particles, so called morphology dependent resonances, or whispering gallery modes (WGMs)<sup>58</sup>, are superimposed on the molecular signals. To separate the WGMs from the molecular signal of interest, the Raman spectra are normalized and stacked in chronological order from left to right, as shown in Fig.(8.6a). The WGMs show up as a manifold of thin slanted lines bending towards lower wavenumbers with increasing time as the droplet shrinks. Molecular band positions on the other hand are independent of particle size, and are identified as horizontal lines in the evolution of the Raman spectra.

From Fig.(8.6a) it is evident that the molecular Raman signal remains qualitatively the same, indicating that no significant change in the molecular composition takes place in the droplet over the course of the shrinking process.

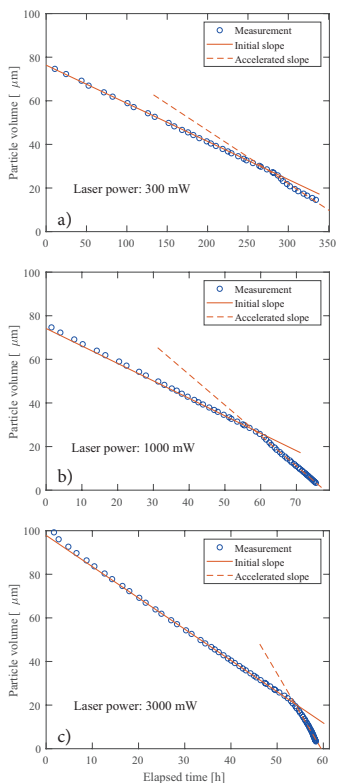


Figure 8.4: Volume shrinking of glycine droplets as a function of time. (a) Droplet trapped at 300 mW nominal laser power (b) droplet trapped at 1000 mW nominal laser power (c) droplet trapped at 3000 mW nominal laser power. At higher power, the shrinking proceeds faster (visible by the larger slopes). Solid and dashed lines indicate the best linear fit before and after the acceleration of the shrinking observed at approximately (a) 280 h, (b) 59 h and (c) 53 h.



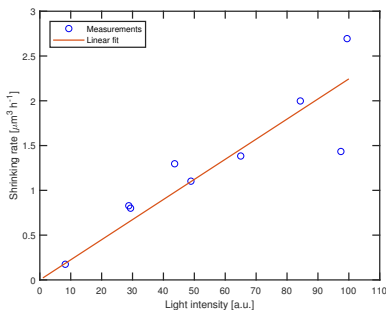


Figure 8.5: Fitted shrinking rate as function of scattered light intensity. The solid line indicates the best linear fit through the origin.

This behavior is observed for all investigated droplets. Since the particle loses the major part of its volume during the shrinking, this implies that glycine is removed from the droplet as a consequence of chemical reaction (vide infra). As the water vapor pressure of the droplet is given by the surrounding RH of 77% and therefore has to remain constant, the removal of glycine from the droplet must be accompanied by the evaporation of water in order to maintain the equilibrium glycine concentration. A quantitative analysis of the Raman spectrum (Fig.(8.6b)) reveals that the spectral intensity of glycine modes with respect to the O–H stretching mode of water remains constant, confirming a constant concentration of glycine molecules during the shrinking process. The measurement ends when the particle becomes too small for stable trapping, and therefore leaves the optical trap.

The linear dependence of the shrinking rate on the light intensity (Fig.(8.5)) proves that the observed shrinking is induced by the laser light. This observation is intriguing as aqueous glycine is not known to absorb light in the visible range, similar to other amino acids<sup>167</sup>. Furthermore, the linear dependence between shrinking rate and light intensity rules out the possibility of multiphoton absorption, which might otherwise populate energetically excited states of glycine to induce chemical reactions.

The observation of a constant shrinking rate over a large portion of the experiments (Fig.(8.4)) provides another important piece of information, as this allows to rule out some of the possible reaction mechanisms. For instance, assuming some residual absorption of light at 532 nm by the droplet solution,

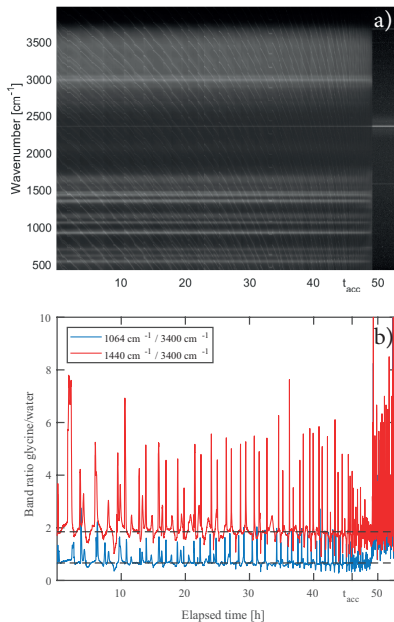


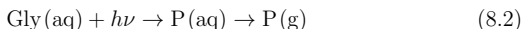
Figure 8.6: Temporal evolution of Raman signal during droplet shrinking. (a) Normalized Raman spectra stacked chronologically from left to right. The molecular Raman bands are visible as horizontal straight white lines on the dark background. The finer, slanted and curved lines correspond to whispering gallery modes. After approximately 49 h, the particle leaves the optical trap as it reaches a size that is too small for trapping, and only background is recorded. The band remaining afterwards at  $2323\text{ cm}^{-1}$  corresponds to the nitrogen gas in the trapping cell. (b) Ratio of the molecular glycine bands centered at  $1064\text{ cm}^{-1}$  and  $1440\text{ cm}^{-1}$  to the water band at around  $3400\text{ cm}^{-1}$ . Peaks and dips in the graphs correspond to spectra where a whispering gallery mode is superimposed on the glycine signal and the water signal, respectively, and are not relevant for the molecular composition. The dashed horizontal lines are a guide to the eye. In this example, the acceleration of the droplet shrinking is observed at  $t_{\text{acc}} = 46\text{ h}$ . From this point in time onwards until the particle is lost, the faster shrinking leads to more frequent WGMs perceived as an apparent increase of noise in the data.

one might argue that the shrinking is a consequence of enhanced evaporation due to the droplet heating by the laser. The evaporation of glycine from the droplet can be approximated by the Hertz-Knudsen equation:

$$\frac{dN}{dt} = S \cdot \frac{\alpha p}{\sqrt{2\pi MRT}} \quad (8.1)$$

where  $\frac{dN}{dt}$  is the molar evaporation rate of glycine,  $S$  is the droplet's surface,  $p$  is the partial pressure and  $M$  is the molar mass of glycine,  $R$  the gas constant,  $T$  the temperature and  $\alpha$  a heuristic sticking coefficient with values between 0 and 1. It is evident from Eq.(8.1) that the rate of shrinking by evaporation should scale with the surface of the droplet and that in that case, a deceleration of the shrinking should be observed over time, contrary to the experimental data. Moreover, any heating by laser light absorption would at most lead to a very small temperature rise due to the efficient cooling by the gas flow. In addition to these arguments, if evaporation were significant, some evaporation should still be observable even at low light intensity, where the heating of the droplet is negligible and hence any deviations from room temperature can be neglected. As seen from Fig.(8.5) however, there is no shrinking observable for low light intensities. We can therefore rule out evaporation as the dominant shrinking mechanism.

Similar reasoning may be used to exclude a photochemical reaction in which glycine absorbs a photon according to



where Gly(aq) is the solvated glycine molecule,  $h\nu$  is the energy of the incoming photon and P is the reaction product that is removed from the droplet (aq) into the surrounding gas phase (g) afterwards. As mentioned above molecular glycine is considered non-absorbing at 532nm. However, if we nevertheless assume that molecular glycine could be very weakly absorbing as in Eq.(8.2), the photon density inside the droplet would be constant over the course of the photochemical reaction. Hence, the first step in Eq.(8.2) would be pseudo-first order, for which the reaction rate is proportional to the concentration of glycine molecules in the droplet. Therefore, one would expect a decrease in the observed shrinking rate over time, which contradicts the experimental observation.

The examples above illustrate that any mechanism, in which glycine molecules directly absorb incoming photons, cannot explain the constant shrinking rates. This implies that a more intricate reaction must take place in

the droplet. We suggest the following simplified scheme with an additional reaction partner M:



where  $M^*$  denotes the photoexcited state of M and P is the reaction product of glycine in the presence of this photoexcited species. This scheme represents a mediated reaction in which the reaction partner M is activated by light absorption, and then reacts with glycine and returns back to the ground state. M shows the characteristics of a photosensitizer<sup>176-179</sup>, which is not consumed during the reaction, and therefore the amount of M remains constant in the droplet. We further assume that the light absorption of the photosensitizer M is the rate limiting step, i.e., that Eq.(8.3) proceeds much slower than Eq.(8.4). This is equivalent to requiring that M is only weakly absorbing, or that the concentration of M in the droplet is low. Since the amount of M in the rate limiting step (Eq.(8.3)) remains constant during the shrinking process, so does  $M^*$  (quasistationary), resulting in a constant rate of degradation of Gly (Eq.(8.4)). Assuming that the absolute concentration of M is much smaller than that of Gly at all times, and therefore has no relevant effect on the equilibrium water vapor pressure of the droplet, the volume shrinking rate is predicted to be constant in accordance with the experimental data.

Although the proposed scheme Eq.(8.3) and Eq.(8.4) concurs with the observed constant reaction rates, it does not yet specify the nature of the photosensitizer and its reaction with glycine. We first discuss potential candidates for the photosensitizer. Contamination during the preparation of the different aqueous glycine solutions used in this study is minimized by using pure substances (glycine purity  $\geq 99\%$ , water resistivity  $18.2\text{ M}\Omega\text{ s}$ ). No correlation between the shrinking rates in Fig.(8.5) and the age of the solution at the time of the measurements is observed, which indicates that there is no accumulation of photoactive contaminants in the solution after the preparation. We therefore propose that contamination is not the origin of the photosensitizer.

It is evident from the previous discussion that the photosensitizer must possess an absorption band at  $532\text{ nm}$ , which is not the case for single solvated glycine molecules. The optical properties of molecules may change however when forming intermolecular bonds, e.g. leading to an enhancement of the absorption and fluorescence in the case of protein aggregates<sup>180-183</sup> and amino acids clusters<sup>184</sup>. For glycine in particular, observations of light absorption

in the near UV/vis range have been attributed to the presence of mesoscopic clusters<sup>185,186</sup>, specifically due to the formation of hydrogen bonds between individual molecules<sup>168</sup>.

Mesoscopic clusters occur naturally in both undersaturated and supersaturated glycine solutions, though a kinetic barrier may have to be overcome for their formation<sup>185</sup>. The average size of the mesoscopic clusters, typically of the order of 100 nm for bulk solutions, depends not only on the monomer concentration but on the history of the sample, indicating that the clusters do not necessarily remain in thermodynamic equilibrium after formation<sup>185</sup>. Based on these observations, we propose that the photo-induced droplet shrinking is mediated by light absorption of mesoclusters in the glycine solution. These mesoclusters remain kinetically stable during the droplet shrinking, despite the decrease of the absolute number of glycine monomers (i. e. constant glycine monomer concentration). Hence, these clusters act as stable photosensitizers inside the droplets, in accordance with the observed constant shrinking rate. The observation of a constant initial shrinking rate thus allows us to narrow down the possible reaction mechanisms at work in the droplets. Alternative schemes might be conceivable, such as the existence of several reaction partners for glycine. However, there is no further experimental evidence in favor of more complex alternatives to the simple mechanism proposed (Eq.(8.3) and Eq.(8.4)). Furthermore, as pointed out above, mesoscopic glycine clusters match the requisite characteristics of the proposed photosensitizer, and are therefore likely candidates. To pursue the argument, let us further discuss the role of the mesoscopic clusters in the observed acceleration of the droplet shrinking.

The acceleration of the droplet shrinking proceeds relatively promptly at the point of acceleration when the particle has lost a typical amount of 75% of its volume (Fig.(8.4)). Assuming that the total number of mesoclusters remains approximately constant ( $M$  in Eq.(8.3) and Eq.(8.4)), their concentration has increased by an approximate factor of 4 at this point. The sudden nature of the shrinking acceleration hints at a phase transition inside the particle. In particular, the increase in mesocluster concentration may trigger the separation of a dense cluster phase inside the droplets as part of a liquid-liquid phase transition. While a definite conclusion has to await more detailed microscopic investigations, we present the following arguments in favor of this explanation.

Mesoscopic clusters in aqueous solutions are known to interact with focused light irradiation by assembling in the focal point of the light beam due to the

optical force that acts on the individual clusters<sup>170</sup>. This mechanic is the basis of laser-induced phase transitions<sup>169</sup>, in the particular case of glycine both for liquid-liquid phase separation<sup>170,173</sup> and solid crystal nucleation<sup>169-173</sup>. It should be noted at this point that the spot size in the focus of our optical trap is slightly larger ( $5\ \mu\text{m}$ ) than the typical droplet size, and that therefore, it might appear unlikely that the electromagnetic field gradient is strong enough to induce cluster aggregation in our case. However, micrometer sized droplets exhibit a large variance in the spatial distribution of the internal light field, owing to the nanofocusing effect<sup>26,154</sup>, which can provide the field gradients necessary for aggregation. If in the case of our trapped droplets, the acceleration is due to a phase transition, it would likely be assisted by the light irradiance. One would therefore expect a dependence of the observed shrinking acceleration on the incident light intensity. Fig.(8.7) shows the measured acceleration ratio, that is, the ratio between the shrinking rate after to before the point of acceleration, as a function of light intensity. From this data it is evident that the ratio increases with higher light intensity, which agrees with our explanation of a light-induced phase transition. Since in this scheme, the clusters are expected to aggregate in the regions of high light intensity after reaching a critical concentration, this would lead to a larger absorption rate and thus a larger subsequent reaction rate, in agreement with the observation. Further studies will be necessary to provide conclusive evidence for this explanation.

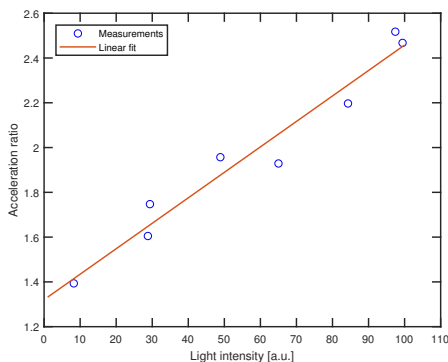


Figure 8.7: Droplet shrinking acceleration as function of light intensity. The solid line indicates the best linear fit.

More data will also be required to understand the specifics of the interaction between the photosensitizer and the solvated glycine molecules in Eq.(8.4). Here, we can only provide a qualitative discussion based on the available data. The Raman spectra (Fig.(8.6)) show no detectable change in the molecular composition, even after the droplet has lost the major part of its volume during the shrinking process. Since this observation rules out the accumulation of reaction products in the droplets over time, the reaction products must be small, volatile compounds that quickly evaporate into the surrounding gas phase. Known degradation mechanisms of glycine and other amino acids in aqueous solution proceed via reaction with radical species, in particular solvated electrons  $e_{\text{solv}}^-$  and hydroxyl  $\bullet\text{OH}$  radicals<sup>187-189</sup>, which form as part of a photosensitized reaction with chromophoric organic matter in water<sup>190-192</sup>. Currently, our data does not allow us to distinguish between different degradation pathways.

## 8.4 Conclusions

We have demonstrated that single micrometer sized aqueous glycine droplets respond to the illumination with laser light of 532 nm by shrinking, despite the fact that molecular glycine does not absorb in the near UV/vis range. Most remarkably, the volume shrinking rate remained constant over the major part of the shrinking process. This indicates a photo-induced decay of glycine molecules in the presence of a rate limiting catalyst, or photosensitizer, and the subsequent evaporation of small, volatile reaction products. Based on the available literature data, we propose that intrinsic mesoscopic clusters of glycine molecules formed by hydrogen bonding in the aqueous solution are the most plausible candidates for this photosensitizer. The presence of mesoscopic glycine clusters would also explain the sudden acceleration of the shrinking rate occurring at a volume loss of 75%. Because of its dependence on the light intensity, we attribute this sudden rate change to arise from the interaction of the mesoclusters with the incident light, possibly initiating a light-induced phase transition.

This study provides yet another example of the non-trivial interactions of light with aqueous glycine solutions<sup>169-173</sup>, which facilitate previously undiscovered reaction pathways - interactions that are likely not exclusive to glycine. Light harvesting by and light interaction with such mesoscopic photosensitizers in aerosol droplets might also have played a role in the formation

of more complex organic molecules under prebiotic conditions. Further investigations are needed to shed light on the specifics of the observed phenomena, and to yield new insight into the underlying reaction mechanisms, which remain elusive in part. Studying solutions in micrometer sized droplets (attoliter volumes) using high laser powers offers the advantage of much higher sensitivity to photo-induced reactions than typically achievable with bulk solutions.

## 8.5 Acknowledgements

This project was supported by the Japan Society for the Promotion of Science (JSPS Oversea Research Fellowship; S.I.), by the Swiss National Science Foundation (SNSF project number 200020\_200306), and by ETH Zürich. We are very grateful to D. Stapfer and M. Steger from our workshops for technical support, and to D. Zindel for helpful discussions.



## 9 Conclusion

Atmospheric aerosols continue to attract much attention due to the complicated role they play in many atmospheric processes. Optical trapping is a powerful tool to characterize individual aerosol particles in the laboratory, with the goal to obtain single particle data under well defined conditions. A particular focus of the present studies is on liquid aerosol droplets, which often exist in a thermodynamic equilibrium with the surrounding gas phase.

In this thesis, a number of characterization techniques have been used to explore the properties of single optically trapped aerosol particles, such as size, shape, refractive index and molecular composition (Chapter 3). These methods are based on analysis of the light scattering of the trapping beam by a trapped droplet. They are non-invasive and have a negligible impact on the thermodynamic equilibrium between the particle and its environment, hence they are well suited for the study of aerosol droplets.

A method that allows one to access the mass of optically trapped aerosol particles has been missing so far, and mass measurements of single atmospheric particles have been traditionally performed using an electrodynamic balance (EDB) for trapping. A main result of the present thesis is the development of a new method to measure the mass of single optically trapped aerosol particles (Chapter 4). Its principle is based on the measurement of particle dynamics that arise due to a periodic modulation of the trapping forces and the subsequent retrieval of the particle's inertia. Similar measurement principles have been demonstrated before<sup>36,41</sup>. The new method, however, exceeds the performance of comparable experiments described in the literature<sup>36-41</sup> with regard to several aspects relevant to atmospheric particles, in particular droplets: It is designed for application at ambient conditions, does not require light absorption by the particle and allows access to the submicrometer size range, where most atmospheric aerosol particles reside.

The performance of the optical mass measurement method has been demonstrated and its accuracy has been characterized in Chapter 5. We find typical values of a few % for the total uncertainty in mass for droplets with sizes in the micrometer range, specifically for radii of 1–2  $\mu\text{m}$ . These values are comparable to reported accuracies of EDB measurements for larger particles in the supermicrometer range. Thus, in this size range, the optical mass measurement method is an alternative to state-of-the-art EDB mass measurements, with the opportunity to extend such measurements also into the submicrometer range.

Mass is a fundamental property of any particle. Many atmospheric processes affect the mass of aerosol droplets, hence these processes can be characterized by measuring the droplet mass. The new method is therefore expected to have potential for a wide range of applications. In Chapter 6 we explore its applicability to measurements of hygroscopic mass growth factors of sea salt aerosols, one of the most abundant aerosol species in the atmosphere. Conflicting values have been published<sup>45,49</sup>, which limits the accuracy of atmospheric models of aerosol absorption and scattering cross-sections for climate predictions. We obtain new values for the hygroscopic mass growth factors of single sea salt droplets and use these results to critically review previously published values. We identified the definition of the dry salt mass of the droplet, which is used to derive the hygroscopic mass growth factors, as an issue. Based on the available data, it is argued that the unaccounted presence of hydrates in the dry salt mass is likely the reason for the observed discrepancies in previous experiments. It is suggested that reporting the hydrate mass of the reference dry sample should become part of a new standard for the determination of hygroscopic growth factors. This is expected to improve the comparability of the retrieved values and the transferability to atmospheric models for more accurate climate predictions.

While the performance of the optical mass measurement setup is comparable to EDB setups for micrometer sized droplets, a few advantages of the optical mass measurement are worth highlighting at this point. First, EDBs do not provide access to submicrometer particles. Mass data reported in the literature<sup>45,49</sup> has only been obtained for particles with radii  $R > 2 \mu\text{m}$ . Below this size range, mass data of single levitated droplets at ambient conditions have not been reported so far. The performance of the optical mass measurement setup for large submicrometer droplets ( $R \approx 0.5 \mu\text{m}$ ) has been demonstrated in Chapter 6. The relative accuracy is slightly less than for larger droplets. But with a typical total uncertainty still below  $\pm 10\%$ , this method can provide reliable mass data in a range that was previously inaccessible. It is

anticipated that the extended size range for optical mass measurements facilitates new single particle studies of size dependent effects, for example the size dependent hygroscopicity<sup>112</sup> of atmospheric aerosol particles. Secondly, the optical mass measurement method is straightforward to implement in existing counter-propagating tweezers (CPT) setups, as shown in Chapter 4. In contrast to EDBs, this method does not require a specific trapping cell design, thus offering more flexibility in the experimental setup. As an additional advantage, its measurement principle is not only applicable to trapping in the gas phase and vacuum, but also in liquid environments. The optical mass measurement method therefore also holds potential for application to liquid phase trapping. This avenue has been explored for micrometer sized glass spheres trapped in water in Chapter 7. These glass microspheres serve as a proxy for biological particles with similar sizes and masses, such as bacteria and other prokaryotic cells. Essentially the same experimental setup and procedure as for trapping in the gas phase was used to measure the mass of the trapped microspheres. It has been found that the current accuracy of the setup is not sufficient for measurements in the liquid phase due to the large damping of the particle and the resulting low signal amplitude of the particle oscillation.

The damping of the particle oscillation is characterized by the damping rate  $\Gamma_0 = \frac{1}{2\pi} \frac{\gamma}{m}$  (Chapter 4, Eq.(4.11)). For trapping in water, the limitation of the accuracy due to large damping and low oscillation amplitude is a consequence of the large drag coefficient  $\gamma$  of water. However, a similar limit is approached in the gas phase when trapping small particles ( $m \rightarrow 0$ ). Currently, a radius of  $R \approx 0.5 \mu\text{m}$  is the approximate lower limit for mass measurements with accuracies of  $< 10\%$  in the gas phase. As shown in Chapter 7, these accuracies are limited by systematic biases in the measurement electronics, in particular the position sensing photodiode used for particle tracking. The fundamental limit of the particle position detection, i.e. the random fluctuations of the particle due to Brownian motion at room temperature is, however, not relevant for the current measurement accuracy. It is therefore expected that an upgrade in the position sensing hardware will yield a substantial improvement over the current state of the mass measurement setup. Such an improvement is unlikely to suffice for the measurements in the liquid phase, where an improvement of at least 3 orders of magnitude is required. However, in the gas phase, it is expected to push the lower size limit of the method. As a current perspective, mass measurements of single large nanometer sized droplets ( $R \approx 200\text{--}300 \text{ nm}$ ) appear feasible, though further studies are needed for demonstration.

A limitation of the current setup is the restriction to particles that are approximately spherical in shape. This is a consequence of the Gaussian beam profiles of the CPT that only allow stable trapping and manipulation of such particles. Many aerosol particles are approximately spherical in shape, in particular all droplets. Nevertheless, application of the mass measurement principle to universal dual beam traps, which allow trapping of a wider range of particle shapes, is an interesting prospect and would broaden the applicability of this method. Future studies are needed to demonstrate whether the current measurement principle is applicable to CPTs with other beam shapes, in particular hollow beam shapes used in universal traps<sup>42</sup>, and to assess the measurement accuracies that can be achieved.

Single optically trapped aqueous glycine droplets have been characterized in Chapter 8. Photo-induced shrinking of the trapped droplet has been observed, which could be unambiguously attributed to the exposure to the light of the trapping beams at 532 nm. This previously unexpected photochemical reaction has been linked to the presence of light absorbing mesoscopic glycine clusters intrinsic to aqueous glycine solutions. Although some aspects of the observed phenomenon remain elusive, our results indicate a previously undiscovered photochemical pathway for glycine, which is photochemically inert at visible wavelengths in the molecular form. These photochemical pathways via the formation of molecular aggregates may be of particular importance for the chemistry of atmospheric aerosol droplets. To elucidate the exact mechanism of the observed reaction, further data is needed with regard to the volatile reaction products. Future mass studies with the new mass measurement method could be helpful here.

## 10 Appendix

### 10.1 Optical force calculation using far field expressions

In this section, a derivation is presented for Eq.(2.28). This equation is equivalent to

$$\int_S d^3r \nabla \cdot \boldsymbol{\sigma} = \frac{1}{c} (W_{\text{abs}} + W_{\text{scat}}) \cdot \hat{\mathbf{z}} - \int_{\partial S} d^2r \frac{\epsilon_0}{2} |\mathbf{E}_s|^2 \hat{\mathbf{r}} \quad (10.1)$$

in the far field limit, i.e. for a sufficiently large sphere  $S$ .

The incident electric and magnetic fields are given by

$$\begin{aligned} \mathbf{E}_0 &= e^{ikz} \hat{\mathbf{x}} \\ \mathbf{B}_0 &= \frac{1}{c} e^{ikz} \hat{\mathbf{y}} \end{aligned} \quad (10.2)$$

where  $\mathbf{B}_0$  is obtained from  $\mathbf{E}_0$  using Eq.(2.3). The scattered electric and

magnetic far fields are given by Eq.(2.12) and Eq.(2.16), respectively:

$$\begin{aligned}
 \mathbf{E}_s &= \sum_{l,m,p} i^l \frac{2l+1}{l(l+1)} (a_{lmp}^s \cdot \mathbf{M}_{lmp} - ib_{lmp}^s \cdot \mathbf{N}_{lmp}) \\
 &= \sum_{l,m,p} i^l \frac{2l+1}{l(l+1)} h_l^{(1)} (a_{lmp}^s \cdot \mathbf{m}_{lmp} + b_{lmp}^s \cdot \mathbf{n}_{lmp}) \\
 \mathbf{B}_s &= \frac{-i}{c} \sum_{l,m,p} i^l \frac{2l+1}{l(l+1)} (a_{lmp}^s \cdot \mathbf{N}_{lmp} - ib_{lmp}^s \cdot \mathbf{M}_{lmp}) \\
 &= \frac{1}{c} \sum_{l,m,p} i^l \frac{2l+1}{l(l+1)} h_l^{(1)} (a_{lmp}^s \cdot \mathbf{n}_{lmp} - b_{lmp}^s \cdot \mathbf{m}_{lmp})
 \end{aligned} \tag{10.3}$$

where  $\mathbf{B}_s$  is again obtained from  $\mathbf{E}_s$  using Eq.(2.3), and the properties of the vector harmonics listed in Eq.(2.5) and Eq.(2.6) were used. From the orthogonality relations Eq.(2.10) it can further be seen that

$$\hat{\mathbf{r}} \times \mathbf{E}_s = c \cdot \mathbf{B}_s \tag{10.4}$$

that is,  $\mathbf{r}$ ,  $\mathbf{E}_s$  and  $\mathbf{B}_s$  are pairwise orthogonal in the far field limit. Introducing the Poynting vector

$$\mathbf{S} = \frac{1}{2} \cdot \frac{1}{\mu_0} \mathbf{E} \times \bar{\mathbf{B}} \tag{10.5}$$

with the prefactor  $\frac{1}{2}$  due to time averaging and  $\mu_0$  the vacuum permeability, we find for incident and scattered Poynting vector

$$\begin{aligned}
 \mathbf{S}_0 &= \frac{1}{2} \cdot \frac{1}{\mu_0} \mathbf{E}_0 \times \bar{\mathbf{B}}_0 = \frac{\epsilon_0}{2} c |\mathbf{E}_0|^2 \hat{\mathbf{z}} = \frac{1}{2\mu_0} c |\mathbf{B}_0|^2 \hat{\mathbf{z}} = \frac{\epsilon_0 c}{2} \hat{\mathbf{z}} \\
 \mathbf{S}_s &= \frac{1}{2} \cdot \frac{1}{\mu_0} \mathbf{E}_s \times \bar{\mathbf{B}}_s = \frac{\epsilon_0}{2} c |\mathbf{E}_s|^2 \hat{\mathbf{r}} = \frac{1}{2\mu_0} c |\mathbf{B}_s|^2 \hat{\mathbf{r}}
 \end{aligned} \tag{10.6}$$

where  $\epsilon_0$  is the vacuum permittivity and  $|\mathbf{E}_0| = 1$ ,  $|\mathbf{B}_0| = \frac{1}{c}$  was used for  $\mathbf{S}_0$ .

We start in Eq.(10.1) by applying the Gauss divergence theorem:

$$\int_S d^3r \nabla \cdot \boldsymbol{\sigma} = \int_{\partial S} d^2r \boldsymbol{\sigma} \cdot \hat{\mathbf{r}} \tag{10.7}$$

where it was used that  $\hat{\mathbf{r}}$  is normal to the surface  $\partial S$ . Evaluating  $\boldsymbol{\sigma} \cdot \hat{\mathbf{r}}$  using

the definition of  $\sigma_{ij}$  in Eq.(2.24) yields

$$\sum_j \sigma_{ij} \cdot \hat{\mathbf{r}}_j = \frac{1}{2\mu_0} \left( \frac{1}{c^2} \bar{E}_i(\mathbf{E} \cdot \hat{\mathbf{r}}) + \bar{B}_i(\mathbf{B} \cdot \hat{\mathbf{r}}) - \left( \frac{1}{c^2} |\mathbf{E}|^2 + |\mathbf{B}|^2 \right) \hat{\mathbf{r}} \right) \quad (10.8)$$

where  $\mathbf{E} = \mathbf{E}_0 + \mathbf{E}_s$  and  $\mathbf{B} = \mathbf{B}_0 + \mathbf{B}_s$ . If  $S$  is sufficiently large (radius  $R_S \gg w$  incident beam width), then the incident wave vanishes everywhere on the surface  $\partial S$  except in forward ( $\theta = 0^\circ$ ) and backward ( $\theta = 180^\circ$ ) direction (again consider the Gaussian beam in Eq.(2.25) for an incident wave that is spatially confined in  $x$  and  $y$  and has a defined momentum along  $z$ ). At the two poles the surface normals are  $\hat{\mathbf{r}} = \hat{\mathbf{z}}$  ( $\theta = 0^\circ$ ) and  $\hat{\mathbf{r}} = -\hat{\mathbf{z}}$  ( $\theta = 180^\circ$ ) and therefore, they point parallel to the incident Poynting vector  $\mathbf{S}_0$  and perpendicular to  $\mathbf{E}_0$  and  $\mathbf{B}_0$ . Furthermore, it was already shown that the scattered Poynting vector  $\mathbf{S}_s$  is parallel to the surface normal  $\hat{\mathbf{r}}$ , and therefore  $\mathbf{E}_s$  and  $\mathbf{B}_s$  are perpendicular to  $\hat{\mathbf{r}}$ . Since incident and scattered wave are perpendicular to  $\hat{\mathbf{r}}$  or vanish for all points on the surface  $\partial S$ , Eq.(10.8) simplifies to

$$\begin{aligned} \sum_j \sigma_{ij} \cdot \hat{\mathbf{r}}_j &= - \left( \frac{\epsilon_0}{2} |\mathbf{E}|^2 + \frac{1}{2\mu_0} |\mathbf{B}|^2 \right) \hat{\mathbf{r}} \\ &= - \left( \frac{\epsilon_0}{2} |\mathbf{E}_0|^2 + \frac{\epsilon_0}{2} |\mathbf{E}_s|^2 + \frac{\epsilon_0}{2} \mathbf{E}_s \bar{\mathbf{E}}_0 + \frac{\epsilon_0}{2} \mathbf{E}_0 \bar{\mathbf{E}}_s \right. \\ &\quad \left. + \frac{1}{2\mu_0} |\mathbf{B}_0|^2 + \frac{1}{2\mu_0} |\mathbf{B}_s|^2 + \frac{1}{2\mu_0} \mathbf{B}_s \bar{\mathbf{B}}_0 + \frac{1}{2\mu_0} \mathbf{B}_0 \bar{\mathbf{B}}_s \right) \hat{\mathbf{r}} \\ &= -\frac{1}{c} (\mathbf{S}_0 + \mathbf{S}_s + \mathbf{S}_{0s}) \end{aligned} \quad (10.9)$$

where Eq.(10.6) was used in the last step and we have introduced the Poynting vector of the interference between incident and scattered wave

$$\mathbf{S}_{0s} = \frac{\epsilon_0 c}{2} \mathbf{E}_s \bar{\mathbf{E}}_0 + \frac{\epsilon_0 c}{2} \mathbf{E}_0 \bar{\mathbf{E}}_s + \frac{c}{2\mu_0} \mathbf{B}_s \bar{\mathbf{B}}_0 + \frac{c}{2\mu_0} \mathbf{B}_0 \bar{\mathbf{B}}_s \quad (10.10)$$

The Poynting vector of the interference vanishes everywhere on  $\partial S$  except in forward and backward direction. The intensity  $\mathbf{E}_s$  in backward direction is typically much weaker than in forward direction. Thus, as an additional approximation, the interference in backward direction is neglected in the following. This approximation corresponds to the observation that the light-particle interaction only affects the segment of the beam  $\mathbf{E}_0$  after the particle. The beam segment before the particle is not influenced by the presence of the particle in very good approximation. As a corollary the following identity is

obtained

$$\int_{\partial S} d^2r \mathbf{S}_{0s} \cdot \hat{\mathbf{r}} = \int_{\partial S} d^2r \mathbf{S}_{0s} \cdot \hat{\mathbf{z}} \quad (10.11)$$

As additional input in the derivation, the conservation of energy is discussed here. The energy flux through the surface  $\partial S$  has to be equal to the negative absorption rate  $W_{\text{abs}}$  of the particle. Denoting  $\mathbf{S}$  the Poynting vector of the total electromagnetic field, one obtains

$$\begin{aligned} W_{\text{abs}} &= - \int_{\partial S} d^2r \mathbf{S} \cdot \hat{\mathbf{r}} \\ &= - \frac{1}{2\mu_0} \int_{\partial S} d^2r (\mathbf{E}_0 + \mathbf{E}_s) \times (\mathbf{B}_0 + \mathbf{B}_s) \cdot \hat{\mathbf{r}} \\ &= - \int_{\partial S} d^2r \mathbf{S}_0 + \mathbf{S}_s + \mathbf{S}_{0s} \cdot \hat{\mathbf{r}} \\ &= -W_{\text{scat}} - \int_{\partial S} d^2r \mathbf{S}_{0s} \cdot \hat{\mathbf{z}} \end{aligned} \quad (10.12)$$

where in the last step we have identified the scattering rate in Eq.(2.29) and the integral over  $\mathbf{S}_0$  vanishes for symmetry reasons. We now have all the



pieces to proceed from Eq.(10.7) to obtain

$$\begin{aligned}
 \mathbf{F} &= \int_{\partial S} d^2r \boldsymbol{\sigma} \cdot \hat{\mathbf{r}} \\
 &= -\frac{1}{c} \int_{\partial S} d^2r \mathbf{S}_0 + \mathbf{S}_s + \mathbf{S}_{0s} \\
 \left[ \int_{\partial S} d^2r \mathbf{S}_0 = 0 \right] \\
 &= -\frac{1}{c} \int_{\partial S} d^2r \mathbf{S}_s - \frac{1}{c} \int_{\partial S} d^2r \mathbf{S}_{0s} \\
 [\mathbf{S}_{0s} \parallel +\hat{\mathbf{z}}] \\
 &= -\frac{1}{c} \int_{\partial S} d^2r \mathbf{S}_s - \frac{1}{c} \left( \int_{\partial S} d^2r \mathbf{S}_{0s} \cdot \hat{\mathbf{z}} \right) \hat{\mathbf{z}} \\
 &= -\frac{1}{c} \int_{\partial S} d^2r \mathbf{S}_s + \frac{1}{c} (W_{\text{abs}} + W_{\text{scat}}) \hat{\mathbf{z}}
 \end{aligned} \tag{10.13}$$

substituting Eq.(10.6) for  $\mathbf{S}_s$  yields Eq.(2.28).

## 10.2 Holography reconstruction

Many algorithms have been used in the literature<sup>193</sup> for reconstruction of the original scattered wave from a recorded hologram, and a review of these techniques is not within the scope of this chapter. Here an algorithm for efficient evaluation of Eq.(2.37) is presented, which uses comparably few, well justified assumptions. The algorithm is in part derived in previous articles<sup>33,53,194</sup>. The complete derivation of the algorithm however has not been presented elsewhere to the best of our knowledge.

We assume the hologram screen  $A$  in Eq.(2.37) is a rectangular screen positioned parallel to the  $x, y$  plane such that the center lies on the  $z$  axis. The reconstructed scattered field  $E_h$  inside  $A$  is given by Eq.(2.36). For an incident spherical wave originating at  $\mathbf{O} = (0/0/0)$ , the reconstructed scattered

field takes the form

$$E_h(\mathbf{s}) = h(\mathbf{s}) \cdot \alpha \frac{e^{iks}}{s} \quad (10.14)$$

where  $\mathbf{s} = (u/v/L)$  are the screen coordinates and  $s = |\mathbf{s}|$  is the distance of  $\mathbf{s}$  with respect to  $\mathbf{O}$ . Here  $L$  denotes the  $z$  coordinate of all points of  $A$ , which corresponds to the distance between the center of the screen and  $\mathbf{O}$ . The scaling factor  $\alpha$  is not relevant for the hologram reconstruction and is neglected in the following ( $\alpha = 1$ ). Using this, Eq.(2.37) can be rewritten as

$$\begin{aligned} E_h(\mathbf{r}) &= -\frac{1}{4\pi} \int_A d^2s h(\mathbf{s}) \left( \frac{e^{iks}}{s} \frac{\partial}{\partial \mathbf{n}} \frac{e^{-ik|\mathbf{s}-\mathbf{r}|}}{|\mathbf{s}-\mathbf{r}|} - \frac{e^{-ik|\mathbf{s}-\mathbf{r}|}}{|\mathbf{s}-\mathbf{r}|} \cdot \frac{\partial}{\partial \mathbf{n}} \frac{e^{iks}}{s} \right) \\ &= -\frac{1}{4\pi} \int_A d^2s h(\mathbf{s}) \frac{e^{iks}}{s^2} \frac{e^{-ik|\mathbf{s}-\mathbf{r}|}}{|\mathbf{s}-\mathbf{r}|^2} \cdot \\ &\quad \left( \left( -ik - \frac{1}{|\mathbf{s}-\mathbf{r}|} \right) s(L-z) - \left( ik - \frac{1}{s} \right) |\mathbf{s}-\mathbf{r}|L \right) \end{aligned} \quad (10.15)$$

where  $\frac{\partial}{\partial \mathbf{n}}$  is the derivative along the normal of  $A$ , which coincides with the  $z$ -axis, and  $z$  is the corresponding component of  $\mathbf{r} = (x/y/z)$ . Note that  $\frac{\partial}{\partial \mathbf{n}}$  acts on  $\mathbf{s}$ , but not on  $\mathbf{r}$ . In the far field limit, we have  $ks \gg 1$ . Furthermore, we place the particle sufficiently close to the origin  $\mathbf{O}$ , such that  $s \gg r$  for all points of interest for the reconstruction (points that are in the local volume of the particle). With this, Eq.(10.15) is simplified to

$$\begin{aligned} E_h(\mathbf{r}) &= -\frac{1}{4\pi} \int_A d^2s h(\mathbf{s}) \frac{e^{iks}}{s^2} \frac{e^{-ik|\mathbf{s}-\mathbf{r}|}}{s^2} \cdot (-2iksL) \\ &= \frac{ik}{2\pi} L \int_A d^2s h(\mathbf{s}) \frac{e^{-ik(|\mathbf{s}-\mathbf{r}|-s)}}{s^3} \end{aligned} \quad (10.16)$$

The terms in the exponential are approximated by a Taylor expansion in the limit  $\frac{r}{s} \rightarrow 0$

$$-ik(|\mathbf{s}-\mathbf{r}|-s) = ik \frac{\mathbf{s}}{s} \cdot \mathbf{r} - ik \frac{\mathbf{r}}{s} \cdot \mathbf{r} + \mathcal{O}\left(kr \frac{r^2}{s^2}\right) \quad (10.17)$$

Truncating the Taylor series after the first non-vanishing order yields

$$E_h(\mathbf{r}) = \frac{ik}{2\pi} L \int_A d^2s h(\mathbf{s}) \frac{e^{ik\frac{\mathbf{s}}{s} \cdot \mathbf{r}}}{s^3} \quad (10.18)$$

This integral can be transformed using a non-linear coordinate transformation,  $\mathbf{s} = (u/v/L) \rightarrow \mathbf{t} = (p/q/L)$  defined by

$$p = \frac{u}{s} \quad q = \frac{v}{s} \quad (10.19)$$

with the reverse transformation

$$u = L \frac{p}{(1-p^2-q^2)^{\frac{1}{2}}} \quad v = L \frac{q}{(1-p^2-q^2)^{\frac{1}{2}}} \quad (10.20)$$

Note that  $p$  and  $q$  are dimensionless and  $p^2 + q^2 < 1$ . The determinant of the Jacobian of this transformation is

$$\det(J) = \frac{s^4}{L^2} = \frac{L^2}{(1-p^2-q^2)^2} \quad (10.21)$$

Therefore the differentials transform according to  $d^2s = \frac{L^2}{(1-p^2-q^2)^2} d^2t$ . Using this we omit the constant prefactor  $\frac{ik}{2\pi}$  and arrive at the final expression

$$\begin{aligned} E_h(x, y) &\sim L \int_{-W-H}^{+W+H} \int_{-W-H}^{+W+H} d^2s h(u, v) \frac{e^{ik \frac{ux+vy+Lz}{(u^2+v^2+L^2)^{\frac{1}{2}}}}}{(u^2+v^2+L^2)^{\frac{3}{2}}} \\ &= \int_{-W'-H'(p)}^{+W'+H'(p)} \int_{-W'-H'(p)}^{+W'+H'(p)} dpdq e^{ik(px+qy)} \\ &\quad (1-p^2-q^2)^{-\frac{1}{2}} e^{ikz(1-p^2-q^2)^{\frac{1}{2}}} h(u(p, q), v(p, q)) \\ &= \int_{-W'-H'(p)}^{+W'+H'(p)} \int_{-W'-H'(p)}^{+W'+H'(p)} dpdq e^{ik(px+qy)} \cdot \tilde{h}(p, q) \end{aligned} \quad (10.22)$$

where  $H$  and  $W$  are half the height and width of the screen  $A$ ,  $H'$  and  $W'$  the respective dimensions in the transformed space, and

$$\tilde{h}(p, q) = (1-p^2-q^2)^{-\frac{1}{2}} e^{ikz(1-p^2-q^2)^{\frac{1}{2}}} h(u(p, q), v(p, q)) \quad (10.23)$$

is the transformed hologram. Due to the non-linear transformation, the transformed area limited by  $p = \pm W'$  and  $q = \pm H(p)'$  is no longer a rectangle. It can be shown using Eq.(10.19) and Eq.(10.20) that the transformed area is the overlap between two ellipses (see also Latychevskaia et al.<sup>195</sup>), which are described by

$$\begin{aligned} \left(1 + \frac{L^2}{W^2}\right) p^2 + q^2 &= 1 \\ p^2 + \left(1 + \frac{L^2}{H^2}\right) q^2 &= 1 \end{aligned} \quad (10.24)$$

This is equivalent to stating that

$$\begin{aligned} W' &= \frac{W}{(W^2 + L^2)^{\frac{1}{2}}} \\ H'(p) &= \begin{cases} \left(1 - p^2 \left(1 + \frac{L^2}{W^2}\right)\right)^{\frac{1}{2}}, & \text{if } |p| > \frac{W}{(W^2 + H^2 + L^2)^{\frac{1}{2}}} \\ \left(\frac{1 - p^2}{1 + \frac{L^2}{H^2}}\right)^{\frac{1}{2}}, & \text{if } |p| \leq \frac{W}{(W^2 + H^2 + L^2)^{\frac{1}{2}}} \end{cases} \end{aligned} \quad (10.25)$$

The advantage of Eq.(10.22) over Eq.(2.37) for computation is that it represents a 2d Fourier transform of  $\tilde{h}$ , which can be efficiently calculated using a fast Fourier transform (FFT) algorithm. Therefore, instead of evaluating Eq.(2.37) for a 3d grid of  $\mathbf{r}$  values, a 2d slice of the particle can be reconstructed in one step using Eq.(10.22). The 3d particle is then obtained by repeating this step for different grid points along the  $z$  axis. To make use of the FFT algorithm,  $\tilde{h}$  has to be sampled on equidistant points in a rectangular area. The rectified  $\tilde{h}_{\text{rec}}$  is obtained by defining a 2d grid with dimensions  $W'_{\text{rec}} \times H'_{\text{rec}} = \frac{W}{(W^2 + L^2)^{\frac{1}{2}}} \times \frac{H}{(H^2 + L^2)^{\frac{1}{2}}}$ , which is the smallest rectangle that encompasses the transformed area, and

$$\tilde{h}_{\text{rec}}(p_i, q_j) = \begin{cases} \tilde{h}(p_i, q_j) & \text{if point } (p_i, q_j) \text{ is inside transformed area} \\ 0 & \text{otherwise} \end{cases} \quad (10.26)$$

## Bibliography

1. Boucher, O. *et al.* *Clouds and Aerosols in Climate change 2013: The Physical Science Basis. Contribution of Working Group I to the Fifth Assessment Report of the Intergovernmental Panel on Climate Change* (Cambridge University Press, 2013).
2. Pöschl, U. & Shiraiwa, M. *Chem. Rev.* **115**, 4440 (2015).
3. Myhre, G. *et al.* *Anthropogenic and Natural Radiative Forcing in Climate Change 2013 – The Physical Science Basis: Working Group I Contribution to the Fifth Assessment Report of the Intergovernmental Panel on Climate Change* 659 (Cambridge University Press, 2013).
4. Ashkin, A. *PRL* **24**, 156 (1970).
5. Ashkin, A., Dziedzic, J. M. & Yamane, T. *Nature* **330**, 769 (1987).
6. Guck, J. *et al.* *Biophys. J.* **81**, 767 (2001).
7. Wang, M. D., Yin, H., Landick, R., Gelles, J. & Block, S. M. *Biophys. J.* **72**, 1335 (1997).
8. Brau, R. *et al.* *J. Opt. A* **9**, S103 (2007).
9. Ashkin, A., Schütze, K., Dziedzic, J., Euteneuer, U. & Schliwa, M. *Nature* **348**, 346 (1990).
10. Block, S. M., Goldstein, L. S. & Schnapp, B. J. *Nature* **348**, 348 (1990).
11. Shepherd, G., Corey, D. P. & Block, S. M. *PNAS* **87**, 8627 (1990).
12. Svoboda, K., Schmidt, C. F., Schnapp, B. J. & Block, S. M. *Nature* **365**, 721 (1993).
13. Ishijima, A. *et al.* *Cell* **92**, 161 (1998).
14. Puppels, G., Garritsen, H., Kummer, J. & Greve, J. *Cytomet.: J. Inter. Soc. Anal. Cyto.* **14**, 251 (1993).
15. Wood, B. R., Caspers, P., Puppels, G. J., Pandiancherri, S. & McNaughton, D. *Anal. Bioanal. Chem.* **387**, 1691 (2007).

16. Gross, S. P. *Application of optical traps in Vivo in Methods in Enzymology* (Elsevier, 2003).
17. Ashok, P. C. & Dholakia, K. *Curr. Opin. Biotechnol.* **23**, 16 (2012).
18. Gieseler, J., Novotny, L. & Quidant, R. *Nat. Phys.* **9**, 806 (2013).
19. Ranjit, G., Cunningham, M., Casey, K. & Geraci, A. A. *PRA* **93**, 053801 (2016).
20. Millen, J., Monteiro, T. S., Pettit, R. & Vamivakas, A. N. *Rep. Prog. Phys.* **83**, 026401 (2020).
21. Gonzalez-Ballester, C., Aspelmeyer, M., Novotny, L., Quidant, R. & Romero-Isart, O. *Science* **374**, eabg3027 (2021).
22. Ahn, J. *et al. Nat. Nanotech.* **15**, 89 (2020).
23. Van der Laan, F. *et al. PRA* **102**, 013505 (2020).
24. Athanasiadis, A. *et al. PCCP* **18**, 30385 (2016).
25. Reid, J. P. *et al. Nat. Comm.* **9**, 956 (2018).
26. Cremer, J. W., Thaler, K. M., Haisch, C. & Signorell, R. *Nat. Comm.* **7**, 10941 (2016).
27. Cotterell, M. I., Preston, T. C., Orr-Ewing, A. J. & Reid, J. P. *Aero. Sci. Tech.* **50**, 1077 (2016).
28. Davies, J. F. & Wilson, K. R. *Anal. Chem.* **88**, 2361 (2016).
29. King, M. D., Thompson, K. C., Ward, A. D., Pfrang, C. & Hughes, B. R. *Faraday Discuss.* **137**, 173 (2008).
30. David, G., Parmentier, E. A., Taurino, I. & Signorell, R. *Sci. Rep.* **10**, 7929 (2020).
31. Esat, K., David, G., Poulkas, T., Shein, M. & Signorell, R. *PCCP* **20**, 11598 (2018).
32. David, G., Esat, K., Ritsch, I. & Signorell, R. *PCCP* **18**, 5477 (2016).
33. David, G., Esat, K., Thanopoulos, I. & Signorell, R. *Comm. Chem.* **1**, 46 (2018).
34. Schweiger, G. *J. Aero. Sci.* **21**, 483 (1990).
35. Kalume, A., Wang, C., Santarpia, J. & Pan, Y.-L. *Chem. Phys. Lett.* **706**, 255 (2018).
36. Ricci, F., Cuairan, M. T., Conangla, G. P., Schell, A. W. & Quidant, R. *Nano Lett.* **19**, 6711 (2019).
37. Delić, U. *et al. Quant. Sci. Tech.* **5**, 025006 (2020).

## BIBLIOGRAPHY

---

38. Hillberry, L. E. *et al. Phys. Rev. Appl.* **14**, 044027 (2020).
39. Carlse, G. *et al. Phys. Rev. Appl.* **14**, 024017 (2 2020).
40. Bera, S. K. *et al. Opt. Lett.* **41**, 4356 (2016).
41. Lin, J., Deng, J., Wei, R., Li, Y.-q. & Wang, Y. *JOSA B* **34**, 1242 (2017).
42. Gong, Z., Pan, Y.-L., Videen, G. & Wang, C. *J. Quant. Spect. Rad. Transf.* **214**, 94 (2018).
43. Davis, E. J. & Ray, A. K. *J. Colloid Interface Sci.* **75**, 566 (1980).
44. Hartung, W. & Avedisian, C. *Proc. Roy. Soc. Lond. A* **437**, 237 (1992).
45. Tang, I. N., Tridico, A. & Fung, K. *J. Geophys. Res.: Atmos.* **102**, 23269 (1997).
46. McMurry, P. *AEROSOLS — Observations and Measurements in Encyclopedia of Atmospheric Sciences* (Academic Press, Oxford, 2003).
47. Zhang, K. M., Knipping, E. M., Wexler, A. S., Bhave, P. V. & Tonnesen, G. S. *Atmos. Env.* **39**, 3373 (2005).
48. Zieger, P., Fierz-Schmidhauser, R., Weingartner, E. & Baltensperger, U. *Atmos. Chem. Phys.* **13**, 10609 (2013).
49. Zieger, P. *et al. Nat. Comm.* **8**, 15883 (2017).
50. Bohren, C. F. & Huffman, D. R. *Absorption and Scattering of Light by Small Particles* (Wiley-VCH Verlag, 2004).
51. Frezza, F., Mangini, F. & Tedeschi, N. *JOSA A* **35**, 163 (2018).
52. Gabor, D. *Nature* **161**, 777 (1948).
53. Barton, J. J. *PRL* **61**, 1356 (1988).
54. Gabor, D. *Proc. Roy. Soc. Lond. A* **197**, 454 (1949).
55. Latychevskaia, T. *JOSA A* **36**, D31 (2019).
56. Gardiner, D. J. & Graves, P. R. *Practical Raman Spectroscopy* (Springer-Verlag, 1989).
57. Prince, R. C., Frontiera, R. R. & Potma, E. O. *Chem. Rev.* **117**, 5070 (2017).
58. Oraevsky, A. N. *Quant. elec.* **32**, 377 (2002).
59. Reich, O., David, G. & Signorell, R. in *Optical Trapping and Optical Micromanipulation XVIII* **11798**, 1179827 (2021).
60. Reich, O., David, G., Esat, K. & Signorell, R. *Comm. Phys.* **3**, 223 (2020).

61. Lee, A. K., Ling, T. & Chan, C. K. *Faraday Discuss.* **137**, 245 (2008).
62. Liang, Z., Chu, Y., Gen, M. & Chan, C. K. *Atmos. Chem. Phys.* **22**, 3017 (2022).
63. Murata, S. & Yasuda, N. *Opt. Laser Tech.* **32**, 567 (2000).
64. Xu, W., Jericho, M., Meinertzhagen, I. & Kreuzer, H. *PNAS* **98**, 11301 (2001).
65. Krieger, U. K., Marcolli, C. & Reid, J. P. *Chem. Soc. Rev.* **41**, 6631 (2012).
66. Davis, E. J. *Aero. Sci. Tech.* **2**, 121 (1982).
67. Paul, W. *Rev. Mod. Phys.* **62**, 531 (1990).
68. Nie, Z. *et al. Angew. Chem.* **45**, 8131 (2006).
69. Dilling, J., Blaum, K., Brodeur, M. & Eliseev, S. *Annu. Rev. Nucl. Part. Sci.* **68**, 45 (2018).
70. Scigelova, M. & Makarov, A. *Proteomics* **6**, 16 (2006).
71. Tang, I. & Munkelwitz, H. *J. Geophys. Res.: Atmos.* **99**, 18801 (1994).
72. Landau, L. D. & Lifshitz, E. M. *Viscous Fluids* in *Fluid Mechanics* 2nd ed. (Pergamon Press, 1987).
73. Cunningham, E. *Proc. Roy. Soc. Lond. A* **83**, 357 (1910).
74. Moshfegh, A., Shams, M., Ahmadi, G. & Ebrahimi, R. *Colloids Surf. A* **345**, 112 (2009).
75. Mylona, S. K. *et al. J. Phys. Chem. Ref. Data* **43**, 013104 (2014).
76. Arita, Y., Mazilu, M. & Dholakia, K. *Nat. Comm.* **4**, 2374 (2013).
77. Pérez García, L., Donlucas Pérez, J., Volpe, G., V Arzola, A. & Volpe, G. *Nat. Comm.* **9**, 5166 (2018).
78. McGloin, D. *Philos. Trans. R. Soc. A* **364**, 3521 (2006).
79. He, H., Friese, M., Heckenberg, N. & Rubinsztein-Dunlop, H. *PRL* **75**, 826 (1995).
80. Maragò, O. M., Jones, P. H., Gucciardi, P. G., Volpe, G. & Ferrari, A. C. *Nat. Nanotech.* **8**, 807 (2013).
81. Dufresne, E. R., Spalding, G. C., Dearing, M. T., Sheets, S. A. & Grier, D. G. *Rev. Sci. Instr.* **72**, 1810 (2001).
82. Liesener, J., Reichert, M., Haist, T. & Tiziani, H. J. *Opt. Comm.* **185**, 77 (2000).



## BIBLIOGRAPHY

---

83. Jesacher, A., Fürhapter, S., Bernet, S. & Ritsch-Martel, M. *Opt. Express* **12**, 4129 (2004).
84. Ceconi, C., Shank, E. A., Bustamante, C. & Marqusee, S. *Science* **309**, 2057 (2005).
85. Hajizadeh, F. *et al. Optica* **4**, 746 (2017).
86. Neuman, K. C. & Block, S. M. *Rev. Sci. Instr.* **75**, 2787 (2004).
87. Li, T., Kheifets, S., Medellin, D. & Raizen, M. G. *Science* **328**, 1673 (2010).
88. Reimann, R. *et al. PRL* **121**, 033602 (2018).
89. Svak, V. *et al. Nat. Comm.* **9**, 5453 (2018).
90. Wills, J. B., Knox, K. J. & Reid, J. P. *Chem. Phys. Lett.* **481**, 153 (2009).
91. Mitchem, L. & Reid, J. P. *Chemical Society Reviews* **37**, 756 (2008).
92. Davis, R. D., Lance, S., Gordon, J. A. & Tolbert, M. A. *Anal. Chem.* **87**, 6186 (2015).
93. Cotterell, M. I. *et al. PCCP* **16**, 2118 (2014).
94. Guillon, M., Dholakia, K. & McGloin, D. *Opt. Express* **16**, 7655 (2008).
95. Bzdek, B. R., Power, R. M., Simpson, S. H., Reid, J. P. & Royall, C. P. *Chem. Sci.* **7**, 274 (2016).
96. Peng, C., Chan, M. N. & Chan, C. K. *Environ. Sci. Tech.* **35**, 4495 (2001).
97. Tang, I., Fung, K., Imre, D. & Munkelwitz, H. *Aero. Sci. Tech.* **23**, 443 (1995).
98. Davies, J. F. *Aero. Sci. Tech.* **53**, 309 (2019).
99. Murphy, D. M. *Science* **307**, 1888 (2005).
100. Miles, R. E., Carruthers, A. E. & Reid, J. P. *Laser Photonics Rev.* **5**, 534 (2011).
101. Morris, J. *et al. Geophys. Res. Lett.* **29**, 71 (2002).
102. Smith, G. D., Woods, E., DeForest, C. L., Baer, T. & Miller, R. E. *J. Phys. Chem. A* **106**, 8085 (2002).
103. Ashkin, A. & Dziedzic, J. *PRL* **54**, 1245 (1985).
104. Constable, A., Kim, J., Mervis, J., Zarinetchi, F. & Prentiss, M. *Opt. Lett.* **18**, 1867 (1993).

105. Čížmár, T., Garcés-Chávez, V., Dholakia, K. & Zemánek, P. *Applied Physics Letters* **86**, 174101 (2005).
106. Rkiouak, L. *et al.* *PCCP* **16**, 11426 (2014).
107. Rafferty, A., Gorkowski, K., Zuend, A. & Preston, T. C. *PNAS* **116**, 19880 (2019).
108. Greenspan, L. *J. Res. Natl. Bur. Stand. A Phys. Chem.* **81**, 89 (1977).
109. Zhang, H.-L. & Han, S.-J. *J. Chem. Eng. Data* **41**, 516 (1996).
110. Topping, D. *et al.* *Geoscient. Model Dev.* **9**, 899 (2016).
111. Chirife, J. & Resnik, S. L. *J. Food Sci.* **49**, 1486 (1984).
112. Laskina, O. *et al.* *J. Phys. Chem. A* **119**, 4489 (2015).
113. Hu, D. *et al.* *Aero. Air Qual. Res.* **10**, 255 (2010).
114. Swietlicki, E. *et al.* *Tellus B* **60**, 432 (2008).
115. Park, K. *et al.* *PNAS* **107**, 20691 (2010).
116. Popescu, G., Park, K., Mir, M. & Bashir, R. *Lab Chip* **14**, 646 (2014).
117. Arlett, J., Myers, E. & Roukes, M. *Nat. Nanotech.* **6**, 203 (2011).
118. Cadart, C., Venkova, L., Recho, P., Lagomarsino, M. C. & Piel, M. *Nat. Phys.* **15**, 993 (2019).
119. Kalantarifard, F. *et al.* *Nat. Comm.* **10**, 2683 (2019).
120. Chan, M. N., Choi, M. Y., Ng, N. L. & Chan, C. K. *Environ. Sci. Tech.* **39**, 1555 (2005).
121. Hess, M., Koepke, P. & Schult, I. *Bull. Am. Meteorol. Soc.* **79**, 831 (1998).
122. Kreidenweis, S. *et al.* *Atmos. Chem. Phys.* **5**, 1357 (2005).
123. Koehler, K. *et al.* *Atmos. Chem. Phys.* **6**, 795 (2006).
124. Köhler, H. *Trans. Farad. Soc.* **32**, 1152 (1936).
125. Viana, M. *et al.* *Sci. Total Environ.* **472**, 825 (2014).
126. Lewis, E. R. & Schwartz, S. E. *Sea salt aerosol production: mechanisms, methods, measurements, and models* (American geophysical union, 2004).
127. Quinn, P. K., Collins, D. B., Grassian, V. H., Prather, K. A. & Bates, T. S. *Chem. Rev.* **115**, 4383 (2015).
128. Grythe, H., Ström, J., Krejci, R., Quinn, P. & Stohl, A. *Atmos. Chem. Phys.* **14**, 1277 (2014).

## BIBLIOGRAPHY

---

129. Fuentes, E., Coe, H., Green, D., de Leeuw, G. & McFiggans, G. *Atmos. Meas. Tech.* **3**, 141 (2010).
130. Rosasco, G. J. & Roedder, E. *Geochim. Cosmochim. Acta* **43**, 1907 (1979).
131. Dubessy, J., Geisler, D., Kosztolanyi, C. & Vernet, M. *Geochim. Cosmochim. Acta* **47**, 1 (1983).
132. Aarnoutse, P. J. & Westerhuis, J. A. *Anal. Chem.* **77**, 1228 (2005).
133. Qiu, Y. *et al. Chem. Geol.* **533**, 119447 (2020).
134. Richardson, C. & Kurtz, C. *JACS* **106**, 6615 (1984).
135. Steimer, S. S. *et al. Atmos. Meas. Tech.* **8**, 2397 (2015).
136. Frossard, A. A. & Russell, L. M. *Environ. Sci. Tech.* **46**, 13326 (2012).
137. Prieto-Taboada, N., Gomez-Laserna, O., Martinez-Arkarazo, I., Olazabal, M. Á. & Madariaga, J. M. *Anal. Chem.* **86**, 10131 (2014).
138. Xiao, H.-S. *et al. Environ. Sci. Tech.* **42**, 8698 (2008).
139. Nandy, L. *et al. ACS Earth Space Chem.* **3**, 1260 (2019).
140. Davis, R. D., Lance, S., Gordon, J. A., Ushijima, S. B. & Tolbert, M. A. *PNAS* **112**, 15815 (2015).
141. Wallace, A. F. *et al. Science* **341**, 885 (2013).
142. Chakraborty, D. & Patey, G. *Chem. Phys. Lett.* **587**, 25 (2013).
143. Nielsen, M. H., Aloni, S. & De Yoreo, J. J. *Science* **345**, 1158 (2014).
144. Baumgartner, J. *et al. Nat. Mater.* **12**, 310 (2013).
145. Lee, S. *et al. PNAS* **113**, 13618 (2016).
146. Su, B. *et al. Atmos. Env.* **290**, 119365 (2022).
147. Sheng, H.-P. & Huggins, R. A. *Am. J. Clin. Nutr.* **32**, 630 (1979).
148. Kauzmann, W. *Some factors in the interpretation of protein denaturation in Advances in protein chemistry* (Elsevier, 1959).
149. Baldwin, R. L. *PNAS* **111**, 13052 (2014).
150. Porter, D. & Vollrath, F. *Soft Matter* **4**, 328 (2008).
151. Ashkin, A. & Dziedzic, J. *Appl. Phys. Lett.* **19**, 283 (1971).
152. Bones, D. L., Reid, J. P., Lienhard, D. M. & Krieger, U. K. *PNAS* **109**, 11613 (2012).
153. Walser, M. L., Park, J., Gomez, A. L., Russell, A. R. & Nizkorodov, S. A. *J. Phys. Chem. A* **111**, 1907 (2007).

154. Corral Arroyo, P. *et al. Science* **376**, 293 (2022).
155. Altaf, M. B., Zuend, A. & Freedman, M. A. *Chem. Comm.* **52**, 9220 (2016).
156. Kucinski, T. M., Dawson, J. N. & Freedman, M. A. *J. Phys. Chem. Lett.* **10**, 6915 (2019).
157. Bzdek, B. R. & Reid, J. P. *J. Chem. Phys.* **147**, 220901 (2017).
158. Lee, J. K., Banerjee, S., Nam, H. G. & Zare, R. N. *Q. Rev. Biophys.* **48**, 437 (2015).
159. Girod, M., Moyano, E., Campbell, D. I. & Cooks, R. G. *Chem. Sci.* **2**, 501 (2011).
160. Lee, J. K., Samanta, D., Nam, H. G. & Zare, R. N. *JACS* **141**, 10585 (2019).
161. Ruiz-Lopez, M. F., Francisco, J. S., Martins-Costa, M. T. & Anglada, J. M. *Nat. Rev. Chem.* **4**, 459 (2020).
162. Bain, R. M., Sathyamoorthi, S. & Zare, R. N. *Angew. Chem.* **129**, 15279 (2017).
163. Tervahattu, H., Tuck, A. & Vaida, V. *Chemistry in prebiotic aerosols: a mechanism for the origin of life* in *Origins* (Springer, 2004).
164. Arnstein, H. *The metabolism of glycine* in *Advances in protein chemistry* (Elsevier, 1954).
165. Hall, J. C. *J. Parenter. Enter. Nutr.* **22**, 393 (1998).
166. Jackson, A. A. *Eur. J. Clin. Nutr.* **45**, 59 (1991).
167. Bhat, M. N. & Dharmaparakash, S. *J. Cryst. Growth* **236**, 376 (2002).
168. Terpugov, E. L., Kondratyev, M. S. & Degtyareva, O. V. *J. Biomol. Struct. Dyn.* **39**, 108 (2021).
169. Alexander, A. J. & Camp, P. J. *J. Chem. Phys.* **150**, 040901 (2019).
170. Sugiyama, T., Yuyama, K.-i. & Masuhara, H. *Acc. Chem. Res.* **45**, 1946 (2012).
171. Zaccaro, J., Matic, J., Myerson, A. S. & Garetz, B. A. *Cryst. Growth Des.* **1**, 5 (2001).
172. Garetz, B. A., Matic, J. & Myerson, A. S. *PRL* **89**, 175501 (2002).
173. Yuyama, K.-i., Sugiyama, T. & Masuhara, H. *J. Phys. Chem. Lett.* **1**, 1321 (2010).
174. Ashkin, A. *PNAS* **94**, 4853 (1997).

## BIBLIOGRAPHY

---

175. Parmentier, E. A. *et al. J. Phys. Chem. A* **126**, 4456 (2022).
176. Corral Arroyo, P. *et al. Environ. Sci. Tech.* **52**, 7680 (2018).
177. George, C., Ammann, M., D'Anna, B., Donaldson, D. & Nizkorodov, S. A. *Chem. Rev.* **115**, 4218 (2015).
178. Wang, X. *et al. Environ. Sci. Tech.* **54**, 3114 (2020).
179. Rapf, R. J. & Vaida, V. *PCCP* **18**, 20067 (2016).
180. Homchaudhuri, L. & Swaminathan, R. *Bull. Chem. Soc. Jpn.* **77**, 765 (2004).
181. Shukla, A. *et al. Arch. Biochem. Biophys.* **428**, 144 (2004).
182. Chan, F. T. *et al. Analyst* **138**, 2156 (2013).
183. Pinotsi, D., Buell, A. K., Dobson, C. M., Kaminski Schierle, G. S. & Kaminski, C. F. *ChemBioChem* **14**, 846 (2013).
184. Chen, X. *et al. Sci. China Chem.* **61**, 351 (2018).
185. Jawor-Baczynska, A., Moore, B. D., Lee, H. S., McCormick, A. V. & Sefcik, J. *Faraday Discuss.* **167**, 425 (2013).
186. Zimbitas, G. *et al. Colloids Surf. A* **579**, 123633 (2019).
187. Mönig, J., Chapman, R. & Asmus, K. D. *J. Phys. Chem.* **89**, 3139 (1985).
188. Garrison, W. M. *Radiat. Res. Suppl.* **4**, 158 (1964).
189. Garrison, W. M. *Radiation-induced reactions of amino acids and peptides* (1971). [escholarship.org/uc/item/5rk086qm](https://escholarship.org/uc/item/5rk086qm), Accessed: April 2023.
190. Lundeen, R. A., Janssen, E. M.-L., Chu, C. & McNeill, K. *Chimia* **68**, 812 (2014).
191. Sun, Z. *et al. Environ. Sci. Tech.* **52**, 2953 (2018).
192. Mopper, K. & Zika, R. G. *Natural photosensitizers in sea water: riboflavin and its breakdown products in Photochemistry of Environmental Aquatic Systems* (ACS Publications, 1987).
193. Kreis, T. M., Adams, M. & Jüptner, W. P. in *Opt. Insp. Micromeas. II* **3098**, 224 (1997).
194. Garcia-Sucerquia, J. *et al. Appl. Opt.* **45**, 836 (2006).
195. Latychevskaia, T. & Fink, H.-W. *Appl. Opt.* **54**, 2424 (2015).



# Curriculum vitae

## Personal data

NAME	Oliver Rafael Reich
DATE OF BIRTH	21.05.1992
NATIONALITY	Swiss and Italian

## Education

02/2018 - CURRENT	<b>PhD studies</b> , Laboratory of physical chemistry ETH Zurich, Switzerland
09/2015 - 08/2017	<b>MSc ETH Physics</b> , ETH Zurich, Switzerland
09/2012 - 01/2016	<b>BSc ETH Physics</b> , ETH Zurich, Switzerland
08/2007 - 07/2011	<b>Highschool diploma (Matura)</b> Kantonsschule Frauenfeld, Switzerland

## Extracurricular experience

10/2011 - 05/2012	Civilian service, assistance physiotherapy Zent. Amb. Rehab. Zürich, Zürich, Switzerland
09/2016 - 12/2017	Civilian service, assistance patient care Kantonsspital Baden, Baden, Switzerland
09/2009 - 07/2019	Member of Zürcher Jugend Gitarren Ensemble

## Publication list

1. S. Ishizuka, **O. Reich**, G. David and R. Signorell "Photo-induced shrinking of aqueous glycine aerosol droplets" *Atmos. Chem. Phys. Discuss.* [preprint], <https://doi.org/10.5194/acp-2023-6>, in review (2023)
2. **O. Reich**, M.J. Gleichweit, G. David, N. Leemann and R. Signorell "Hygroscopic growth of single atmospheric sea salt aerosol particles from mass measurement in an optical trap" *Environ. Sci.: Atmos.* (2023)
3. **O. Reich**, G. David and R. Signorell "Anharmonic aerosol particle dynamics at Mie resonances in modulated counter-propagating optical tweezers" *Proc. SPIE 11798, Optical Trapping and Optical Micromanipulation XVIII*, 1179827 (2021)
4. **O. Reich**, G. David, K. Esat and R. Signorell "Weighing picogram aerosol droplets with an optical balance" *Comm. Phys.*, 3, 223 (2020)
5. G. David, **O. Reich**, M.E. Divéky, S. Roy, E.A. Parmentier, J.W. Cremer, K. Esat and R. Signorell "Characterization and control of droplets optically trapped in air" *Proc. SPIE 11083, Optical Trapping and Optical Micromanipulation XVI*, 1108322 (2019)

## Conference list

- |         |  |
|---------|--|
| 12/2022 | POSTER PRESENTATION - American Geophysical Union<br>Fall meeting 2022, Chicago, USA    |
| 08/2021 | ORAL PRESENTATION - SPIE Nanoscience + Engineering 2021<br>San Diego, USA              |
| 07/2021 | ORAL PRESENTATION - Summer school <i>Droplet 2020</i><br>Zurich, Switzerland           |
| 08/2019 | POSTER PRESENTATION - Swiss Chemical Society Fall meeting<br>2019, Zurich, Switzerland |



## Acknowledgements

I am very grateful to my supervisor, Ruth Signorell, who gave me the opportunity to work in the research topics that I have presented in this thesis. I enjoyed much freedom to exercise my own judgement in the projects I worked on, but could always rely on her for helpful advice and guidance in matters less familiar to me. I also thank Lukas Novotny for accepting the co-examination of my thesis and his insightful comments that improved this manuscript.

Many more people have contributed to the completion of this thesis, be it with their professional expertise or otherwise. My thanks go to the Aerosols and Nanoscience group at ETH Zurich, which has been a wonderful environment for me for the last five years. I want to thank in particular Grégory David for his many inputs over the course of my doctoral studies as well as Kıvanç Esat, with whom I have had the pleasure to work at the start of my doctorate. Both have made significant contributions to the building of the optical trapping setup which I was then given the opportunity to develop the mass measurement method on. I want to thank my other coworkers who were part of the projects presented in this thesis, Michael Gleichweit for his contribution to the measurement of the hygroscopicity of sea salt aerosols and Shinnosuke Ishisuka (Shin) for his collaboration in the investigation of the photolysis of aqueous glycine droplets. Shin brought to my attention the shrinking of the optically trapped glycine droplets, which started the investigation of this unexpected phenomenon. Many thanks to Johannes Cremer who introduced me to the concept of the modulation of the optical trapping beams and assisted me in the building of the modulated counter-propagating optical tweezers, which was instrumental for the work in this thesis. I also had the opportunity to supervise the semester projects of two highly motivated students, Joël Affolter and Nicole Leemann, which I thank a lot for their commitment. I am grateful for the technical assistance in all mechanical, electronic and chemical matters that I have received over the

## ACKNOWLEDGEMENTS

---

years, in particular from David Stapfer, Markus Steger and Daniel Zindel. Special thanks to David and Markus for building custom parts of the optical trapping setup.

I want to thank all my friends and family for supporting me during my doctoral studies. I want to thank in particular my former coworker Evelyne Parmentier, who may not have directly contributed to the work presented in this thesis, but has always been a good friend to me. My final thanks go to my parents, Luisa Fabro and Johannes Reich, as well as my sister Anouk for all their support.